Quasistatic component generation of ultrasonic waves and its applications in materials evaluation

Chang Jiang

A thesis submitted in fulfilment of the requirements for the degree of

Doctor of Philosophy

School of Architecture and Civil Engineering

Faculty of Sciences, Engineering and Technology

The University of Adelaide, Australia

January 2024

Abstract

The quasistatic component (QSC) of ultrasonic wave propagation is one of the nonlinear ultrasonic phenomena that results from the interaction between ultrasound and nonlinearities in the solid materials. Owing to the low frequency and high sensitivity to microstructural changes in materials, the QSC has promising potential for developing cost-effective materials testing approaches and damage detection methods. However, most generation features of QSC have not been revealed and understood due to the complex propagation characteristics of ultrasonic guided waves. This thesis systematically investigates the QSC generation of ultrasound propagation in different solid materials and geometries. By theoretical analysis, finite element modeling, and experimental studies, the wave type, displacement direction, generation efficiency, cumulative effect, temporal shape, and mode conversion of QSC are comprehensively investigated. For thin plates, Lamb waves and shear horizontal waves are selected as primary waves for the study of QSC generation. For pipe-like structures, longitudinal modes and torsional modes are employed in the investigation. The results show that the generated QSC pulse wave in different structures by different primary waves invariantly possesses the fastest velocity and has mainly in-plane particle displacement. Other properties of QSC are also explored and confirmed to be consistent with the theory and numerical results. Based on the guidance of the present theoretical, numerical, and experimental studies, potential materials characterization and nondestructive testing/evaluation techniques and methods have been proposed. The elastic properties and damage state of many industrial materials, including advanced composite materials, have been promisingly characterized by the measurement and quantification of the nonlinear QSC response. The findings of QSC generation can pave the way for more future cost-effective nondestructive testing/evaluation and structural health monitoring technologies of ultrasound.

Keywords: Ultrasound, Nonlinear Guided Waves, Quasistatic Component

Preface

This thesis is submitted as a "Thesis by Publications" in accordance with "Specifications for Thesis 2024" of The University of Adelaide. The journal articles generated are listed as follows:

List of publications

1. **Chang Jiang**, Weibin Li, Mingxi Deng, et al. (2021) Static component generation and measurement of nonlinear guided waves with group velocity mismatch, *JASA Express Letters* 1:055601.

2. **Chang Jiang**, Weibin Li, Mingxi Deng, et al. (2022) Quasistatic pulse generation of ultrasonic guided wave propagation in composites, *Journal of Sound and Vibration* 524:116764.

3. **Chang Jiang**, Changyu Zhang, Weibin Li, et al. (2022) Assessment of damage in composites using static component generation of ultrasonic guided wave, *Smart Materials and Structures* 31(4):045025.

4. **Chang Jiang**, Weibin Li, Ching-Tai Ng, et al. (2024) Quasistatic component generation of group velocity mismatched guided waves in tubular structures for microdamage localization, *Applied Acoustics 217:109813*.

5. **Chang Jiang**, Weibin Li, Ching-Tai Ng, et al. (2024) Numerical and experimental investigations on quasistatic pulse generation of ultrasonic guided waves in fiber reinforced composite pipes, *Journal of Sound and Vibration*.

HDR Thesis Declaration

I certify that this work contains no material which has been accepted for the award of any other degree or diploma in my name, in any university or other tertiary institution and, to the best of my knowledge and belief, contains no material previously published or written by another person, except where due reference has been made in the text. In addition, I certify that no part of this work will, in the future, be used in a submission in my name, for any other degree or diploma in any university or other tertiary institution without the prior approval of The University of Adelaide and where applicable, any partner institution responsible for the joint-award of this degree.

I acknowledge that copyright of published works contained within this thesis resides with the copyright holder(s) of those works.

I also give permission for the digital version of my thesis to be made available on the web, via the university's digital research repository, the Library Search and also through web search engines, unless permission has been granted by the university to restrict access for a period of time.

Signature: Date: 12.30.2023

Name: Chang Jiang

Acknowledgements

Unconsciously, I have been pursuing my student career for more than 20 years. I am honored to submit my doctoral thesis for review at this moment, which will be one of the proudest moments of my life. Three years of overseas doctoral study have allowed me to gain professional knowledge and make many friends, which is a memorable experience.

Firstly, I would like to thank my supervisors Prof. Alex Ching-Tai Ng and Prof. Weibin Li, who gave me valuable suggestions and comments on my study and research. In addition, I would like to express my gratitude to Prof. Mingxi Deng for his help on research creativity. I also thank the engineers/technicians Brenton Howie and Jon Ayoub of the school, who provided me with invaluable help for my experiments.

In addition, I would like to thank my colleagues, including John Wu, Henry Cao, Tina Yin, Harris Zhu, Alvin Hu, Eddie Wang, Jakson Zeng, Juan Pineda Allen, and Wayne Liang. In the meantime, I also thank my colleagues known from Xiamen University including Zifeng Lan, Tianze Shi, Jun Xiao, Changyu Zhang, and Hesheng Qu. They have helped me in my study and life in big or small ways.

Finally, I would like to say thank you to my parents and relatives. They have always supported my decisions and kept their trust and love for me from afar in China. I also want to say thank you to my domestic friends, including Mei Li, Carey Gao, Hengliang Huang, and so forth. We chat a lot in our spare time, and I am glad to have such great friends. They accompanied me for many years of graduate school life, helped me overcome various difficulties in my low times, and spent many wonderful moments with me, enabling me to reach today.

Above all, I hope that the people who love me and the people I love are healthy, happy, and prosperous.

Chang (Frankie) Jiang
Adelaide, South Australia
December 2023

Table of Contents

Chapter 1: Introduction

1.1. Nonlinear Ultrasound

Nonlinear ultrasound is a technique that involves the propagation of ultrasonic waves with a finite amplitude through a medium, resulting in nonlinear interactions between the propagating waves and the material or defects [1]. Two basic nonlinear effects are the acoustic-elastic effect and the harmonic generation [2]. The former is based on the dependence of ultrasonic wave velocity on external stress applied to the material. The latter typically involves higher harmonic generation, sub-harmonic generation, and nonlinear frequency-mixing [1]. In the field of medical imaging, nonlinear ultrasound waves play an increasingly important role in diagnostic and therapeutic medicine [3, 4]. For instance, microbubble contrast agents, once injected into the bloodstream, induce a nonlinear response upon interaction with ultrasound waves. This nonlinearity generates vibration frequencies different from the resonating frequency, which can be measured and processed to form images of the source of nonlinearity. The principal difference between linear and non-linear ultrasonic nondestructive evaluation is that in the latter, the propagating wave is assumed to have a finite amplitude and is accompanied by numerous effects, whose magnitudes depend on the vibration amplitude [2]. This makes the technique sensitive to distributed micro-defects or degradation, and overcomes some limitations of linear ultrasonic techniques [5]. Thus, nonlinear ultrasound is a powerful tool for nondestructive evaluation and medical imaging, providing unique insights into material properties and physiological processes.

The field of nonlinear ultrasound is a branch of nonlinear acoustics that started in 1755, and a short outline of the developments in nonlinear ultrasound from 1960 to 2000 was given by Bjørnø [6]. The major theoretical foundations forming the basis for numerical studies were available already in 1960 [7]. The early theoretical contributions to the nonlinear acoustics, including contributions from Lagrange (1760), Poisson (1808),

Stokes (1848), Earnshaw (1860), Riemann (1860), Rankine (1870), Huguenot (1889), Rayleigh (1910), Taylor (1910), Fay (1931), Fubini (1935), Burgers' (1948), Hopf (1950) and Cole (1951) can be found in [8]. The developments in nonlinear ultrasound during 1960 to 2000 was described as three main roads: 1) development of model equations and their solutions, 2) application in biological materials, focused ultrasound and parametric arrays, characterization of qualities of materials, 3) explanations to observations in industrial applications of high-power ultrasound, cavitation and bubble dynamics, sonochemistry, solitons and chaos, sonic booms, and nondestructive testing and evaluation [6].

Except for the topics of second-order acoustic nonlinearity of fluids, focused ultrasonic fields, parametric acoustic arrays, and thermoacoustics, the nonlinear ultrasonic waves in solids/interfaces and the related applications of nondestructive evaluation and structural health monitoring have been developing rapidly in the recent decades. A review on the nonlinear acoustic applications for material characterization was published by Solodov et al. in 1999 [9]. The review article gave general theoretical analysis of the effects of nonlinearity, dissipation, dispersion, and diffraction on intense acoustic wave propagation, along with the discussion on the nonlinear acoustic applications for solid material evaluation. The elasticity nonlinearity of solid materials can originate from asymmetry of lattice structure and dislocation in crystals, disbonds and cracks in engineering materials. The article also introduced the popular acoustic nonlinear parameters and their determination methods. Three main application fields, including biomedical imaging, acoustic microscopy, and nonlinear nondestructive evaluation, were presented.

1.2. Ultrasonic Guided Waves

Ultrasonic guided waves are a type of ultrasonic wave that can propagate along a structure, such as a pipe or a plate, for long distances. They have become critically

important in nondestructive testing and structural health monitoring, providing new, faster, more sensitive, and more economical ways of inspecting materials and structures [10]. The use of ultrasonic guided waves has increased tremendously over the past decade due to improved understanding and computational efficiency for complex problem-solving. These waves can be used to inspect large areas from a single location, making them particularly useful for inspecting structures where access is limited. In the field of nondestructive testing, ultrasonic guided waves can detect defects such as cracks or corrosion in a material. They can also be used to monitor the health of a structure over time, identifying any changes that may indicate a problem. Thus, ultrasonic guided waves are a powerful tool in the field of nondestructive testing and structural health monitoring, offering unique capabilities for inspecting and monitoring materials and structures.

Ultrasonic guided waves can be grouped into different types in terms of the structures of wave guides. For thin plate structures, the Lamb waves and shear horizontal guided waves are two major waves. For Lamb waves, the particle motion lies in the plane that contains the direction of wave propagation and the direction perpendicular to the plate. In 1917, the English mathematician, Horace Lamb, published his classic analysis and description of acoustic waves of this wave [10]. Their properties turned out to be quite complex. Since the 1990s, the understanding and utilization of Lamb waves has advanced greatly, thanks to the rapid increase in the availability of computing power. Lamb's theoretical formulations have found substantial practical application, especially in the field of nondestructive testing. For shear horizontal (SH) guided waves, the term "horizontal shear" means that the particle vibrations (displacements and velocities) caused by any of the SH modes are in a plane that is parallel to the surfaces of the layer.

For guided waves in pipe-like structures, there are three wave families: 1) torsional modes, 2) longitudinal modes, and 3) flexural modes [10]. Torsional modes involve the twisting of the structure around its longitudinal axis. In pipes, torsional modes are

particularly useful because they are non-dispersive (i.e., their velocity does not depend on frequency), which simplifies data interpretation. Longitudinal modes involve the compression and dilation of the structure along its length. Flexural modes involve the bending of the structure. Flexural modes can be very sensitive to defects on the structure's surface. Additionally, there is Rayleigh surface waves, which propagate mainly along the surfaces of solids. Rayleigh waves include both longitudinal and transverse motions that decrease exponentially in amplitude as distance from the surface increases [10]. There is a phase difference between these component motions. The existence of Rayleigh waves was discovered in 1885 by Lord Rayleigh, after whom they were named. Besides, circumferential guided waves are guided waves that propagate in the circumferential direction of a hollow cylinder, such as a pipe. There are two types of circumferential guided waves: circumferential shear horizontal waves (CSH-waves) and circumferential Lamb type waves (CLT-waves). They have many practical applications, including the detection of corrosion in piping from in-pipe or in-line inspection vehicles [10].

1.3. Nonlinear Ultrasonic Guided Waves

In the past two decades, nonlinear ultrasonic guided waves have become a crucial instrument for identifying early-stage damage in structures such as plates, pipes/tubes, rods, and rails. The benefits of these waves are a combination of the previously mentioned advantages of nonlinear ultrasonics (enhanced sensitivity and the ability to detect early damage) and guided waves (features like volumetric coverage, long-distance propagation, single-sided access, rapid inspection, and the ability to inspect unreachable areas) [11]. The use of non-contact techniques like laser excitation and laser Doppler vibrometer measurements could yield additional benefits. However, due to the complex and dispersive nature of guided waves, they pose several analytical challenges that are not encountered with bulk waves. Without a proper understanding of their propagation, the chances of successfully conducting an inspection using

nonlinear guided waves are extremely low [11].

The growing focus on the development of testing methods using nonlinear ultrasonic guided waves is primarily due to the theoretical progress in the propagation of nonlinear guided waves in solid media. A common acoustic nonlinear response is the production of second harmonics, which can be effectively utilized to assess damage or degradation in materials and structures [12]. Regarding second harmonic generation of guided waves, there are two main research branches: 1) nonlinear acoustic responses generated by the material nonlinearity, and 2) nonlinear acoustic phenomena induced by the local damages. The former is closely related to the material constitutive model, i.e., the stress-strain relationship. The latter is based on the effect of local acoustic nonlinearity, e.g., the breathing cracks/delamination. In the 1990-2000s, a few significant studies [13-15] on the second harmonic generation of guided Lamb waves in thin solid plates were published. The two important conditions that are required by the cumulative second harmonic generation were determined as: 1) non-zero power flux, and 2) synchronism/phase matching. The physics for second harmonic generation in intact thin plates is also applicable to that in hollow cylinder structures. It is important to note that the cumulative second harmonic wave generation is associated with the material nonlinearity of a regional area of the solid. On the other hand, contact acoustic nonlinearity (CAN) has been investigated by many researchers [16, 17]. It has been found that under favorable conditions – nonlinear effects exhibited by cracks are stronger than crack-induced linear phenomena. This is especially useful for local microdamage detection where the linear ultrasound is not sensitive to microdamage, and traditional nonlinear ultrasonic techniques are not viable due to the intrinsic limitations of higher harmonic generation. There are studies focused on the mechanisms of CAN and proposed physical models for simulating the CAN effect of ultrasound propagation [18, 19]. Apart from the CAN phenomenon, the hysteresis nonlinearity, quasi-static pulse generation, sub-harmonic generation, wave mixing, and resonant ultrasound spectroscopy are also important nonlinear acoustic phenomena that can

occur in guided wave propagations [11, 20, 21].

1.4. Ultrasonic Techniques for Materials Characterization

Nondestructive testing (NDT) techniques are crucial for materials characterization without causing any damage to the tested materials. These methods are widely used in various industries to ensure the integrity, quality, and reliability of materials [22]. There are many common NDT techniques for materials characterization, including ultrasonic testing (UT), radiographic testing (RT), magnetic particle testing (MPT), dye penetrant testing (PT), eddy current testing (ECT), acoustic emission testing (AET), infrared thermography (IRT), and so on. Especially, high-frequency sound waves can usually be used to detect internal flaws, measure thickness, and characterize material properties with relatively higher efficiency and accuracy [2].

For metallic materials, cracks, fatigue, thermal damage, corrosion damage, and plastic damages are common. To detect and evaluate these damages, many technologies and methods based on ultrasound have been developed. Felice et al. conducted a review of bulk wave methods for sizing flaws [23]. They categorized the methods into four types: i) amplitude techniques (measuring the amplitude of a signal from the flaw and using the amplitude value, and often other knowledge, to infer the flaw size.), ii) temporal techniques (the arrival time of one or more signals from the flaw are used to infer its size), iii) imaging techniques (signals from the flaw are used to obtain a two-dimensional or three-dimensional representation of the region of interest and flaw sizes are inferred from this representation in various ways), and iv) inversion techniques (signals from the flaw are inputted into algorithms which determine the physical properties of the flaw from which the signals originated). In general, linear ultrasonic methods are used for macro-damages detection and evaluation. Due to the relationship between the sizes of wavelength and the flaws, linear ultrasonic features including wave reflection/transmission and attenuation are insensitive to smaller flaws of

subwavelength sizes. For the microdamage characterization, Maier et al. [24] proposed the noncontact nonlinear resonance ultrasound spectroscopy (NRUS) method for evaluating microscopic damages in small metallic specimens using the nonclassical hysteretic nonlinearity parameter. Many other researchers [25-28] have also proposed novel techniques for detecting early-stage microdamage in metallic materials based on the measurement of nonlinear ultrasonic responses.

As the popularity of lighter, stiffer, stronger and tougher substances is growing, there are increasing publications focused on the NDT of fiber reinforced composite materials. For composite materials and structures, the nonlinear ultrasound techniques also play an important role. Due to the special damage mechanisms (e.g., delamination, debonding, matrix cracks) of composites, the use of the ultrasonic method in composite materials can be more complicated than that in metallic materials. Aslam et al. investigated the mixed harmonic generation in damaged concrete [29]. Yu et al. used the feature guided waves in quasi-isotropic composite bends for damage detection [30]. Liao et al. studied the damage monitoring of bolted joints using both the piezoelectric impedance and ultrasonic guided waves [31]. Liu et al. proposed a non-elliptical probability imaging method for delamination detection of anisotropic composite plates using nonlinear ultrasonic guided wave [32]. Li et al. described an experimental procedure for improving the detectability of small defects in thick carbon fiber composite materials based on the total focusing method (TFM) [33]. A comprehensive introduction of physical ultrasonics of composites can be found in [34].

1.5. Research Questions & Objectives

Research in the field of nonlinear ultrasound in solids explores various aspects of material characterization, damage detection, and understanding the nonlinear behavior of materials under ultrasonic excitation. While specific research questions may evolve over time, there are some general areas of interest and popular research questions in the

field of nonlinear ultrasound for solids [1, 11]:

1) Nonlinear Elasticity: i) How can nonlinear ultrasonic techniques be used to characterize the nonlinear elastic properties of materials? ii) What are the relationships between microstructural features and nonlinear elastic responses in different materials?

2) Damage Detection: i) How can nonlinear ultrasound be employed for early detection and characterization of damage, such as fatigue cracks, in solid materials? ii) What nonlinear features are more or the most sensitive to different types and stages of damage in materials?

3) Nonlinear Guided Waves: i) How can nonlinear guided waves be utilized for improving defect detection and characterization in waveguides such as pipes, rods, and plates? ii) What are the effects of material anisotropy on the propagation and interaction of nonlinear guided waves?

4) Material Microstructure: i) How does the microstructure of materials influence their nonlinear response to ultrasonic waves? ii) Can nonlinear ultrasound provides insights into the evolution of microstructural changes in materials?

5) Nonlinear Imaging Techniques: i) What novel imaging techniques can be developed using nonlinear ultrasound for improved spatial resolution in material characterization? ii) How can nonlinear imaging be applied to visualize and quantify heterogeneities within materials?

6) Nonlinear Acoustic Microscopy: i) How can nonlinear acoustic microscopy be advanced for high-resolution imaging of sub-surface features in solid materials? ii) What are the limitations and opportunities for nonlinear acoustic microscopy in various material types?

7) Thermal Effects: i) How do thermal effects, such as temperature-dependent material properties, influence the nonlinear behavior of materials under ultrasonic excitation? ii) Can nonlinear ultrasound be used for nondestructive evaluation of thermal-induced damage in materials?

8) Nonlinear Wave Propagation Modeling: i) What advanced numerical models can accurately simulate the nonlinear wave propagation in solids? ii) How can these models be validated and improved based on experimental data?

9) Material Characterization in Extreme Environments: i) How can nonlinear ultrasound be applied for material characterization in extreme conditions, such as high temperatures, radiation, or aggressive chemical environments? ii) What are the challenges and opportunities in extending nonlinear ultrasound techniques to harsh operational environments?

10) Integration with Other NDE Techniques: i) How can nonlinear ultrasound complement and be integrated with other nondestructive evaluation (NDE) techniques for comprehensive material assessment? ii) What are the synergies between nonlinear ultrasound and other emerging technologies in the field of materials characterization?

It is noted that research in nonlinear ultrasound for solids is dynamic and continually evolving, driven by advancements in both experimental techniques and theoretical understanding. Researchers aim to develop more robust and sensitive methods for nondestructive characterization of materials, with potential applications in diverse industries ranging from aerospace and manufacturing to civil engineering and healthcare. Here in the thesis, investigation is primarily focused on the quasistatic component (QSC) generation of ultrasonic waves. Currently, the QSC generation regarding elastic waves has not yet fully understood. As one of the nonlinear acoustic responses of ultrasound in solids, the QSC can have particular features and be beneficial for practical applications. The investigation aims to explore the QSC generation from both the theoretical, numerical, and experimental perspectives. Detailed objectives of the thesis are:

1. To systematically explore the generation characteristics, wave mode/type, and propagation features of QSC in solid structures with material nonlinearities.
2. To relate the QSC generation with material characterization and take advantages of

QSC generation for developing new NDT techniques.

3. To assess microdamage in metallic, polymer, and fiber reinforced composite materials using the QSC generation and validate its reliability and sensitivity.

The thesis is structured as follows: Chapter 2 provides a critical review on the previously published studies of QSC generation. Chapter 3 reports the numerical study of QSC generation by both Lamb waves and shear horizontal waves in isotropic metallic thin plates. Chapter 4 presents the numerical study of QSC generation in anisotropic composite thin plates. Chapter 5 provides both the numerical and experimental studies on the QSC generation in three-dimensional anisotropic composites plates with finite sizes. Chapter 6 is a study on the QSC generation of guided waves in isotropic metallic pipe-like structures. Chapter 7 presents a study on the QSC generation of guided waves in anisotropic composite pipe-like structures. Chapter 8 provides the summary of the findings and future research recommendations.

References:

[1]   Jhang K-Y, Measurement of nonlinear ultrasonic characteristics, Singapore: Springer Singapore, 2020.

[2]   Marcantonio V, Monarca D, Colantoni A, Cecchini M. Ultrasonic waves for materials evaluation in fatigue, thermal and corrosion damage: A review. Mechanical Systems and Signal Processing 2019;120:32-42. 10.1016/j.ymssp.2018.10.012.

[3]   Hall TJ, Barbone PE, Oberai AA, Jiang JF, Dord JF, Goenezen S, Fisher TG. Recent Results in Nonlinear Strain and Modulus Imaging. Current Medical Imaging 2011;7:313-327.

[4]   Tang MX, Kamiyama N, Eckersley RJ. Effects of nonlinear propagation in ultrasound contrast agent imaging. Ultrasound in Medicine and Biology 2010;36:459-466. 10.1016/j.ultrasmedbio.2009.11.011.

[5]   Yun HG, Rayhana R, Pant S, Genest M, Liu Z. Nonlinear ultrasonic testing

and data analytics for damage characterization: A review. Measurement 2021;186:23. 110155. 10.1016/j.measurement.2021.110155.

[6]   Bjørnø L. Forty years of nonlinear ultrasound. Ultrasonics 2002;40:11-17.

[7]   Mason WP, Physical acoustics, New Jersey: Academic Press, 1964.

[8]   Bjørnø L. Proceedings of the open seminar on acoustics. Solina-Jawor 2000;1:19-30.

[9]   Zheng YM, RG, Solodov, IY. Nonlinear acoustic applications for material characterization: A review. Canadian Journal of Physics 1999;77:927-967.

[10]   Rose J, Ultrasonic guided waves in solid media, Cambridge: Cambridge University Press, 2014.

[11]   Chillara VK, Lissenden CJ. Review of nonlinear ultrasonic guided wave nondestructive evaluation: theory, numerics, and experiments. Optical Engineering 2015;55:011002. 10.1117/1.Oe.55.1.011002.

[12]   Li WB, Deng MX, Xiang YX. Review on second-harmonic generation of ultrasonic guided waves in solid media (I): Theoretical analyses. Chinese Physics B 2017;26:15. 114302. 10.1088/1674-1056/26/11/114302.

[13]   Deng MX. Cumulative second-harmonic generation accompanying nonlinear shear horizontal mode propagation in a solid plate. Journal of Applied Physics 1998;84:3500-3505. 10.1063/1.368525.

[14]   Deng MX. Second-harmonic generation of ultrasonic guided wave propagation in an anisotropic solid plate. Applied Physics Letters 2008;92:111910. 10.1063/1.2899938.

[15]   Li WB, Deng MX, Xiang YX. Review on second-harmonic generation of ultrasonic guided waves in solid media (I): Theoretical analyses. Chinese Physics B 2017;26:114302. 10.1088/1674-1056/26/11/114302.

[16]   Solodov IY, Krohn N, Busse G. CAN: an example of nonclassical acoustic nonlinearity in solids. Ultrasonics 2002;40:621-625. 10.1016/S0041-624X(02)00186-5.

[17]   Broda D, Staszewski WJ, Martowicz A, T.Uhl, Silberschmidt VV. Modelling

of nonlinear crack–wave interactions for damage detection based on ultrasound—A review. Journal of Sound and Vibration 2014;333:1097–1118. 10.1016/j.jsv.2013.09.033.

[18]   Aleshin V, Delrue S, Trifonov A, Matar OB, Abeele KVD. Two dimensional modeling of elastic wave propagation in solids containing cracks with rough surfaces and friction – Part I: Theoretical background. Ultrasonics 2018;82:11-18. 10.1016/j.ultras.2017.07.002.

[19]   Delrue S, Aleshin V, Truyaert K, Matar OB, Abeele KVD. Two dimensional modeling of elastic wave propagation in solids containing cracks with rough surfaces and friction – Part II: Numerical implementation. 2018;82:19-30. 10.1016/j.ultras.2017.07.003.

[20]   Jhang K-Y. Nonlinear Ultrasonic Techniques for Nondestructive Assessment of Micro Damage in Material: A Review. International Journal of Precision Engineering and Manufacturing 2009;10:123-135. 10.1007/s12541-009-0019-y.

[21]   Yun H, Rayhana R, Pant S, Genest M, Liu Z. Nonlinear ultrasonic testing and data analytics for damage characterization: A review. Measurement 2021;186:110155. 10.1016/j.measurement.2021.110155.

[22]   Li D, Zhou J, Ou J. Damage, nondestructive evaluation and rehabilitation of FRP composite-RC structure: A review. Construction and Building Materials 2021;271:121551. 10.1016/j.conbuildmat.2020.121551.

[23]   Felice MV, Fan Z. Sizing of flaws using ultrasonic bulk wave testing: A review. Ultrasonics 2018;88:26-42. 10.1016/j.ultras.2018.03.003.

[24]   Maier S, Kim J-Y, Forstenhäusler M, Wall JJ, Jacobs LJ. Noncontact nonlinear resonance ultrasound spectroscopy (NRUS) for small metallic specimens. NDT & E International 2018;98:37-44. 10.1016/j.ndteint.2018.04.003.

[25]   Ruiz A, Ortiz N, Medina A, Kim JY, Jacobs LJ. Application of ultrasonic methods for early detection of thermal damage in 2205 duplex stainless steel. NDT & E International 2013;54:19-26. 19. 10.1016/j.ndteint.2012.11.009.

[26]   Xiang YX, Deng MX, Xuan FZ. Creep damage characterization using nonlinear ultrasonic guided wave method: A mesoscale model. Journal of Applied Physics 2014;115:10.1063/1.4863639.

[27]   Kim J-Y, Jacobs LJ, Qu J, Littles JW. Experimental characterization of fatigue damage in a nickel-base superalloy using nonlinear ultrasonic waves. The Journal of the Acoustical Society of America 2006;120:1266-1273. 10.1121/1.2221557.

[28]   Li WB, Cho Y. Thermal Fatigue Damage Assessment in an Isotropic Pipe Using Nonlinear Ultrasonic Guided Waves. Experimental Mechanics 2014;10.1007/s11340-014-9882-2.

[29]   Aslam M, Nagarajan P, Remanan M. Nonlinear ultrasonic evaluation of damaged concrete based on mixed harmonic generation. Structural Control and Health Monitoring 2022;29:10.1002/stc.3110.

[30]   Yu X, Ratassepp M, Fan Z. Damage detection in quasi-isotropic composite bends using ultrasonic feature guided waves. Composites Science and Technology 2017;141:120-129. 120. 10.1016/j.compscitech.2017.01.011.

[31]   Liao W, Sun H, Wang Y, Qing X. A novel damage index integrating piezoelectric impedance and ultrasonic guided wave for damage monitoring of bolted joints. Structural Health Monitoring 2023;147592172311594. 10.1177/14759217231159427.

[32]   Liu Y, Hong X, Zhang B. Contact delamination detection of anisotropic composite plates using non-elliptical probability imaging of nonlinear ultrasonic guided waves. Structural Health Monitoring 2022;22:276-295. 276. 10.1177/14759217221085159.

[33]   Li C, Pain D, Wilcox PD, Drinkwater BW. Imaging composite material using ultrasonic arrays. NDT&E International 2013;53:8-17. 10.1016/j.ndteint.2012.07.006.

[34]   Rokhlin S, Chimenti D, Nagy P, Physical ultrasonics of composites: Oxford University Press, 2011.

Chapter 2: Literature Review

2.1. Generation Mechanism & Significance of QSC

The QSC of ultrasonic waves in solid materials can be generated due to the nonlinearity of the material constitutive equations, i.e., the nonlinear stress-strain relation. Thus, the QSC can be regarded as one of those nonlinear ultrasonic responses induced by such material nonlinearity. In contrast to linear characteristics of ultrasound in solid materials, these nonlinear ultrasonic responses generated by the interaction of ultrasound with the solid materials can be of rather small magnitude. Linear features such as wave velocity and wave attenuation (damping) can be generally related to the linear wave motion equation, while those nonlinear features are mostly associated with the nonlinear parts of the wave equation.

From the point of physical theory, the solution of a longitudinal wave equation considering the higher order elasticity of the material can generally have the static component (DC wave signal), the fundamental wave, the second harmonic wave, the third order harmonic wave, and so forth. Depending on the symmetrical characteristic of the stress-strain curve, the even order harmonic waves (e.g., second harmonic, fourth order harmonic) can be cancelled out sometimes. Besides, the higher the order of the elasticity we include in the wave equation, the more accurate the solution of wave field can be. However, from the perspective of practical measurement, only the static component, the second harmonic wave, and the third order harmonic wave are significant enough that modern instruments are capable of measuring the effective nonlinear signals of relatively larger magnitudes. It should be noted that, in experiments, we typically excite tone-burst ultrasonic waves into the specimens. Therefore, the wave field solution for plane longitudinal wave equation will be different from the actual wave field in experiments. In that case, the term QSC is used for representing the static strain/component caused by the tone-burst acoustic radiation, which is at near-zero

frequency in frequency domain after Fourier transform.

It should be noted that some recent studies have reported that the QSC of ultrasound propagation in solids with local microcracks can occur as well. Due to the breathing effect of such microcracks, the local stress-strain of the materials is nonlinear, leading to the generation of QSC and higher harmonics.

However, by comparing the three nonlinear components induced by the propagation of one mono-frequency ultrasound in weekly nonlinear solid (i.e., QSC, the second harmonic wave, and the third harmonic wave), we can further understand their advantages and drawbacks respectively, regarding the potential value for industrial applications. As is widely known, the higher the frequency of ultrasound, the greater the energy of the ultrasonic beam will possess, if the time duration is the same. However, with shorter wavelength for high frequency wave, the wave attenuation in damping materials is also greater than that of the low-frequency one. Thus, the QSC has greater value for nonlinear ultrasonic applications in damping materials such as composites and porous materials. The signal-to-noise ratio of QSC will be higher compared to the correspondingly generated second and third harmonics.

However, this may not be true if we consider the abilities of available instruments at the moment. For PZTs/transducers, they are cost-effective for measuring the vibrational signals of certain frequency ranges. This leads to the fact that we may not be able to measure the QSC with the expected high signal-to-noise ratio, as it is of rather low frequency. Laser vibrometer can be promisingly used for measuring the QSC, but the cost will be much higher than using PZTs. Above all, the QSC is still worth deep and systematic investigation based on its already known unique acoustic features. As we understand it more, we can push the scientific boundary of nonlinear acoustics even further and create more powerful and comprehensive methods and tools applicable in many engineering fields.

2.2. Research History of QSC

The existence of QSC was first theoretically predicted by Cantrell in [1]. Besides, there is a follow-up paper [2] discussing the features of QSC, especially the shape of QSC. Based on the predictions by Yost et al., the quasistatic displacement pulse produced by a longitudinal plane wave propagation through a semi-infinite elastic solid with quadratic nonlinearity must be of right-triangular shape. Yost et al. also conducted measurements to validate their analytical predictions in the crystallographic direction of single crystal silicon and isotropic vitreous silica [2]. Besides, the slope of the quasistatic displacement pulse was measured by Cantrell et al. and was used for calculation of the nonlinearity parameter of crystalline silicon in all three crystallographic symmetry directions [3]. Although the calculation of nonlinearity parameter by the measurement of QSC slope is in line with the known value, their experiments did not directly validate the shape of the QSC as right triangular with a sharp leading edge and a uniformly decreasing slope until the end of the pulse.

Later, more analytical, numerical, and experimental evidence emerged that presents different results compared to those of Cantrell. Jacob et al. implemented direct measurement on the QSC displacement using an optical interferometer in fused silica and aluminum alloy samples, and found that the QSC produced by a longitudinal acoustic wave has a flat-top shape [4]. Also, they found the amplitude of QSC is independent of the pulse duration, but dependent on the QSC propagation distance. Later in 2007, Rénier et al. also reported that the radiated QSC amplitude by ultrasonic tone burst in water is proportional to the wave propagation distance [5]. Narasimha et al. studied the QSC pulse in Al7175-T7351 alloy using a piezoelectric receiver, and confirmed the flat-top shape of QSC and the irrelevance of the QSC amplitude with the duration of the tone burst [6]. Later, there were rebuttals [7-9] around the features of QSC generation by ultrasonic longitudinal waves generated by piezoelectric transducers. In 2011 and 2012, Qu et al. also published their research on the topic of QSC generation [10, 11]. They obtained an analytical solution for the propagation of

tone burst in elastic solids with quadratic nonlinearity. They found that the cumulative pulse amplitude is proportional to the wave propagation length and is independent of the tone burst duration. They also analyzed the effects of boundary conditions on the QSC generation and noted the difficulty of evaluating the acoustic nonlinearity parameter using QSC generation. However, Cantrell et al. had another argument [12] in terms of the violation of law of energy conservation as the response to the above new findings.

In 2013, the controversial issue of quasistatic pulse generation by longitudinal ultrasonic waves in weakly nonlinear solids was basically settled following the study by Nagy et al. that presents rigorous analytical analysis and robust numerical simulations [13]. It is again confirmed that the time-domain shape of the quasistatic pulse generated by a longitudinal plane wave is not a right-angle triangle. Besides, the amplitude of QSC pulse is proportional to the wave propagation distance. The shape of QSC pulse is closely related to the boundary conditions that how the primary tone burst wave is excited and received. Besides, the finite size effect was also investigated, and it was found that the QSC pulse suffers large divergence loss than the correspondingly generated second harmonic waves.

However, the above studies are all associated with the longitudinal waves, either theoretical longitudinal plane wave, or experimental longitudinal tone burst wave. In 2018, Wan et al. first published their numerical studies on the QSC generation from guided wave propagation in thin isotropic aluminum plate [14]. They extracted the QSC time signals using the empirical mode decomposition method and confirmed that the QSC generation by Lamb waves in thin metallic plate with quadratic elastic nonlinearity is intrinsically cumulative regardless of the well-known synchronism and none-zero power flux conditions that are required by cumulative second harmonic generation of Lamb waves. In the same year, Sun et al. also investigated the QSC generation of Lamb waves in isotropic metallic plates, by both theoretical study, simulation and experiments. However, the results are less convincing regarding the

investigation details [15]. In 2020, Deng proposed an experimental method for measuring the QSC in solids using piezoelectric transducers [16]. Soon later, Sun et al. investigated the local plastic damage evaluation using the QSC of Lamb waves [17]. They used PZTs for excitation and receiving of the waves and showed the effectiveness of the method in plastic damage evaluation in Al-6061 specimens. Besides, Sun et al. conducted a numerical study for QSC generation by bulk waves in solid with randomly distributed micro-cracks [18]. It was found that the QSC can also be generated by simulated CAN effect.

However, none of the above-mentioned studies has shown a systematic study on the QSC generation by guided waves in common solid waveguides. The thesis aims to cover the study of QSC generation of different guided wave propagations in different solid structures and materials. For guided waves in thin plate-like structures, Lamb waves and shear horizontal waves are selected as primary waves for the investigation of QSC pulse generation. For guided waves in pipe-like structures, the longitudinal guided waves and torsional guide waves are selected as primary waves for the investigation of QSC pulse generation. Additionally, both the isotropic metallic materials and the anisotropic fiber reinforced composite materials are selected as the waveguides for studying the QSC generation. By analytical, numerical, and experimental studies, the QSC pulse, as one of the nonlinear ultrasonic responses in solids with weak material nonlinearity, is systematically investigated. The wave mode (wave structure), cumulative effective of generation, generation efficiency, and temporal shape of the nonlinear QSC signal are analyzed and discussed. Consequently, feasibility studies of the potential NDT applications based on the measurement of QSC generation are also conducted and discussed.

References:

[1]   Cantrell JH. Acoustic-radiation stress in solids. I. Theory. Physical Review B 1984;30:3214-3220. 10.1103/PhysRevB.30.3214.

[2]   Yost WT, Cantrell JH. Acoustic-radiation stress in solids. II. Experiment. Physical Review B 1984;30:3221-3227. 10.1103/PhysRevB.30.3221.

[3]   Cantrell JH, Yost WT, Li P. Acoustic radiation-induced static strains in solids. Physical Review B 1987;35:9780-9782. 10.1103/PhysRevB.35.9780.

[4]   Jacob X, Takatsu R, Barrière C, Royer D. Experimental study of the acoustic radiation strain in solids. Applied Physics Letters 2006;88:10.1063/1.2191428.

[5]   Rénier M, Barrière C, Royer D. Optical measurements of the self-demodulated displacement and its interpretation in terms of radiation pressure. The Journal of the Acoustical Society of America 2007;121:3341-3348. 10.1121/1.2730624.

[6]   Thimmavajjula Narasimha K, Kannan E, Balasubramaniam K. Simplified experimental technique to extract the acoustic radiation induced static strain in solids. Applied Physics Letters 2007;91:10.1063/1.2793181.

[7]   Cantrell JH. Effects of diffraction and dispersion on acoustic radiation-induced static pulses. Applied Physics Letters 2008;92:10.1063/1.2937474.

[8]   Narasimha KT, Kannan E, Balasubramaniam K. Issues on the pulse-width dependence and the shape of acoustic radiation induced static displacement pulses in solids. Journal of Applied Physics 2009;105:10.1063/1.3093873.

[9]   Cantrell JH, Yost WT. Shape profile of acoustic radiation-induced static displacement pulses in solids. Journal of Applied Physics 2010;108:10.1063/1.3457850.

[10]   Qu J, Jacobs LJ, Nagy PB. On the acoustic-radiation-induced strain and stress in elastic solids with quadratic nonlinearity (L). The Journal of the Acoustical Society of America 2011;129:3449-3452. 10.1121/1.3583501.

[11]   Qu J, Nagy PB, Jacobs LJ. Pulse propagation in an elastic medium with quadratic nonlinearity (L). The Journal of the Acoustical Society of America 2012;131:1827-1830. 10.1121/1.3681922.

[12]   Cantrell JH, Yost WT. Energy conservation and pulse propagation in an elastic medium with quadratic nonlinearity. Journal of Applied Physics 2012;112:10.1063/1.4748963.

[13] Nagy PB, Qu J, Jacobs LJ. Finite-size effects on the quasistatic displacement pulse in a solid specimen with quadratic nonlinearity. J Acoust Soc Am 2013;134:1760-74. 10.1121/1.4817840.

[14] Wan X, Tse PW, Zhang X, Xu G, Zhang Q, Fan H, Mao Q, Dong M, Wang C, Ma H. Numerical study on static component generation from the primary Lamb waves propagating in a plate with nonlinearity. Smart Materials and Structures 2018;27:045006. 10.1088/1361-665X/aaafeb.

[15] Sun X, Ding X, Li F, Zhou S, Liu Y, Hu N, Su Z, Zhao Y, Zhang J, Deng M. Interaction of Lamb Wave Modes with Weak Material Nonlinearity: Generation of Symmetric Zero-Frequency Mode. Sensors (Basel) 2018;18:10.3390/s18082451.

[16] Deng MX. An Experimental Approach for Detection of the Acoustic Radiation Induced Static Component in Solids. Chinese Physics Letters 2020;37:074301. 10.1088/0256-307x/37/7/074301.

[17] Sun X, Shui G, Zhao Y, Liu W, Hu N, Deng M. Evaluation of early stage local plastic damage induced by bending using quasi-static component of Lamb waves. NDT & E International 2020;116:102332. 10.1016/j.ndteint.2020.102332.

[18] Sun X, Liu H, Zhao Y, Qu J, Deng MX, Hu N. The zero-frequency component of bulk waves in solids with randomly distributed micro-cracks. Ultrasonics 2020;107:106172. 10.1016/j.ultras.2020.106172.

Chapter 3: Static Component Generation and Measurement of Nonlinear Guided Waves with Group Velocity Mismatch

3.1. Introduction, Significance, and Commentary

Although the QSC generation in solids by longitudinal plane wave has been theoretically investigated before, rare reports can be found on the QSC generation of guided waves in solids. This study explores the QSC generation by both Lamb waves and shear horizontal guided waves in isotropic metallic materials. By use of finite element simulation method, the generation characteristics of QSC by guided wavs have been revealed. The cumulative effect of QSC generation in isotropic thin plates has been confirmed. The study provides intuitive prospectives for the further study of QSC generation and development of practical applications.

3.2. Publication

This section is presented as published research paper by **Chang Jiang**, Weibin Li, Mingxi Deng, and Ching-Ti Ng (2021) Static component generation and measurement of nonlinear guided waves with group velocity mismatch, *JASA Express Letters* 1:055601.

Statement of Authorship

Title of Paper	Static component generation and measurement of nonlinear guided waves with group velocity mismatch
Publication Status	☑ Published ☐ Accepted for Publication ☐ Submitted for Publication ☐ Unpublished and Unsubmitted work written in manuscript style
Publication Details	Chang Jiang, Weibin Li, Mingxi Deng, et al. (2021) Static component generation and measurement of nonlinear guided waves with group velocity mismatch, JASA Express Letters 1:055601.

Principal Author

Name of Principal Author (Candidate)	Chang Jiang		
Contribution to the Paper	Methodology, Investigation, Data curation, Visualization, Writing - Original Draft		
Overall percentage (%)	80		
Certification:	This paper reports on original research I conducted during the period of my Higher Degree by Research candidature and is not subject to any obligations or contractual agreements with a third party that would constrain its inclusion in this thesis. I am the primary author of this paper.		
Signature		Date	2023.12.29

Co-Author Contributions

By signing the Statement of Authorship, each author certifies that:

i. the candidate's stated contribution to the publication is accurate (as detailed above);

ii. permission is granted for the candidate in include the publication in the thesis; and

iii. the sum of all co-author contributions is equal to 100% less the candidate's stated contribution.

Name of Co-Author	Weibin Li		
Contribution to the Paper	Conceptualization, Resources, Writing - Review & Editing, Supervision, Funding acquisition		
Signature		Date	2023.12.29

Name of Co-Author	Mingxi Deng		
Contribution to the Paper	Resources, Writing - Review & Editing, Supervision		
Signature		Date	2023.12.29

Name of Co-Author	Ching-Tai Ng		
Contribution to the Paper	Writing - Review & Editing, Supervision		
Signature		Date	2023.12.29

Please cut and paste additional co-author panels here as required.

Static component generation and measurement of nonlinear guided waves with group velocity mismatch

Chang Jiang,[1] Weibin Li,[1,a)] Mingxi Deng,[2] and Ching-Tai Ng[3]

[1]*School of Aerospace Engineering, Xiamen University, Fujian, China*
[2]*College of Aerospace Engineering, Chongqing University, Chongqing, China*
[3]*School of Civil, Environmental, and Mining Engineering, University of Adelaide, Adelaide, South Australia, Australia*

jiangc632@gmail.com, liweibin@xmu.edu.cn, dengmx65@yahoo.com, alex.ng@adelaide.edu.au

Abstract: This study focuses on static component generation (SCG) and its measurement wherein a group velocity mismatch (GVM) exists between the primary guided wave and the generated static component (SC). The SCGs by primary S0, A0, and SH0 waves are investigated. It is confirmed that the SCs are S0 mode. The GVM causes the temporal waveforms of the SCs to tend to increase in width with propagation distance. A feasible method is proposed accordingly for measurement of SCG with GVM using only lead zirconic titanate based transducers, wherein the SCs generated by two counter-propagating primary waves are modulated and superposed on each other. © 2021 Author(s). All article content, except where otherwise noted, is licensed under a Creative Commons Attribution (CC BY) license (http://creativecommons.org/licenses/by/4.0/).

1. Introduction

Nonlinear ultrasonic responses generated from wave interaction with material nonlinearity have been widely investigated for micro-damage detection and materials characterization in recent years (Kundu, 2018). Among different types of nonlinear responses, the generation of an acoustic radiation induced static component (SC, also referred to as quasi-static displacement pulse) was reported to depend on the material nonlinearity parameter (Cantrell, 1984). Later, it was confirmed that the SC generated by a primary longitudinal tone burst wave possesses a flat-top time-domain shape with its peak amplitude proportional to the propagation distance (Jacob *et al.*, 2006; Nagy *et al.*, 2013).

Regarding the propagation of guided waves, the static component generation (SCG) by primary Lamb waves propagating in plates with weak quadratic nonlinearity was recently reported to possess certain unique properties (Wan *et al.*, 2018; Sun *et al.*, 2018). First, it was demonstrated that the generated SC (also referred to as quasi-static displacement pulse) from a primary Lamb wave propagating in a plate with quadratic nonlinearity shares the characteristic of S0 mode. The SC is polarized in the primary wave propagation direction with only in-plane displacement. Second, it was shown that, whether the phase velocity of the primary Lamb wave matches with that of the SC or not, the energy of the SC increases with the propagation distance of the primary wave. That means a cumulative SCG by primary Lamb waves does not need to satisfy the synchronism condition as required by second harmonic generation (SHG). Given these features, using SCG by Lamb waves is attractive for early materials testing and evaluation due to flexible mode selection and low attenuation in measurements.

However, little literature is available on the SCG by primary shear horizontal guided waves. In regard to the propagation of a primary shear horizontal guided wave in a plate with quadratic nonlinearity, properties including mode and temporal waveform of the potentially produced SC have yet to be revealed. It is known that, for guided wave based ultrasonic testing and structure health monitoring, choosing the primary wave mode and the fundamental frequency usually requires careful consideration (Mitra and Gopalakrishnan, 2016). Optimized mode and frequency of guided waves are always desired in order to enhance the signal-to-noise ratio in practical applications. In the case where non-low-frequency S0 mode is chosen, it is expected that a group velocity mismatch (GVM) existing between the primary guided wave and the produced SC can impact the time-domain shape of the SC. Assuming the SC pulse was separated from the primary guided wave after traveling a certain distance due to the GVM, the measure of SC pulse by lead zirconic titanate based transducers (PZTs) can be troublesome. Setting optical measurement methods aside, existing experimental studies concerning the measure of SCG by PZTs employ either a bulk wave (Narasimha *et al.*, 2007; Deng, 2020) or a low-frequency S0 Lamb wave (Sun *et al.*, 2020) as the primary wave, of which the group velocity is matched with the SC. In those cases, the

a)Author to whom correspondence should be addressed.

measured primary wave that is coupled with the SC pulse exhibits an asymmetry in time domain. That makes the extraction of SC pulse possible. However, regarding the SCG by primary guided waves with GVM, a lack of effective measurement methods based on PZTs can restrict the applications of SCG.

This study is twofold: one aim is to investigate the SCG by both primary Lamb and shear horizontal guide waves, and another aim is to provide a feasible method for measuring SCG by guided waves with GVM based on PZTs. The outline of this paper is as follows. In Sec. 2, basic characteristics of the generated SC from primary S0, A0, and SH0 modes are checked. The effect of GVM on the time-domain waveform of the produced SC is revealed and discussed. In Sec. 3, a wave modulation and superposition method is proposed. The effectiveness of the method is verified by a numerical simulation, wherein two counter-propagating primary shear horizontal waves are modulated and superposed to generate a measurable alternating current (ac) displacement signal related to the SCG.

2. SCG by guided waves with GVM

2.1 Numerical investigations

The following numerical simulations are implemented by COMSOL Multiphysics software (V5.5). The material is aluminum with a built-in Murnaghan hyper-elastic model applied. The S0 and A0 Lamb waves are simulated using a two-dimensional (2D) plane strain model as shown in Fig. 1(a). The length of the plate is 1.6 m for the S0 wave simulation and 0.4 m for the A0 wave simulation. A displacement-prescribed boundary condition is applied to the left end, and a fixed constraint is applied to the right end. The excitation directions of S0 and A0 modes are in the x- and y-direction, respectively. For simulating the SH0 wave, a simplified three-dimensional (3D) model is used to reduce the computational cost. As shown in Fig. 1(b), the length of the model is 0.4 m. One layer of elements is contained in the width direction. Periodical continuity boundary conditions are assigned to the front and back surfaces to simulate the plane strain condition. The excitation direction of the SH0 mode is along the y-direction. For these three simulations, the thickness of the model is 1 mm. The excitation signal is a Hanning windowed 10-cycle sinusoidal tone burst, of which the maximum amplitude is 100 nm. The frequency is $f = 1$ MHz. The maximum mesh size is $\lambda/20$, where λ is the wavelength of the corresponding primary guided wave. The time step of the transient solver is set as $1/20f$ to ensure the accuracy of the simulation. Domain point probes are set on the top surface of the plate at different locations to extract the displacement component signals in different directions. For the case of the 2D finite-element method (FEM) model, U_1 and U_2 denote the displacement components in the x- and y-direction, respectively. Similarly, U_1, U_2, and U_3 denote the displacement components in the x-, y-, and z-direction, respectively, for the 3D FEM model.

2.2 Results and discussion

In the S0 wave excitation case, the displacement components in the x- (U_1) and y-directions (U_2) are extracted and processed by a 200 kHz low-pass filter. It is found that the quasi-static pulse extracted in the x-direction ($\bar{U}_1$) is about 2 orders of magnitude larger than that extracted in the y-direction ($\bar{U}_2$). The $\bar{U}_1$ has a uniform displacement profile along the thickness direction of the plate. Also, the group velocities of the primary wave and the generated SC are about 5200 and 5342 m/s, respectively, according to the time signals obtained at different locations shown in Figs. 2(a) and 2(b). This confirms that the generated SC from a 1 MHz primary S0 wave is zero-frequency S0 mode. Since the difference in group velocity is small (about 3%), the amplitude of the SC first increases with the propagation distance as shown in Fig. 2(a). However, it stops increasing after the primary S0 wave further lags behind the generated SC at a propagation distance longer than 500 mm. As shown in Fig. 2(b), while the power flux to SCG continues, the waveform of the quasi-static pulse is approximately a trapezoid with increasing width. In the A0 wave excitation case, SCG occurs in a similar way except that the cumulative effect is mostly evidenced by an increasing width of the SC due to a larger difference (about 42%) in group
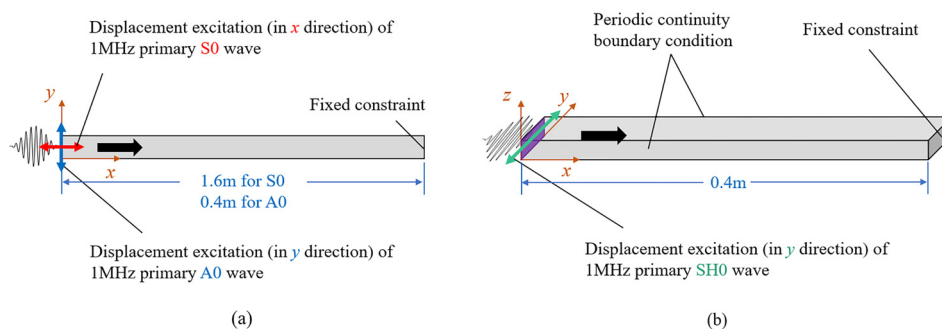

Fig. 1. (a) 2D FEM model for investigation of SCGs by 1 MHz primary S0 and A0 waves; (b) 3D FEM model for investigation of SCG by 1 MHz primary SH0 wave.
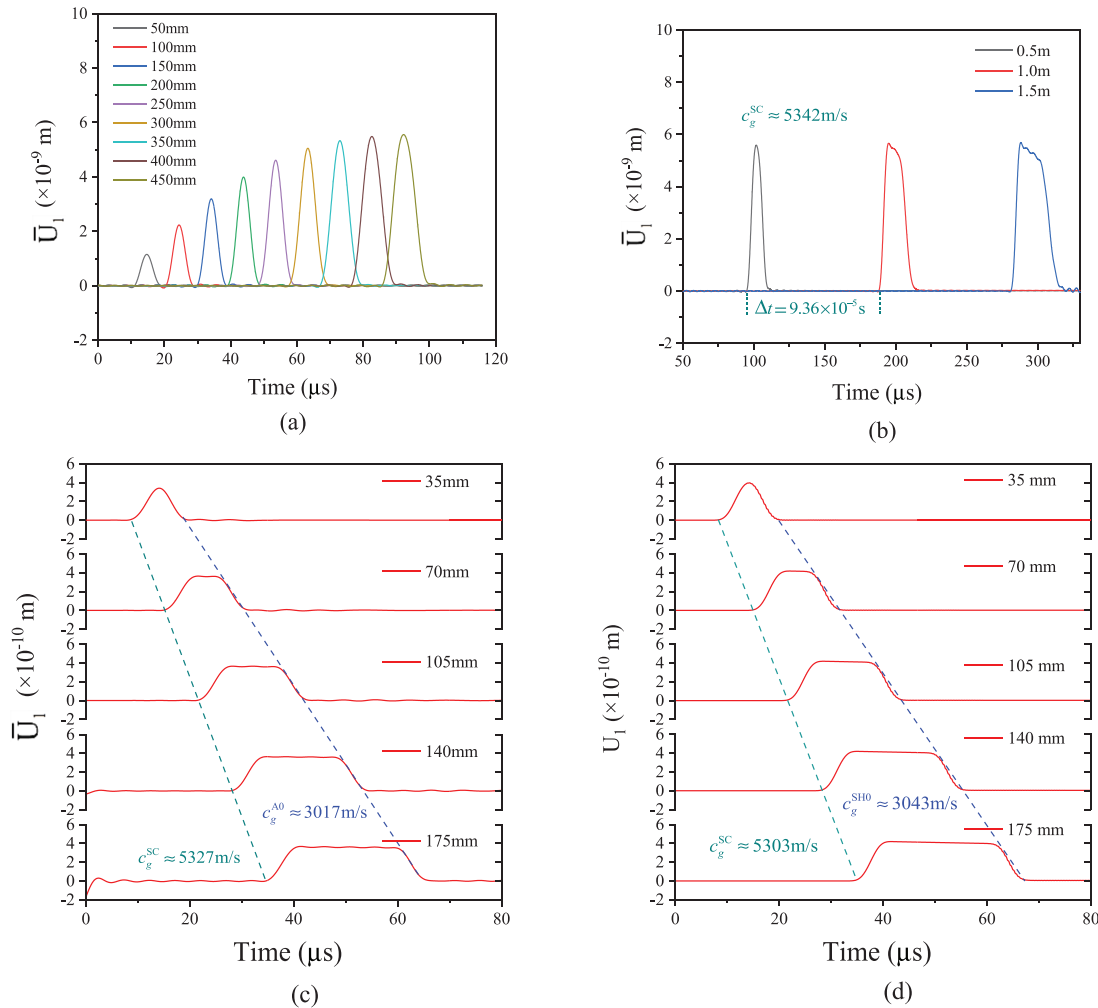
Fig. 2. Temporal waveforms of the SCs generated from different primary modes propagating at increasing distances: (a) the primary S0 mode propagating within 0.5 m, (b) the primary S0 mode propagating beyond 0.5 m, (c) the primary A0 mode propagating within 0.2 m, (d) the primary SH0 mode propagating within 0.2 m.

velocity. As shown in Fig. 2(c), the group velocities of the primary A0 wave and the SC are verified to be about 3017 and 5327 m/s, respectively. It is confirmed that the produced SC from the 1 MHz primary A0 wave is zero-frequency S0 mode.

As to the SH0 wave excitation case, Fig. 2(d) presents the time-domain displacement signals extracted in the x-direction (U_1) at different locations without being processed by a low-pass filter. It is found that the SC generated from a 1 MHz primary SH0 wave is also zero-frequency S0 mode. The group velocities of the primary SH0 wave and the SC are verified to be about 3043 and 5303 m/s, respectively. Thus far, it is further confirmed that the SC generated from all primary guided wave modes in plates with quadratic nonlinearity is S0 mode.

For nonlinear guided wave applications based on SCG, employing a primary low-frequency S0 mode makes the measurement of the generated SC by PZTs convenient. The SC is closely coupled with the primary wave, resulting in a weak asymmetry in the time-domain signal received by the PZT. However, similar to the A0 and SH0 wave excitation cases, a significant GVM existing between the primary wave and the generated SC can cause the temporal waveform of the SC to increase in width soon after it travels a relatively short distance (about 35 mm). This raises the concern that, while the primary guided wave gradually gets separated from the generated SC due to GVM, the independently propagating SC is difficult to capture by PZTs.

3. Wave modulation and superposition method

3.1 Basic description and numerical investigation

A scheme proposed to measure SCG using PZTs with GVM is as follows. First, two intermittent signals $F_1(t)$ and $F_2(t)$ are used as inputs. As illustrated in Fig. 3(a), the two signals are modulated with specific features. During the excitation
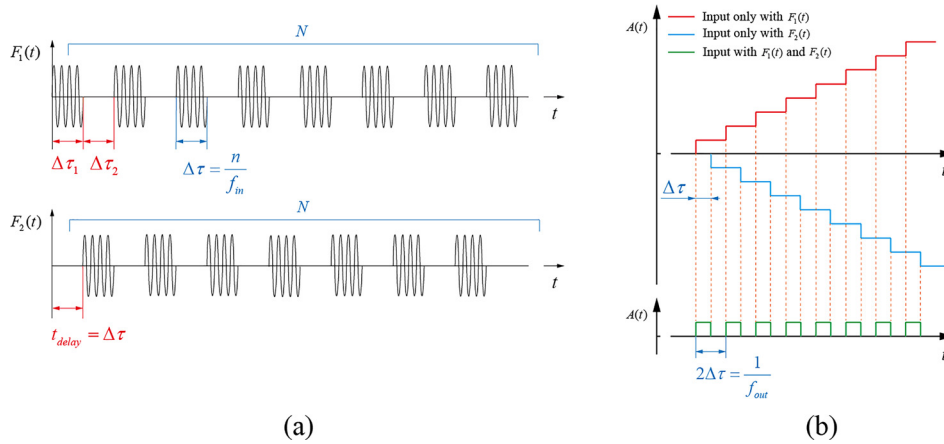
Fig. 3. Temporal waveform illustrations: (a) the designed intermittent signals for primary wave excitations and (b) the modulated and superposed SCs received at the center of the plate.

period ($\Delta\tau_1$), the frequency and the cycle number of the sinusoidal tone burst are denoted as f_{in} and n, respectively. For simplicity, the length of the rest period ($\Delta\tau_2$) is assumed to be the same as the excitation period ($\Delta\tau_1 = \Delta\tau_2 = \Delta\tau$). The number of tone bursts in an input signal is denoted as N. Second, the two intermittent pulse signals are employed to generate two counter-propagating primary guided waves from two sides of a plate. Two SCs with opposite displacement polarities are expected to be produced due to wave interaction with weak material nonlinearity. As illustrated in Fig. 3(b), for one of the two intermittent primary waves, as an excitation period starts, a newly generated SC is induced and superposed on the old ones. Consequently, the shape of the two SCs will be steps-like. It should be noted that the maximum amplitude of a propagating SC is limited by its propagation distance. Herein, this limitation is neglected for simplicity. Assuming the measurement location is at the center of the two excitation positions, a time delay $t_{delay} = \Delta\tau$ is supposed to be applied to one of the input signals to achieve the objective of this method. Finally, the interference of the two steps-like SCs will produce a low-frequency displacement signal with a small direct current (dc) component, which can be measured by PZTs. The main frequency of the measured signal is denoted as f_{out}. Through basic analysis, it can be confirmed that $f_{in} = 2n \cdot f_{out}$, while $f_{out} = 1/2\Delta\tau$ and $f_{in} = n/\Delta\tau$.

Specifically, f_{in}= 10 MHz, n= 10, and N= 10 are used in a numerical investigation to verify the feasibility of the method. Figure 4(a) shows the FEM model. The frequency of the received displacement signal at the center location of the plate (f_{out}) is supposed to be 0.5 MHz based on the above analysis.

3.2 Results and discussion

The propagating primary shear horizontal wave excited from the left end of the plate is extracted in the y-direction as shown in Fig. 4(b). Since the two newly generated SCs are polarized in the x-direction, they can be readily extracted without signal filtering. As shown in Fig. 4(c), the displacement signal extracted at the center of the plate (red line) is a low-frequency signal with approximately stabilized maximum amplitude. Its frequency is 0.5 MHz, confirmed by fast Fourier transform. This result is in agreement with the prediction described in Sec. 3.1. For comparison, when only one modulated primary wave is excited, the signal extracted in the x-direction at the same location (blue line) contains a strong time-varying dc component. While the ac component resulting from the primary wave modulation is essential for measurements by PZTs, such a dc component, the magnitude of which irregularly changes with time, can exert a negative effect on the piezoelectric process. However, the superposition process of the two SCs, as another important part of the proposed method, can lead to a relatively stable and balanced vibration of the medium at the measuring point. This increases the signal-to-noise ratio and finally advantages the measure of SCG with GVM using only PZTs.

In addition, since PZTs are always of certain sizes in practical applications, signals measured along lines of different lengths at the center of the plate [dotted line shown in Fig. 4(a)] are averaged and presented in Fig. 4(d). As shown in the figure, the maximum amplitude of the averaged signal tends to decrease when increasing the line length. This suggests that smaller PZT is more sensitive for SCG measurement using the proposed method.

It is known that, due to different polarization directions, the generated SC can be more readily extracted from primary SH waves than from primary Lamb waves. However, in the proposed method, the GVM makes a large contribution to the separation of the primary wave and the generated SC. Owing to a relatively small group velocity, the 10 MHz primary SH waves start to be received at about $t = 35$ μs at $x = 0.1$ m. Therefore, through adjusting the f_{in}, n, and N parameters as described in Sec. 3.1, a total separation of the SCG-related nonlinear wave component from its primary waves can be achieved. Consequently, should primary Lamb waves with significant GVM (like A0 mode) be employed, such separation can be achieved similarly. Also, since high-frequency primary guided waves usually suffer significant
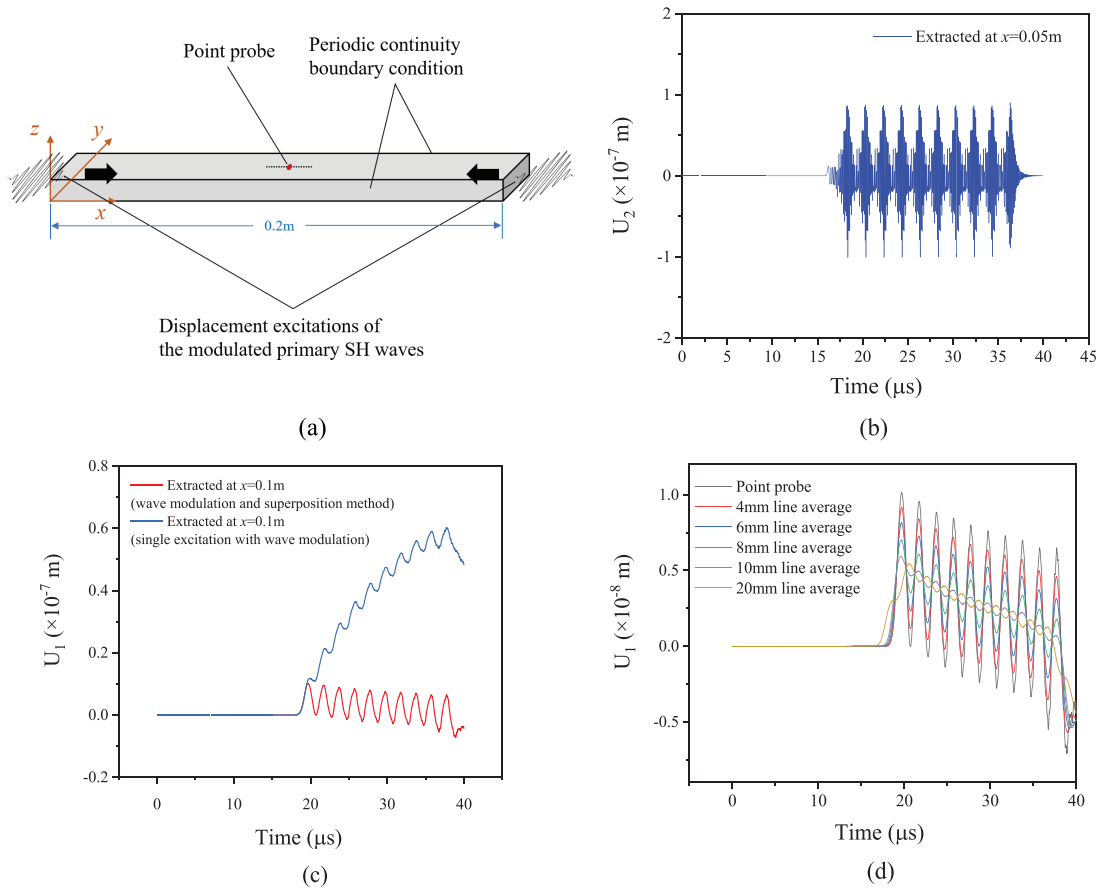
Fig. 4. (a) FEM model of the proposed method. (b) The modulated primary SH waves extracted in the y-direction. (c) The modulated SCs extracted in the x-direction with and without the superposition process. (d) Averaged time-domain signals measured on lines of different lengths set at the center of the plate in the x-direction.

attenuation, the SCG-related signal at a much lower frequency (f_{out}) can be promisingly measured with sufficient signal-to-noise ratio.

The above numerical simulations are based on the plane strain assumption, which neglects the divergence loss of SCG as discussed for longitudinal waves by Nagy et al. (2013). However, through optimizing the distance between the two excitation locations and relevant parameters (f_{in}, n, N, etc.), the practicability and cost-effectiveness of the proposed method can still be achieved for future applications.

4. Conclusion

In this study, the SCGs by both primary Lamb and shear horizontal guided waves in plates with quadratic nonlinearity have been reported. It has been found that the generated SC from a primary SH0 guided wave is S0 mode. Combining with the cases where S0 and A0 modes were employed as primary wave modes, it has been further confirmed that the SCs generated from guided waves in plates are all S0 mode. The effect of GVM existing between the primary guided wave and the corresponding generated SC has been revealed. The GVM causes the SC to increase in width rather than amplitude after the power flux from the primary guided wave to the SC reaches a certain level.

A GVM is one of the main factors that restrict the application of SCG by guided waves based on PZTs. Currently, although there are many guided wave modes in plates, only low-frequency S0 mode has been employed as the primary guided wave mode for practical nonlinear ultrasonic testing based on SCG. This study has proposed a feasible method to facilitate the measurement of SCG by PZTs under the condition of GVM. With the primary wave modulated by a low-frequency switch-signal, the generated SC of relatively large width is then modulated into a displacement signal with periodic vibration. By superposing two SCs individually generated from two modulated counter-propagating primary guided waves, a stabilized ac vibration displacement signal can then be measured by PZTs at a designable location. Consequently, the SCGs by primary wave modes with GVM can be exploited for nonlinear ultrasonic applications using this cost-effective method.

References and links

Cantrell, J. H. (**1984**). "Acoustic-radiation stress in solids. I. Theory," Phys. Rev. B **30**, 3214–3220.

Deng, M. X. (**2020**). "An experimental approach for detection of the acoustic radiation induced static component in solids," Chin. Phys. Lett. **37**, 074301.

Jacob, X., Takatsu, R., Barrière, C., and Royer, D. (**2006**). "Experimental study of the acoustic radiation strain in solids," Appl. Phys. Lett. **88**, 134111.

Kundu, T., Eiras, J. N., Li, W., Liu, P., Sohn, H., and Payá, J. (**2018**). "Fundamentals of nonlinear acoustical techniques and sideband peak count," in *Nonlinear Ultrasonic and Vibro-Acoustical Techniques for Nondestructive Evaluation*, edited by T. Kundu (Springer, Cham, Switzerland).

Mitra, M., and Gopalakrishnan, S. (**2016**). "Guided wave based structural health monitoring: A review," Smart Mater. Struct. **25**, 053001.

Nagy, P. B., Qu, J. M., and Jacobs, L. J. (**2013**). "Finite-size effects on the quasistatic displacement pulse in a solid specimen with quadratic nonlinearity," J. Acoust. Soc. Am. **134**, 1760–1774.

Narasimha, K. T., Kannan, E., and Balasubramaniam, K. (**2007**). "Simplified experimental technique to extract the acoustic radiation induced static strain in solids," Appl. Phys. Lett. **91**, 134103.

Sun, X., Ding, X., Li, F., Zhou, S., Liu, Y., Hu, N., Su, Z., Zhao, Y., Zhang, J., and Deng, M. (**2018**). "Interaction of Lamb wave modes with weak material nonlinearity: Generation of symmetric zero-frequency mode," Sensors **18**, 2451.

Sun, X. Q., Shui, G. S., Zhao, Y. X., Liu, W., Hu, N., and Deng, M. (**2020**). "Evaluation of early stage local plastic damage induced bending using quasi-static component of Lamb waves," NDT E Int. **116**, 102332.

Wan, X., Tse, P. W., Zhang, X., Xu, G., Zhang, Q., Xu, G., Zhang, Q., Fan, H., Mao, Q., Dong, M., Wang, C., and Ma, H. (**2018**). "Numerical study on static component generation from the primary Lamb waves propagating in a plate with nonlinearity," Smart Mater. Struct. **27**, 045006.

29 December 2023 10:53:49

Chapter 4: Quasistatic Pulse Generation of Ultrasonic Guided Waves Propagation in Composites

4.1. Introduction, Significance, and Commentary

To further explore the QSC generation in anisotropic materials, this study employs the finite element method and conducted systematic numerical simulations on the QSC generation by guided wave in fiber reinforced composite thin plates. Intuitive perspectives of the generation, propagation, and mode conversion of the nonlinear QSC pulse wave in the composites are obtained. Different analyzing and signal processing methods are adopted for confirming the features of QSC. The results provide important guidance for developing future material characterization applications and microdamage evaluation applications in anisotropic materials.

4.2. Publication

This section is presented as published research paper by **Chang Jiang**, Weibin Li, Mingxi Deng, Ching-Tai Ng (2022) Quasistatic pulse generation of ultrasonic guided wave propagation in composites, *Journal of Sound and Vibration* 524:116764.

Statement of Authorship

Title of Paper	Quasistatic pulse generation of ultrasonic guided wave propagation in composites
Publication Status	☑ Published ☐ Accepted for Publication ☐ Submitted for Publication ☐ Unpublished and Unsubmitted work written in manuscript style
Publication Details	Chang Jiang, Weibin Li, Mingxi Deng, et al. (2022) Quasistatic pulse generation of ultrasonic guided wave propagation in composites, Journal of Sound and Vibration 524:116764.

Principal Author

Name of Principal Author (Candidate)	Chang Jiang		
Contribution to the Paper	Methodology, Investigation, Data curation, Visualization, Writing - Original Draft		
Overall percentage (%)	80		
Certification:	This paper reports on original research I conducted during the period of my Higher Degree by Research candidature and is not subject to any obligations or contractual agreements with a third party that would constrain its inclusion in this thesis. I am the primary author of this paper.		
Signature		Date	2023.12.29

Co-Author Contributions

By signing the Statement of Authorship, each author certifies that:

i.   the candidate's stated contribution to the publication is accurate (as detailed above);

ii. permission is granted for the candidate in include the publication in the thesis; and

iii. the sum of all co-author contributions is equal to 100% less the candidate's stated contribution.

Name of Co-Author	Weibin Li		
Contribution to the Paper	Conceptualization, Resources, Writing - Review & Editing, Supervision, Funding acquisition		
Signature		Date	2023.12.29

Name of Co-Author	Mingxi Deng		
Contribution to the Paper	Resources, Writing - Review & Editing, Supervision		
Signature		Date	2023.12.29

Name of Co-Author	Ching-Tai Ng		
Contribution to the Paper	Writing - Review & Editing, Supervision		
Signature		Date	2023.12.29

Please cut and paste additional co-author panels here as required.

Quasistatic pulse generation of ultrasonic guided waves propagation in composites

Chang Jiang [a,c], Weibin Li [a,*], Mingxi Deng [b,*], Ching-Tai Ng [c]

[a] *School of Aerospace Engineering, Xiamen University, Xiamen, Fujian, China*
[b] *College of Aerospace Engineering, Chongqing University, Chongqing, China*
[c] *School of Civil, Environmental, and Mining Engineering, University of Adelaide, Adelaide, South Australia, Australia*

A B S T R A C T

In this paper, the generation of quasistatic pulses (QSPs) of guided waves propagation in fiber reinforced plastic (FRP) thin plates is investigated. Numerical perspective of the generation, propagation, and mode conversion of QSPs of GWs in the composites are obtained. It is indicated that the displacement direction and generation efficiency of QSPs depend on the wave propagation direction, the coefficients of the strain energy function, and the primary GW field. Group velocity, wave structure, and wavenumber domain analyses show that the generated QSPs are either S0 mode, or partly coupled S0 and SH0 modes with only in-plane displacements with different direction, regardless of the excitation of primary waves. For GWs propagation in principal material directions, comparative studies show that the generation efficiency of QSPs are depended on both the mode types and primary GW propagation direction. With the considerations of both cumulative effect and the divergence effect, comparative study of generation efficiency of QSP and second harmonics shows that, although the divergence loss is not negligible, appropriate excitation of primary GW can achieve a higher efficiency of cumulative QSP generation than that of the phase matched second harmonics.

1. Introduction

Fiber reinforced polymer (FRP) composites have been widely employed due to their high strength to weight ratio and attractive stiffness properties [1,2]. The inspection and evaluation of FRP materials are imperative for ensuring the safety of high-value infrastructure and assets. Among many nondestructive evaluations (NDE) and structural health monitoring (SHM) techniques, cost-effective inspection methods based on ultrasonic waves have been widely studied and applied for decades [3–5]. In particular, nonlinear guided wave (GW) techniques can be used to characterize microstructural changes of material and identify micro-damages. Studies on the higher harmonics generation and GW mixing of different GWs in various materials were conducted and a wide range of relevant applications were developed in recent years [6–8].

However, there are challenges for using higher harmonics and mixed-frequency combinational harmonics in solids with weak nonlinearity. The well-known synchronism and nonzero power flux conditions are required for generating cumulative harmonics to ensure they are strong enough to be exploited [9–14]. The synchronism condition limits the mode pair selection, especially for composite structures and materials wherein the dispersion features of GWs can be fairly complex and intractable for the development
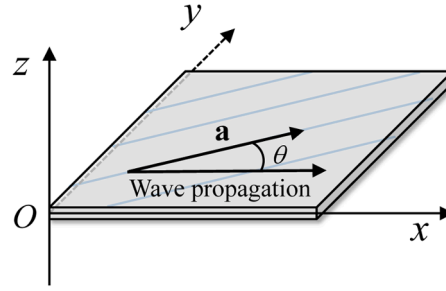
Fig. 1. Coordinate system and wave propagation scheme in FRP thin plates. (Color online).

of GW based NDE and SHM techniques. The relative strong anisotropic characteristics and high level of attenuation of wave propagation in FRP materials usually lead to low signal-to-noise ratio (SNR) of these nonlinear GW techniques.

Due to the relatively low attenuation of QSP at quite low frequency (QSP's carrier wave frequency is zero), the use of QSP has a potential for NDE and SHM of highly attenuative composite structures. This research focuses on the QSP generation of ultrasonic GWs propagation in FRP thin plates. The acoustic radiation induced QSP was first explored by Thurston and Shapiro [15], then studied by Cantrell et al. [16–22]. Theoretical, numerical and experimental investigations on the bulk wave related QSP generation in isotropic solids were carried out in the literature [23–25]. Also, the QSP generation by primary GWs modes in metallic thin plates were numerically and experimentally studied by Wan et al. [26], Sun et al. [27], and Jiang et al. [28]. It was found that the generated static component is zero-frequency fundamental symmetric mode, and is cumulative regardless of the synchronism condition. However, for anisotropic FRP materials, rare literature on the QSP generation by either bulk waves or GWs can be found. The complex dispersion characteristics of GWs and the anisotropy of materials complicate the QSP generation. Since the QSP generation is intrinsically associated with the elastic nonlinearity of materials, the detection with high SNR is worth investigation for developing nonlinear NDE techniques, especially considering its low attenuation feature in composite materials.

In this paper, numerical perspectives on QSP generation of different types of GWs propagating in different directions in an anisotropic composite plate are obtained and discussed. The mode, temporal waveform, and propagation characteristics of QSPs are analysed and given. Theoretical analysis on the QSP generation by GWs propagation in transversely isotropic plates is first provided. By finite element (FE) simulation, intuitive time domain QSP signals are obtained, and the generation efficiency of QSP are compared. Additionally, the divergence loss of QSP induced by finite-size excitation is studied and compared with the second harmonic generation. Important factors such as the group velocity mismatch, the selection and excitation of primary GWs, and the propagation direction of primary GWs are analysed regarding the generation efficiency of QSPs in composite plates. The results obtained in this study provide physical insight and guidance for choosing appropriate mode pairs that benefit the measurability of QSP in composite plates. The fundamental understanding of the QSP generation in FRP materials is essential for development of QSP based NDE and SHM techniques in composite structures.

2. Theoretical fundamentals

2.1. QSP generation in unidirectional FRP plates

The reference configuration for analysing the QSP generation by ultrasonic GW propagation is defined in Fig. 1. The wave is assumed to propagate along the x axis. The fiber direction is denoted by a unit vector $\mathbf{a} = [\cos\theta, \sin\theta, 0]$. The displacement vector of the wave field is $\mathbf{u} = [u_1, u_2, u_3]$, and the displacement gradient tensor is $\mathbf{H} = \nabla\mathbf{u}$. To model the nonlinear elastic response of the unidirectional FRP thin plate, we consider a hyperelastic material model for the transversely isotropic (TI) material, which expresses the strain energy function as a function of the Lagrange strain tensor $\mathbf{E}$ as follows [29]:

$$
\begin{aligned}
W &= W\left(tr\mathbf{E}, tr\mathbf{E}^2, tr\mathbf{E}^3, \mathbf{a} \cdot \mathbf{Ea}, \mathbf{a} \cdot \mathbf{E}^2\mathbf{a}\right) = W_L + W_{NL}, \\
W_L &= \alpha_1(tr\mathbf{E})^2 + \alpha_2(tr\mathbf{E})(\mathbf{a} \cdot \mathbf{Ea}) + \alpha_3(tr\mathbf{E}^2) + \alpha_4(\mathbf{a} \cdot \mathbf{Ea})^2 + \alpha_5(\mathbf{a} \cdot \mathbf{E}^2\mathbf{a}), \\
W_{NL} &= \beta_1(tr\mathbf{E})^3 + \beta_2(tr\mathbf{E})\left(tr\mathbf{E}^2\right) + \beta_3(tr\mathbf{E})(\mathbf{a} \cdot \mathbf{Ea})^2 \\
&\quad + \beta_4(tr\mathbf{E})\left(\mathbf{a} \cdot \mathbf{E}^2\mathbf{a}\right) + \beta_5(tr\mathbf{E})^2(\mathbf{a} \cdot \mathbf{Ea}) + \beta_6\left(tr\mathbf{E}^2\right)(\mathbf{a} \cdot \mathbf{Ea}) \\
&\quad + \beta_7\left(tr\mathbf{E}^3\right) + \beta_8(\mathbf{a} \cdot \mathbf{Ea})^3 + \beta_9(\mathbf{a} \cdot \mathbf{Ea})\left(\mathbf{a} \cdot \mathbf{E}^2\mathbf{a}\right) + O\left(\mathbf{E}^4\right).
\end{aligned}
\tag{1}
$$

Based on the constitutive relation in terms of the second Piola-Kirchhoff stress ($\mathbf{S}$) and the Lagrange strain ($\mathbf{E}$)

$$
\mathbf{S}(\mathbf{E}) = \frac{\partial(W_L + W_{NL})}{\partial\mathbf{E}},
\tag{2}
$$

the linear coefficients α_i ($i = 1, 2, \ldots, 5$) and the nonlinear coefficients β_i ($i = 1, 2, \ldots, 9$) can be determined by inverting

Table 1
Coefficients of the strain energy function W_L. (Unit: GPa).

α_1	α_2	α_3	α_4	α_5
2.25	1.7	4.65	48.8	2.1

$$C_{ijkl} = \frac{\partial^2 W_L}{\partial E_{ij} \partial E_{kl}},$$
$$C_{ijklmn} = \frac{\partial^3 W_{NL}}{\partial E_{ij} \partial E_{kl} \partial E_{mn}}, \tag{3}$$

where C_{ijkl} and C_{ijklmn} are the second order and third order elastic stiffness tensor, respectively. The first Piola-Kirchhoff stress tensor **P** is related to **S** by

$$\mathbf{P}(\mathbf{H}) = (\mathbf{I} + \mathbf{H})\mathbf{S}(\mathbf{H}), \tag{4}$$

where **I** is the identity tensor. Thus, the displacement equation of motion and the boundary condition for the traction-free plate is expressed as

$$\rho \frac{\partial^2 \mathbf{u}}{\partial t^2} - \nabla \cdot \mathbf{P}^{\mathrm{L}}(\mathbf{H}) = \nabla \cdot \mathbf{P}^{\mathrm{NL}}(\mathbf{H}),$$
$$\mathbf{P}(\mathbf{H}) \cdot \mathbf{n}_z = 0, \tag{5}$$

where ρ is the mass density, and $\mathbf{n}_z$ is a unit vector along the z axis. Using a second order perturbation method, the whole GW field can be decomposed as $\mathbf{u} = \mathbf{u}^{(1)} + \mathbf{u}^{(2)}$, and the primary GW is expressed as $\mathbf{u}^{(1)} = \mathbf{u}^{(1)}(z)\exp[j(kx - \omega t)]$. The equation of motion is then decomposed into

$$\rho \frac{\partial^2 \mathbf{u}^{(1)}}{\partial t^2} - \nabla \cdot \mathbf{P}^{\mathrm{L}}\left(\nabla \mathbf{u}^{(1)}\right) = 0,$$
$$\rho \frac{\partial^2 \mathbf{u}^{(2)}}{\partial t^2} - \nabla \cdot \mathbf{P}^{\mathrm{L}}\left(\nabla \mathbf{u}^{(2)}\right) = \mathbf{F}^{(2)}, \tag{6}$$

where $\mathbf{F}^{(2)} = \mathbf{F}[\mathbf{u}^{(1)}(z)] = \nabla \bullet \mathbf{P}^{\mathrm{NL}}(\nabla \mathbf{u}^{(1)})$ represents the second-order bulk driving force term. Also, there exists the second-order traction stress tensor $\mathbf{P}^{(2)} = \mathbf{P}[\mathbf{u}^{(1)}(z)]$ on the top and bottom surfaces of the plate. According to the modal analysis approach for GW excitation, $\mathbf{F}^{(2)}$ and $\mathbf{P}^{(2)}$ can be regarded as the bulk source and surface source for generation of secondary GWs.

Specifically, we only consider the zero-frequency component in the secondary wave field other than the double-frequency harmonic, which is associated with the zero-frequency component of $\mathbf{F}^{(2)}$ and $\mathbf{P}^{(2)}$ (denoted by $\mathbf{f}^{(0\omega)}$ and $\mathbf{p}^{(0\omega)}$). For finite-duration excitation of a primary GW, the function of the finite-duration $\mathbf{f}^{(0\omega)}$ and $\mathbf{p}^{(0\omega)}$ at each position that the primary GW propagates through, is to generate a series of finite-duration zero-frequency components. Finally, the QSP received by the probe can be regarded as the summation of these zero-frequency components in space [30].

2.2. Generation efficiency of QSP

Since the QSP generation is directly associated with the $\mathbf{f}^{(0\omega)}[\mathbf{u}^{(1)}(z)]$ and $\mathbf{p}^{(0\omega)}[\mathbf{u}^{(1)}(z)]$, the generation efficiency is deducted as dependent on the field distribution $\mathbf{u}^{(1)}(z)$ of the primary GW (determined by the dispersion relation with the driving frequency ω and phase velocity c_p^ω), as well as the coefficient $B(\theta)$ (a function of the fiber direction θ and the elastic coefficients α_i and β_i). Consequently, when the excitation frequency ω and amplitude A of the primary wave are given, a primary GW mode propagation with different fiber directions is expected to generate the QSP with different efficiencies. Also, different primary GW modes propagation with the same fiber direction could generate the QSP with different efficiencies.

For a primary low-frequency S0 mode propagating along principal material directions, the field distribution is analogous to that of the one-dimensional longitudinal plane wave, in which case the coefficient $B(\theta)$ is calculated as

$$B(0°) = \frac{-6\alpha_1 - 6\alpha_2 - 6\alpha_3 - 6\alpha_4 - 6\alpha_5 - 6\beta_1 - 3\beta_2 - 6\beta_3 - 4\beta_4 - 6\beta_5 - \frac{11}{2}\beta_6 - 6\beta_7 - 6\beta_8 - 6\beta_9}{(2\alpha_1 + 2\alpha_2 + 2\alpha_3 + 2\alpha_4 + 2\alpha_5)^2},$$
$$B(90°) = \frac{-6\alpha_1 - 6\alpha_3 - 6\beta_1 - 3\beta_2 - 6\beta_7}{(2\alpha_1 + 2\alpha_3)^2}. \tag{7}$$

Here, the displacement direction of the generated QSP is determined by the sign (positivity or negativity) of the coefficient $B(\theta)$, and the generation efficiency of QSP is represented by $|B(\theta)|$. For other GW modes and propagations along the non-principal material directions, the particle motions are quite complex, and the expression of $B(\theta)$ cannot be readily obtained.

Table 2

Coefficients of the strain energy function W_{NL}. (Unit: GPa).

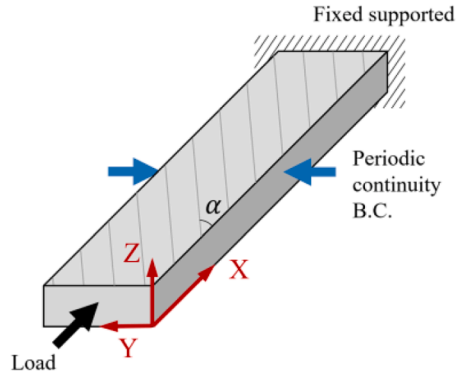| β_1	β_2	β_3	β_4	β_5	β_6	β_7	β_8	β_9
-9.65	-15.55	-10.20	-35.70	61.45	-18.95	-10.47	163.63	42.10

Fig. 2. Schematic of the 3D FE model. (Color online).
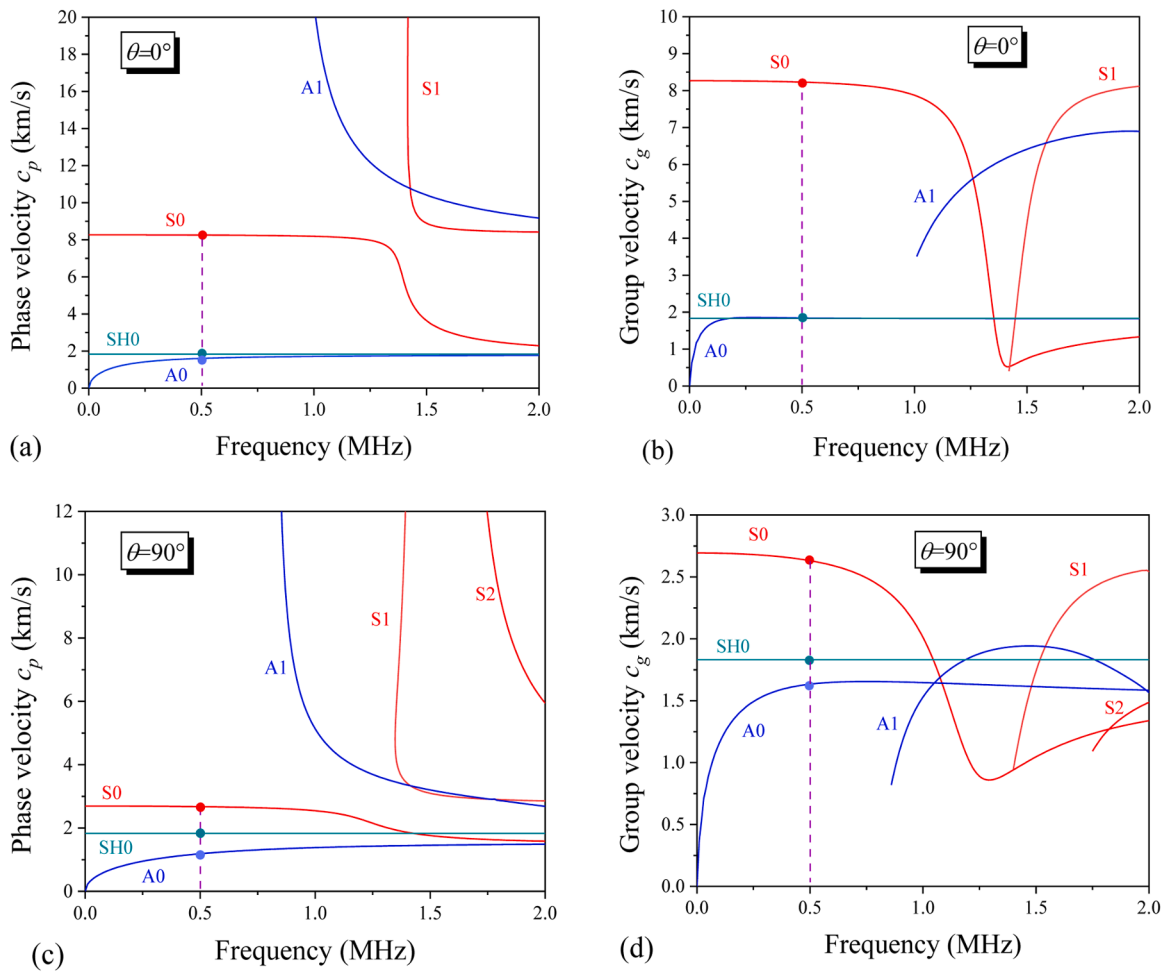
Fig. 3. Dispersion curves of GWs in the 1mm-thickness unidirectional FRP plate propagating along θ = 0° direction: (a) phase velocity, (b) group velocity; and along θ = 90° direction: (c) phase velocity, (d) group velocity. (Color online).
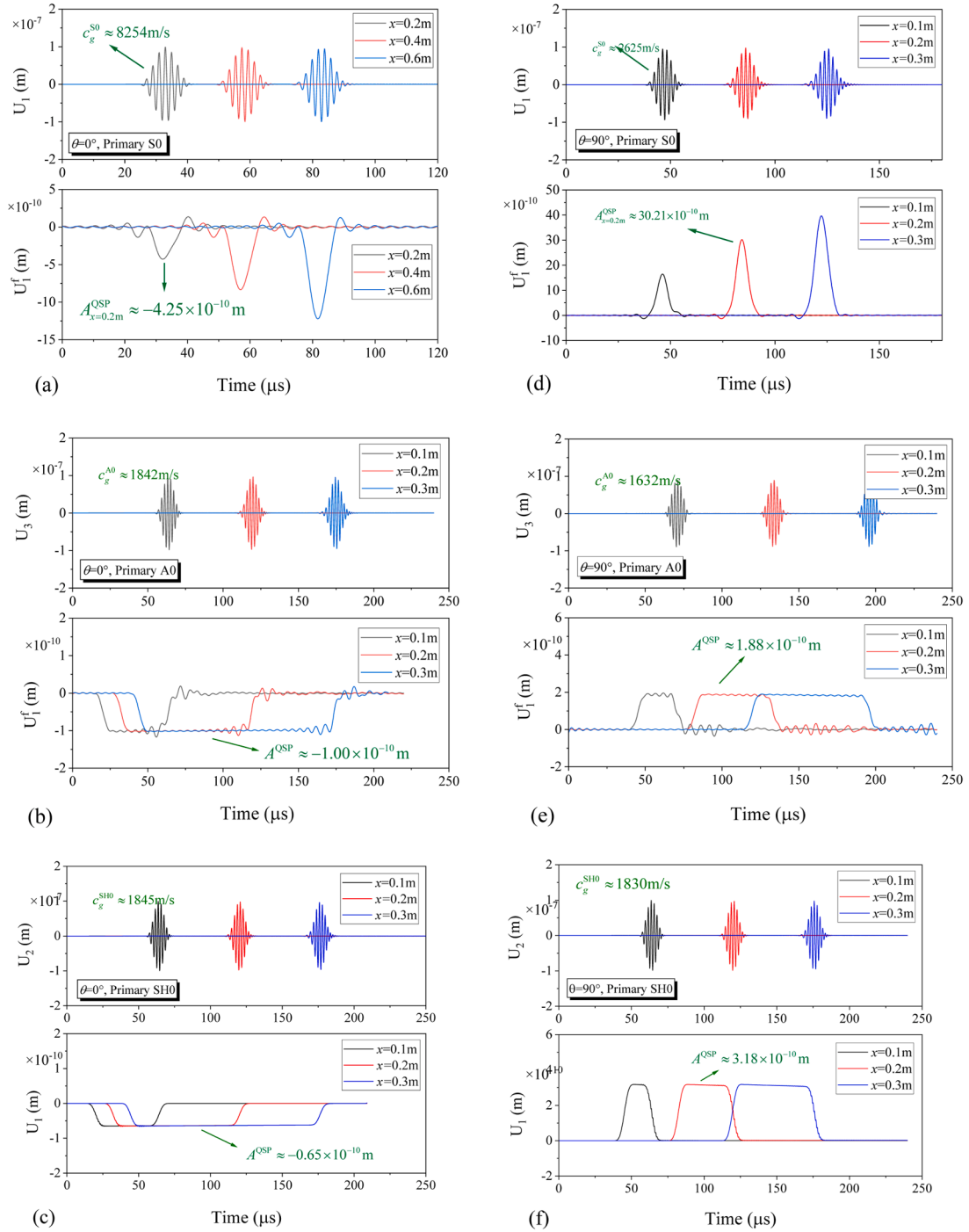
Fig. 4. Displacement signals extracted and processed for observing the primary GWs (upper parts) and the corresponding QSPs (lower parts). Propagations along θ = 0° direction: (a) primary S0, (b) primary A0, (c) primary SH0; and propagations along θ = 90° direction: (d) primary S0, (e) primary A0, (f) primary SH0. (Color online).

3. Numerical studies

3.1. Composite materials with quadratic nonlinearity

For the following FE simulations, the density of the unidirectional FRP plate is 1700 kg/m³. The linear coefficients α_i ($i = 1, 2, ..., 5$) are listed in Table. 1. Following Zhao et al. [29], the nonlinear coefficients β_i ($i = 1, 2, ..., 9$) in Eq. (1) are listed in Table. 2.
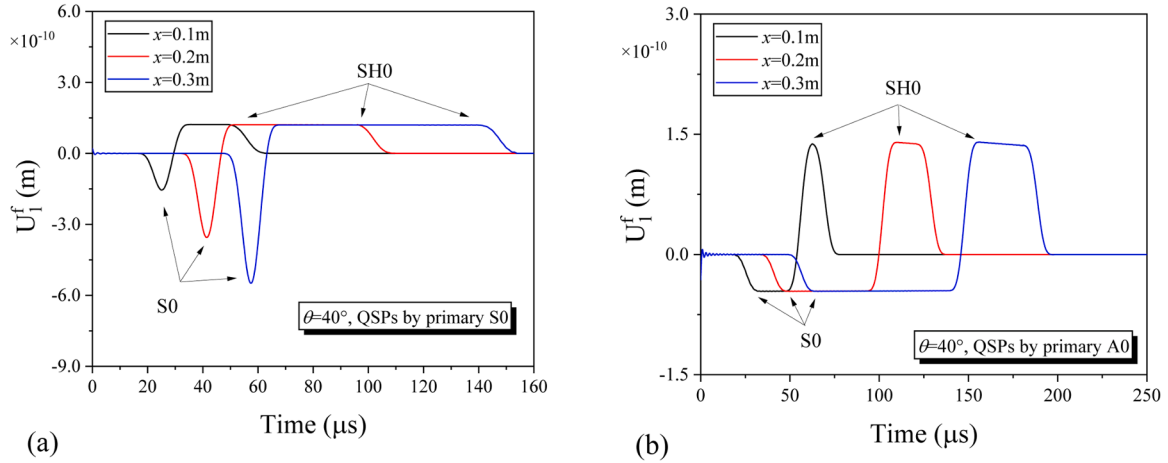
Fig. 5. QSP signals generated by primary GWs propagating along θ = 40°: (a) primary S0, (b) primary A0. (Color online).

Consequently, the coefficient $B(\theta)$ in Eq. (7) are calculated as $B(0°) = -0.10$ and $B(90°) = 0.66$.

For GWs propagation in FRP plates, the wave propagation direction might be different from the principal material directions. Therefore, by separately defining local material coordinate systems for each TI layer of the whole laminate, the wave propagation problems are simulated and analysed using a uniform global (*X, Y, Z*) coordinate system, wherein the wave propagation direction is chosen invariably along the X direction (see Fig. 2).

3.2. Finite element model

To study the QSP generation in FRP thin plates, a 3D FE model is used. The plate geometry, boundary conditions and the global (*X, Y, Z*) coordinate system are shown in Fig. 2. The angle between the fiber direction and the wave propagation direction is denoted as θ. The dimensions of the model are adjusted due to different wavelengths of different primary GW modes in the comparative studies. In general, the length of the model in X direction is chosen long enough so that the interference of the boundary reflected waves are prevented within the expected wave propagation time. The model is discretized with quadratic solid elements, of which the maximum size is determined by $\Delta e = \lambda/20$, where λ is the wavelength of the primary wave. The width of the model in Y direction is chosen as Δe. The periodic continuity boundary condition assigned to the lateral faces of the plate enables modeling wave propagation under a generalized plane strain condition.

The primary GW excitation is achieved by prescribing the load on the front face of the model. The load is a Hann windowed displacement signal, which is expressed by

$$F(t) = U/2 \cdot \sin(2\pi f t) \cdot [1 - \cos(2\pi f t / N)], 0 \le t \le N/f \tag{8}$$

where U denotes the maximum displacement amplitude (100 nm), f denotes the frequency (0.5 MHz), N is the cycle number (10) of the tone burst. The time step of the transient solver is $\Delta\tau = 1/20f$. For signal analysis and interpretation, the coordinates of the receiving probes are denoted as x, y and z. The displacement signals extracted in the X, Y and Z direction are represented by U_1, U_2 and U_3.

For θ = 0° and θ = 90° of a unidirectional 1.0 mm-thickness FRP plate, Fig. 3 shows the dispersion curves. Primary S0, SH0 and A0 waves at frequency 0.5 MHz are chosen for the comparative study of the QSP generation.

4. Results & discussion

The primary GWs are verified first by calculating their group velocities and comparing with the theoretical values. For θ = 0°, Fig. 4 (a)–(c) show the displacement signals extracted and processed for observing the propagating primary S0, A0, and SH0 (upper parts), respectively. The group velocity of the primary S0, A0, and SH0 waves are calculated as 8254 m/s, 1842 m/s, and 1845 m/s, respectively. For θ = 90°, Fig. 4(d)–(f) show the primary S0, A0, and SH0 (upper parts), respectively. The group velocities of the primary GWs are 2625 m/s, 1632 m/s, and 1830 m/s for S0, A0, and SH0 modes at 0.5 MHz, respectively. These results have good agreement with the dispersion curves, and validate the FE models.

4.1. Mode and waveform of QSP

First, the mode of the QSP is investigated based on group velocity, wave structure, and wavenumber domain analyses. The QSP signals generated by GWs propagation are obtained by extracting and processing the displacement signal U_1, which are plotted in the lower parts in Fig. 4. Since the primary S0 and A0 have displacements in the X directions as well, the corresponding U_1 are filtered using a 200 kHz low-pass filter, and are denoted by U_1^f. For θ = 0°, the calculated group velocities of the initial parts of the QSPs from
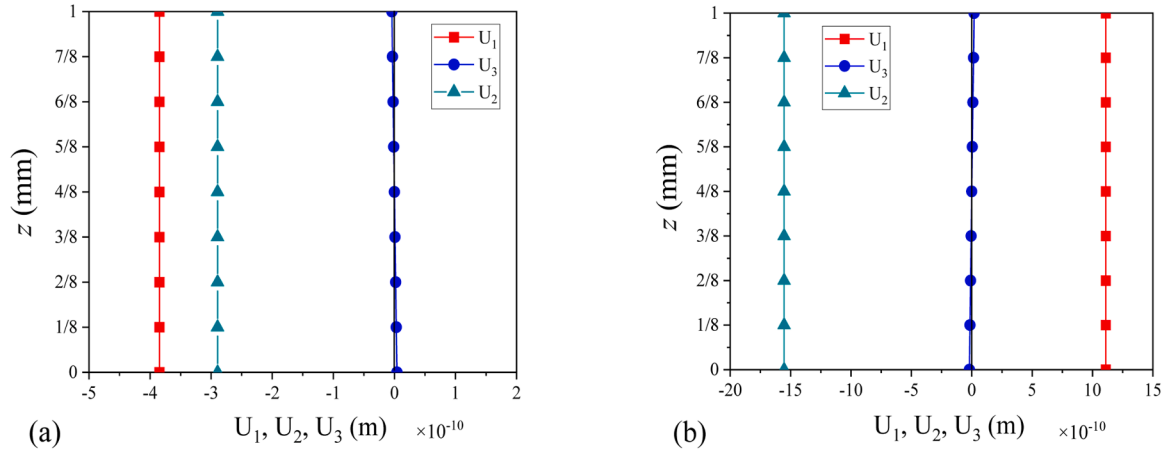
Fig. 6. Wave structures of the QSP signals extracted by probes at locations of different depths z: (a) the fast QSP of S0 mode, and (b) the slow QSP of SH0 mode. (Color online).
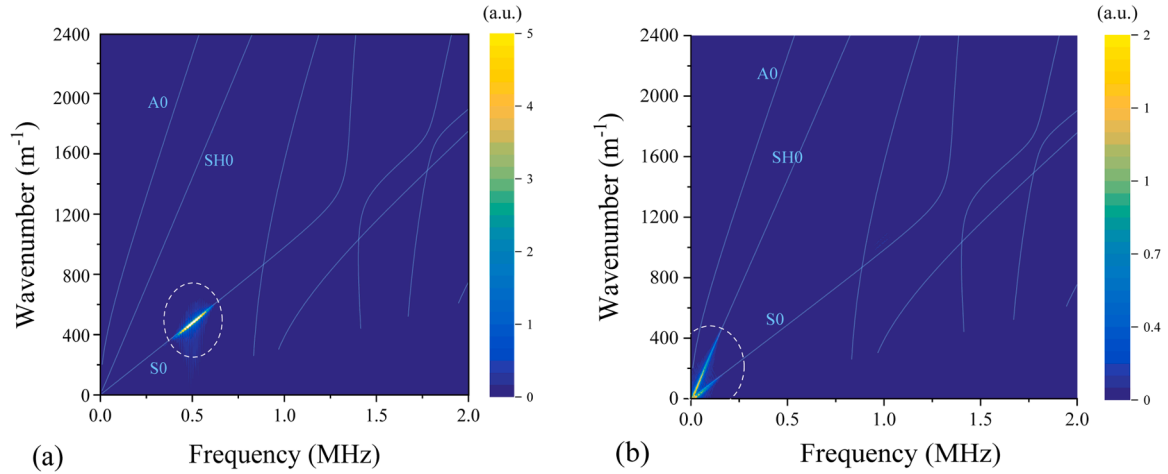

Fig. 7. Wavenumber-frequency domain analyses: (a) the primary S0 at frequency 0.5 MHz, (b) the QSPs of mode S0 and SH0. (Color online).

primary S0, A0, and SH0 are about 8271 m/s, 8270 m/s, and 8270 m/s, respectively. This value of group velocity consists with that of S0 mode at zero frequency, which indicates that the QSP generated from different GW modes are S0 mode. We note from Fig. 4 that the last parts of the QSP signals have the same group velocities with the corresponding primary GWs. This is because the QSP generation is directly associated with the propagation of the primary GW tone burst. For $\theta = 90°$, the group velocities of the generated QSPs from the three different GW modes are about 2700 m/s, which is also identical to that of the zero-frequency S0 mode.

For primary GWs propagating along non-principal material directions, Fig. 5(a) and (b) show the cases where $\theta = 40°$ and the QSPs are generated by primary S0 and A0 modes, respectively. The pure primary S0 and A0 modes which both have three non-zero displacement components in the *X, Y,* and *Z* direction are excited according to their wave structures. By combining the phase inversion method [31] and digital low-pass filtering, as shown in Fig. 5, there are two QSPs, of which the group velocities are about 6400 m/s and 2160 m/s. By referring to the dispersion curves, we confirm that the fast one is S0 mode at zero frequency and the slow one is SH0 mode at zero frequency. Further, Fig. 6(a) and (b) shows the wave structures of the two QSPs, respectively. It is observed that the QSPs both have relatively large in-plane displacements and zero out-of-plane displacements. The in-plane displacements are uniform along the thickness direction. Moreover, Fig. 7(a) shows the wavenumber domain of the primary S0 tone burst, and Fig. 7(b) shows the wavenumber domain of the simultaneously generated QSPs. While the primary S0 is counteracted, the nonlinear QSP signals become dominant, and their modes are verified as S0 and SH0. This simultaneous generation of two QSPs is quite different from that in isotropic materials. In isotropic thin plates, the generated QSP is always a single S0 mode.

Second, the waveform of QSP is analyzed. From Fig. 4, we observe that the displacement direction of the QSP depends on the fiber direction. For $\theta = 0°$, the QSPs generated from different GW modes are of different displacement, i.e., the direction of displacement is different from that of primary GW propagation. While for $\theta = 90°$, the displacement direction of QSP is the same as the GW propagation direction. This result consists with the theoretical analysis of QSP generation in Section 2.2. As the wave field of primary low-frequency
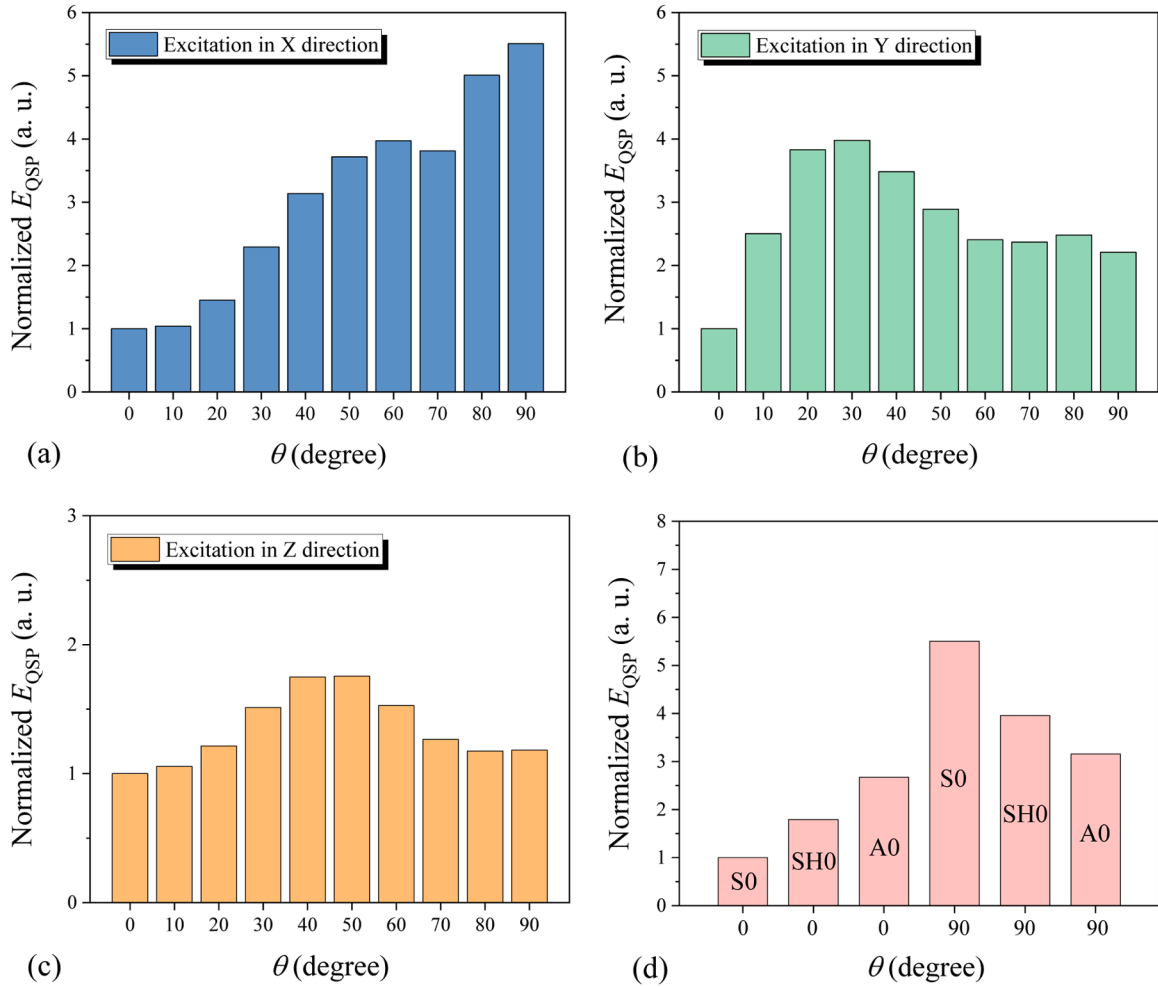
Fig. 8. Efficiency comparison of QSP generation by primary GW excitations along (a) X direction, (b) Y direction, (c) Z direction, (d) propagation in principal material directions. (Color online).

S0 mode is similar to that of a longitudinal plane wave, the sign of coefficient $B(0°)$ is negative, and $B(90°)$ is positive. As a result, the displacement of QSP by the primary S0 is in the different direction of GW propagation for $\theta=0°$, and in the same direction with GW propagation for $\theta = 90°$. This phenomenon is also unique comparing with QSP generation in metallic plates. The displacement direction of QSPs by all GWs in isotropic metallic plate are the same with the propagation direction [26,28].

In addition, the temporal waveform of QSP generated by a primary GW tone burst is affected by the group velocity mismatch. For primary GW whose group velocity matches with that of QSP, the waveform of QSP exhibits an envelope-like shape of the primary GW tone burst (Fig. 4(a) and (d)). The cumulative effect of QSP is evidenced by the increase of the amplitude verse the propagation distance. For other mode pairs with group velocity mismatch, the cumulative effect is also reflected by the increase of the pulse width. This result is similar to the case where the QSPs are generated from GWs propagating in isotropic metallic plates [26,28]. However, since isotropic plates have a constant acoustic nonlinear parameter β, the generated QSP from all GW modes are always a single mode of S0 at zero frequency. By contrast, there are two QSPs generated in the FPR plate when the propagation is not along the principal material direction. It is found that a primary GW tone burst propagating along the non-principal material direction can generate two different modes (S0 and SH0) of QSPs with the in-plane displacements in both the wave propagation direction and the shear horizontal direction as shown in Fig. 6. Moreover, due to the elastic anisotropy of the plate material, the two QSPs with different displacements in the propagation direction cannot be decoupled with each other, regardless of the propagation distance as shown in Fig. 5. This phenomenon of QSP generation is unique for anisotropic FRP plates. The coexistence and coupling of two QSPs of different modes can result in a polarity reversal and multiple jitters of the QSP signals, which can potentially benefit the measurement by piezoelectric sensors.
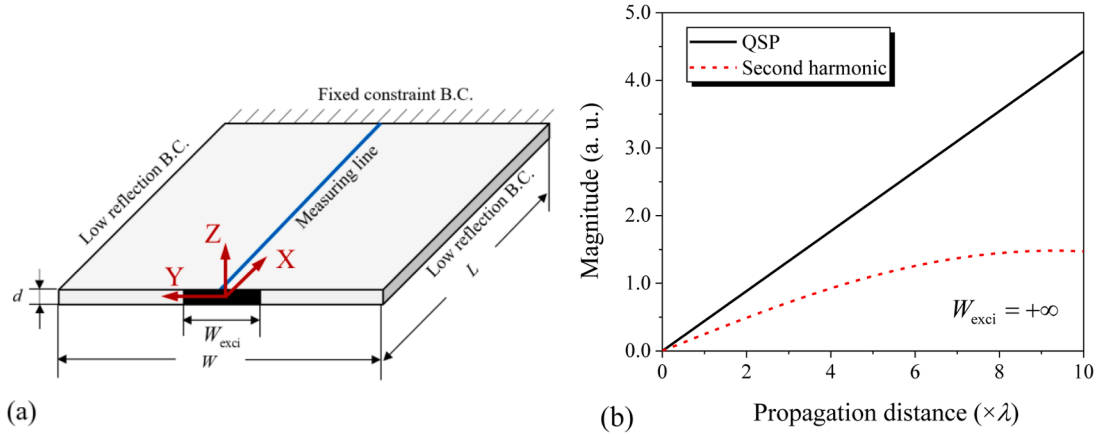
Fig. 9. (a) FE model for finite-size excitation source of primary S0 GW, (b) cumulative effects of QSP and second harmonic generated by plane S0 GW. (Color online).

4.2. Generation efficiency of QSP

Although the cumulative effect of QSP generation is regardless of the phase matching condition as required by the second harmonic generation, influences of the group velocity mismatch, the selection and excitation of primary GWs, and the propagation direction of primary GWs on the generation efficiency of QSPs in composite plates is worth investigation for optimization of GW mode pair choice and wave propagation direction in practical applications. Higher efficiency of QSP generation can lead to larger amplitude of the QSP measured at the same location, which improves the measurability and SNR of the QSP signal. Especially, when there is a significant group velocity mismatch between the primary GW and the QSP, the cumulative increase of the pulse width is vulnerable to random noises, and the increase of temporal amplitude is more meaningful.

First, we compare the generation efficiency of the two QSPs by the two primary S0 GWs at 0.5 MHz with $\theta = 0°$ and $\theta = 90°$. As shown in Fig. 3(b) and (d), the group velocities of these two primary S0 waves at 0.5 MHz both approximately matches with that of the generated QSPs at zero frequency. However, as shown in Fig. 4(a) and (d), the amplitudes of the two QSPs measured at $x = 0.2$ m are -4.25×10^{-10}m and 30.21×10^{-10}m for $\theta = 0°$ and $\theta = 90°$, respectively. The latter is about seven times larger than the former. This result approximately agrees with the theoretical prediction in Eq. (7). The calculated $|B(90°)|$ is about seven times larger than $|B(0°)|$ regarding the longitudinal wave propagation. Thus, with the low-frequency S0 GW tone burst excitation of the same amplitude, duration, and the approximate group velocity matching condition, the selection of $\theta = 90°$ can contribute to greater generation efficiency of QSP, which benefits practical measurement of the nonlinear signal.

Second, we compare the generation efficiency of the two QSPs by the primary A0 and SH0 GWs with $\theta = 0°$. As shown in Fig. 3(a) and (b), the group velocities of these two primary GWs are identical. The particle vibration directions are both perpendicular to the fiber direction. The phase velocity of SH0 is a little larger than that of A0 at 0.5 MHz. Consequently, the amplitude of the QSP generated by SH0 is little smaller than that by A0. As shown in Fig. 4(b) and (c), the QSPs by SH0 and A0 have a maximum amplitude of -0.65×10^{-10}m and -1.00×10^{-10}m, respectively. Thus, with the frequency, amplitude, duration, propagation direction, and the degree of group velocity mismatch of the primary GWs being the same, the generation efficiency of QSP is smaller for primary SH0 excitation than for A0 excitation. However, for $\theta = 90°$, although the phase velocity of primary SH0 is larger than that of A0 at 0.5 MHz, the generation efficiency of QSP by SH0 is a little larger than that by A0. This is confirmed by calculating the integrated amplitude of the QSPs in time domain. The reason can be that, for $\theta = 90°$, the particle vibration is along the fiber direction for SH0, while perpendicular to the fiber direction for A0.

Third, the generation efficiency of QSP by different primary GW modes propagating in directions ranging from 0° to 90° are investigated. Since there are two QSPs of mode S0 and SH0 when the primary GWs propagate along non-principal material directions, and the two QSPs have in-plane displacement in both *X* and *Y* directions, the generation efficiency of the QSP is then calculated by

$$E_{QSP} = \frac{\sqrt{\left(\int |U_1^{QSP}|\right)^2 + \left(\int |U_2^{QSP}|\right)^2}}{x}. \tag{9}$$

As shown in Fig. 8(a)–(c), the generation efficiency of QSP by primary GW excitation along the *X* direction becomes largest when the fiber direction is $\theta = 90°$. When the primary GW excitation is along *Y* and *Z* directions, the corresponding fiber directions for the largest generation efficiency of QSP are about $\theta = 30°$ and $\theta = 45°$, respectively. In particular, Fig. 8(d) shows the comparison for primary S0, SH0, and A0 GWs when the propagations are along principal material directions. The generation efficiency of QSP is largest for A0 and smallest for S0 when $\theta = 0°$, while the result of $\theta = 90°$ is the very opposite. Considering the complex features of GWs propagation in non-principal directions, the S0 mode with fiber direction $\theta = 90°$ is an optimized choice for the largest generation efficiency of QSP in practical applications.
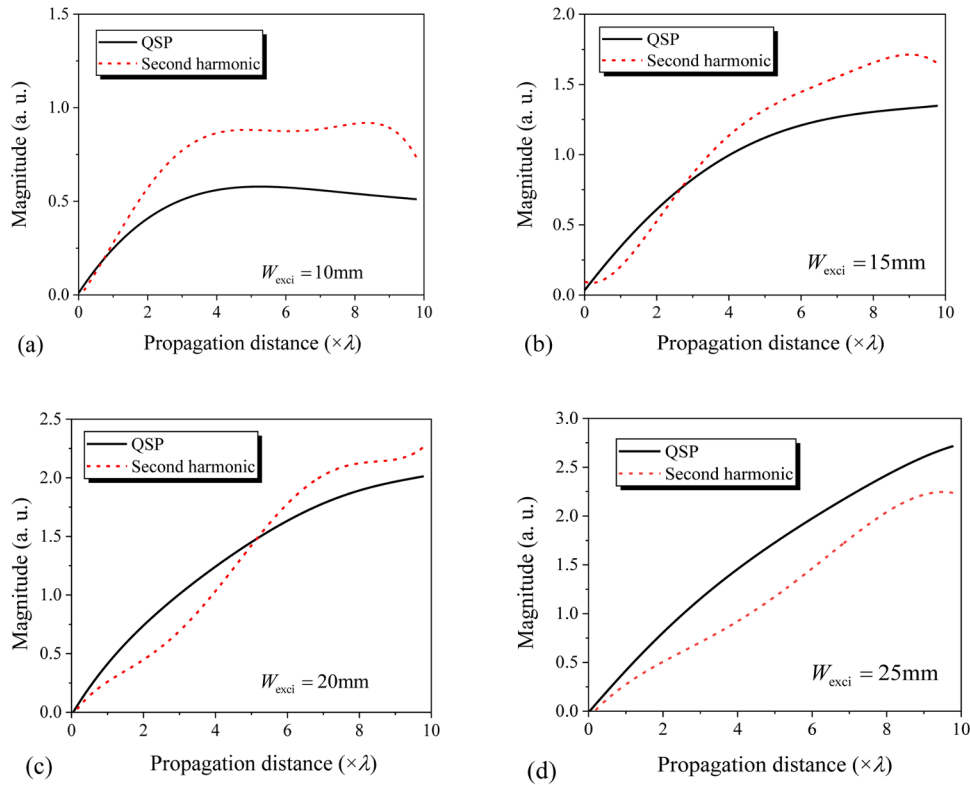
Fig. 10. Cumulative effects of the QSP and second harmonic of primary S0 GW using finite-size excitations: (a) $W_{exci} = 10$mm, (b)$W_{exci} = 15$mm, (c) $W_{exci} = 20$mm, (d)$W_{exci} = 25$mm. (Colour online)

4.3. Influence of excitation condition on QSP generation

Another import factor that can significantly affect the SNR of QSP in practical application is the divergence loss caused by the finite excitation size of primary GWs. Nagy et al. [21] investigated the finite-size effect on the QSP produced by a longitudinal wave in an isotropic solid. One of their main conclusions is that the divergence of the QSP wave is not negligible, even when the divergences of the fundamental and second harmonic are both negligible. Here, we simultaneously consider the QSP generation and second harmonic generation in a [0/90/0/90]s laminated FRP plate, and compare their cumulative effects. Fig. 9(a) shows the FE model. The dimensions are $d = 1.36$mm, $W = 50$mm, and $L = 300$mm. The primary S0 mode at 0.4 MHz with wavelength $\lambda = 15.33$mm is chosen, of which the second harmonic generation is under an approximate phase matching condition. The theoretical maximum cumulative distance of second harmonic is $\Delta\Lambda = 0.146$m. As a reference, Fig. 9(b) shows the comparison of cumulative effects of these two nonlinear signals generated by plane wave excitation.

As shown in Fig. 10(a), when $W_{exci} = 10$mm, the magnitude of the generated QSP is overall smaller than that of the second harmonic within a propagation distance of 0.15 m. This is very opposite to the case shown in Fig. 9(b) which is obtained under the plane wave excitation. Further, when $W_{exci} = 15$mm, the divergence loss of QSP is less and its magnitude at $x = 45$ mm becomes the same as that of the second harmonic. Moreover, the magnitude of QSP keeps increasing with the excitation size W_{exci} and is overall greater than that of the second harmonic when $W_{exci} = 25$mm. The divergence loss can be due to the poor directivity pattern of the QSP. When W_{exci}/λ is small, the main lobe of the directivity pattern of the QSP is wide, and the wave energy of QSP diminishes quicker than the second harmonic wave. However, the result shown in Fig. 10(d) indicates that, with relatively large-size excitation of primary waves, the measure of QSP can still be a feasible tool to characterize the change of relative material nonlinearity rendering higher SNR than second harmonic generation, especially when considering the fact that higher harmonics suffer much attenuation in practical applications.

5. Conclusion

The QSP generation of GWs in anisotropic FRP thin plates was investigated in this paper. Theoretical analysis on QSP generation of GW propagation in transversely isotropic thin plates was firstly conducted to show the factors that affected the displacement direction and generation efficiency of QSP. By FE simulations, the mode of the QSP generated by different primary GWs was confirmed as S0 or partly coupled S0 and SH0 modes with only in-plane displacement. The displacement direction of QSP was found to be related with the sign of the coefficient function $B(\theta)$. Further, for given excitation amplitude and frequency of the primary GW, the generation

efficiency of QSP varies with the GW propagation direction, as well as the primary mode type. Additionally, considering both the cumulative and divergence effects, obtained results clearly indicate that, a higher efficiency of cumulative QSP generation than that of a phase matched second harmonic can be achieved with appropriate excitation size of primary GWs. The results obtained in this study provide physical insight and guidance for choosing GW mode and transmitting/receiving condition that benefits the measurability of QSP in composite plates.

CRediT authorship contribution statement

Chang Jiang: Methodology, Validation, Investigation, Data curation, Writing – original draft, Writing – review & editing. **Weibin Li:** Conceptualization, Validation, Investigation, Writing – original draft, Writing – review & editing, Supervision, Project administration, Funding acquisition. **Mingxi Deng:** Conceptualization, Investigation, Writing – review & editing, Project administration, Funding acquisition. **Ching-Tai Ng:** Data curation, Writing – original draft, Supervision.

Declaration of Competing Interest

The authors declare that they have no known competing financial interests or personal relationships that could have appeared to influence the work reported in this paper.

Acknowledgments

References

[1] M. Sarfraz, H. Hong, S. Kim, Recent developments in the manufacturing technologies of composite components and their cost-effectiveness in the automotive industry: a review study, Compos. Struct. 266 (2021), 113864, https://doi.org/10.1016/j.compstruct.2021.113864.
[2] D. Rajak, D. Pagar, P. Menezes, E. Linul. Fiber-reinforced polymer composites: manufacturing, properties, and applications. polymers. 11, 1667 (2019). 10.3390/polym11101667.
[3] S. Rokhlin, D. Chimenti, P. Nagy, Physical Ultrasonics of Composites, Oxford University Press, New York, 2011.
[4] J. Krautkramer, H. Krautkramer, Ultrasonic Testing of Materials, Springer, Berlin, Heidelberg, 2013, https://doi.org/10.1007/978-3-662-10680-8.
[5] M.R. Kessler, Advanced Topics in Characterization of Composites, Trafford publishing, Victoria, BC, Canada, 2004.
[6] V. Chillara, C. Lissenden, Review of nonlinear ultrasonic guided wave nondestructive evaluation: theory, numerics, and experiments, Opt. Eng. 55 (2016), 011002, https://doi.org/10.1117/1.OE.55.1.011002.
[7] W. Li, M. Deng, Y. Xiang, Review on second-harmonic generation of ultrasonic guided waves in solid media (I): theoretical analyses, Chin. Phys. B 26 (2017), 114302, https://doi.org/10.1088/1674-1056/26/11/114302.
[8] M. Hasanian, C. Lissenden, Second order harmonic guided wave mutual interactions in plate: vector analysis, numerical simulation, and experimental results, J. Appl. Phys. 122 (2017), 084901, https://doi.org/10.1063/1.4993924.
[9] M. Deng, Analysis of second-harmonic generation of Lamb modes using a modal analysis approach, J. Appl. Phys. 94 (2003) 4152, https://doi.org/10.1063/1.1601312.
[10] W.J.N. de Lima, M.F. Hamilton, Finite-amplitude waves in isotropic elastic plates, J. Sound Vib. 265 (2003) 819–839, https://doi.org/10.1016/S0022-460X(02)01260-9.
[11] W. Li, M. Deng, N. Hu, Y. Xiang, Theoretical analysis and experimental observation of frequency mixing response of ultrasonic Lamb waves, J. Appl. Phys. 124 (2018), 044901, https://doi.org/10.1063/1.5028536.
[12] W. Li, Z. Lan, N. Hu, M. Deng, Modelling and simulation of backward combined harmonic generation induced by one-way mixing of longitudinal ultrasonic guided waves in a circular pipe, Ultrasonics 113 (2021), 106356, https://doi.org/10.1016/j.ultras.2021.106356.
[13] S. Shan, L. Cheng, Mixed third harmonic shear horizontal wave generation: interaction between primary shear horizontal wave and second harmonic Lamb wave, Smart Mater. Struct. 28 (2019), 085042, https://doi.org/10.1088/1361-665X/ab1fce.
[14] M. Sun, Y. Xiang, M. Deng, J. Xu, F. Xuan, Scanning non-collinear wave mixing for nonlinear ultrasonic detection and localization of plasticity, NDT E Int. 93 (2018) 1–6, https://doi.org/10.1016/j.ndteint.2017.09.010.
[15] R.N. Thurstion, M.J. Shapiro, Interpretation of ultrasonic experiments on finite-amplitude waves, J. Acoust. Soc. Am. 41 (1967) 1112, https://doi.org/10.1121/1.1910443.
[16] J.H. Cantrell, Acoustic-radiation stress in solids. I, Theory. Phys. Rev. B 30 (1984) 3214–3220, https://doi.org/10.1103/PhysRevB.30.3214.
[17] J.H. Cantrell, Effects of diffraction and dispersion on acoustic radiation-induced static pulses, Appl. Phys. Lett. 92 (2008), 231914, https://doi.org/10.1063/1.2937474.
[18] J.H. Cantrell, W.T. Yost, Shape profile of acoustic radiation-induced static displacement pulses in solids, J. Appl. Phys. 108 (2010), 013512, https://doi.org/10.1063/1.3457850.
[19] J.H. Cantrell, W.T. Yost, Energy conservation and pulse propagation in an elastic medium with quadratic nonlinearity, J. Appl. Phys. 112 (2012), 053507, https://doi.org/10.1063/1.4748963.
[20] J.M. Qu, L.J. Jacobs, P.B. Nagy, On the acoustic-radiation-induced strain and stress in elastic solids with quadratic nonlinearity (L), J. Acoust. Soc. Am. 129 (2011) 3449, https://doi.org/10.1121/1.3583501.
[21] P.B. Nagy, J.M. Qu, L.J. Jacobs, Finite-size effects on the quasistatic displacement pulse in a solid specimen with quadratic nonlinearity, J. Acoust. Soc. Am. 134 (2013) 1760–1774, https://doi.org/10.1121/1.4817840.
[22] J.M. Qu, P.B. Nagy, L.J. Jacobs, Pulse propagation in an elastic medium with quadratic nonlinearity (L), J. Acoust. Soc. Am. 131 (2012) 1827, https://doi.org/10.1121/1.3681922.
[23] X. Jacob, R. Takatsu, C. Barrière, D. Royer, Experimental study of the acoustic radiation strain in solids, Appl. Phys. Lett. 88 (2006), 134111, https://doi.org/10.1063/1.2191428.
[24] K.T. Narasimha, E. Kannan, K. Balasubramaniam, Simplified experimental technique to extract the acoustic radiation, Appl. Phys. Lett. 91 (2007), 134103, https://doi.org/10.1063/1.2793181.
[25] M. Deng, An experimental approach for detection of the acoustic radiation induced static component in solids, Chin. Phys. Lett. 37 (2020), 074301, https://doi.org/10.1088/0256-307X/37/7/074301.

[26] X. Wan, P. Tse, X. Zhang, G. Xu, Q. Zhang, et al., Numerical study on static component generation from the primary Lamb waves propagating in a plate with nonlinearity, Smart. Mater. Struct. 27 (2018), 045006, https://doi.org/10.1088/1361-665X/aaafeb.

[27] X. Sun, G. Shui, Y. Zhao, W. Liu, N. Hu, et al., Evaluation of early-stage local plastic damage induced by bending using quasi-static component of Lamb waves, NDT E Int. 116 (2020), 102332, https://doi.org/10.1016/j.ndteint.2020.102332.

[28] C. Jiang, W. Li, M. Deng, C. Ng, Static component generation and measurement of nonlinear guided waves with group velocity mismatch, JASA Express Lett. 1 (2021), 055601, https://doi.org/10.1121/10.0004847.

[29] J. Zhao, V.K. Chillara, B. Ren, H. Cho, J. Qiu, et al., Second harmonic generation in composites: theoretical and numerical analyses, J. Appl. Phys. 119 (2016), 064902, https://doi.org/10.1063/1.4941390.

[30] H. Chen, M. Deng, G. Gao, N. Hu, Y. Xiang, Modelling and simulation of static component generation of Lamb wave propagation in a layered plate, Ultrasonics 116 (2021), 106473, https://doi.org/10.1016/j.ultras.2021.106473.

[31] W. Li, S. Hu, M. Deng, Combination of phase matching and phase-reversal approaches for thermal damage assessment by second harmonic lamb waves, Materials 11 (2018) 1961, https://doi.org/10.3390/ma11101961 (Basel).

Chapter 5: Assessment of Damage in Composites Using Static Component Generation of Ultrasonic Guided Waves

5.1. Introduction, Significance, and Commentary

This chapter presents the study of QSC generation in composite thin plates with finite sizes. As indicated by previous studies, the generated QSC pulse signal has a near zero-frequency carrier wave and can suffer little acoustic attenuation in materials. However, the divergence loss of the nonlinear QSC wave is not neglectable, as the directivity of QSC wave is poorer than higher harmonic waves. By numerical simulation, the QSC wave by finite-size excitation of primary Lamb waves is investigated. The observed features of QSC in simulations are then compared with the results of following experiments. The study validates the measurability of QSC by transducers and the feasibility of microdamage detection and evaluation in composite thin plates, showing promising potential for NDT applications of other anisotropic materials.

5.2. Publication

This section is presented as published research paper by **Chang Jiang**, Changyu Zhang, Weibin Li, Mingxi Deng, and Ching-Tai Ng (2022) Assessment of damage in composites using static component generation of ultrasonic guided wave, *Smart Materials and Structures* 31(4):045025.

Statement of Authorship

Title of Paper	Assessment of damage in composites using static component generation of ultrasonic guided wave
Publication Status	☑ Published ☐ Accepted for Publication ☐ Submitted for Publication ☐ Unpublished and Unsubmitted work written in manuscript style
Publication Details	Chang Jiang, Changyu Zhang, Weibin Li, et al. (2022) Assessment of damage in composites using static component generation of ultrasonic guided wave, Smart Materials and Structures 31(4):045025.

Principal Author

Name of Principal Author (Candidate)	Chang Jiang		
Contribution to the Paper	Methodology, Investigation, Data curation, Visualization, Writing - Original Draft		
Overall percentage (%)	80		
Certification:	This paper reports on original research I conducted during the period of my Higher Degree by Research candidature and is not subject to any obligations or contractual agreements with a third party that would constrain its inclusion in this thesis. I am the primary author of this paper.		
Signature		Date	2023.12.29

Co-Author Contributions

By signing the Statement of Authorship, each author certifies that:

i. the candidate's stated contribution to the publication is accurate (as detailed above);

ii. permission is granted for the candidate in include the publication in the thesis; and

iii. the sum of all co-author contributions is equal to 100% less the candidate's stated contribution.

Name of Co-Author	Changyu Zhang		
Contribution to the Paper	Data curation, Writing - Review & Editing		
Signature		Date	2023.12.29
Name of Co-Author	Weibin Li		
Contribution to the Paper	Conceptualization, Resources, Writing - Review & Editing, Supervision, Funding acquisition		
Signature		Date	2023.12.29
Name of Co-Author	Mingxi Deng		
Contribution to the Paper	Resources, Writing - Review & Editing, Supervision		
Signature		Date	2023.12.29
Name of Co-Author	Ching-Tai Ng		
Contribution to the Paper	Writing - Review & Editing, Supervision		
Signature		Date	2023.12.29

Please cut and paste additional co-author panels here as required.

Assessment of damage in composites using static component generation of ultrasonic guided waves

Chang Jiang[1,3], Changyu Zhang[1], Weibin Li[1,*] , Mingxi Deng[2,*] and Ching-Tai Ng[3]

[1] School of Aerospace Engineering, Xiamen University, Xiamen, Fujian, People's Republic of China
[2] College of Aerospace Engineering, Chongqing University, Chongqing, People's Republic of China
[3] School of Civil, Environmental, and Mining Engineering, University of Adelaide, Adelaide, South Australia, Australia

E-mail: liweibin@xmu.edu.cn and dengmx65@yahoo.com

Abstract

Static component (SC) generation of guided waves (GWs), which combines the high sensitivity of acoustic nonlinearity to micro-damage and low attenuative effect, has great potential for damage assessment in large composite structures. The present work explores the use of SC generation of GWs for assessing damages in carbon fiber reinforced polymer (CFRP) composite laminates. The features including mode, waveform, and cumulative effect of the generated SC in composites are numerically investigated by three-dimensional finite element modeling and simulation. A dynamic displacement measurement method based on piezoelectric transducers is accordingly proposed and experimentally verified. The cumulative SC pulse generated from primary GW tone-burst with a finite duration, is observed and verified numerically and experimentally. It is found that the magnitude of the generated SC pulse is linearly proportional to the quadratic material nonlinearity. Experimental results demonstrate that the generated SC pulse of GW under group velocity matching condition, is an effective means to assess the hygrothermal damage and low-velocity impact damage in CFRP composite plates. The performed experimental examination validates the feasibility of the proposed approach for damage assessment in CFRP composites.

Keywords: guided wave, static component, material nonlinearity, composites, damage assessment

(Some figures may appear in colour only in the online journal)

1. Introduction

Fiber reinforced composite materials and structures are being widely applied in many fields due to the improved properties such as light weight, high strength and modulus, and corrosion resistance in comparison with metallic materials [1, 2]. However, the damage mechanism and failure analysis of fiber reinforced composites are generally complex.

High/low velocity impact, thermal/mechanical fatigue, and hygrothermal aging, are several main damage inducing factors for composite laminates [3, 4]. Damage evolution and accumulation from matrix microcracking and degradation to fiber breakage and delamination, can lead to severe reductions in strength and integrity of the composites, and eventually result in catastrophic failure of materials and structures in unpredictable manners [5, 6]. For major equipment and key facilities in civil, aerospace, national defense, and other industries, it is imperative to develop nondestructive testing and evaluation (NDT&E) methods for monitoring and evaluating structural

1

micro-changes of the composites at the early stage of damage evolution.

There has been increasing interest in studying the cost effective and time efficient techniques for NDT&E of composites based on the ultrasonic waves. In particular, the characterization of composites using ultrasonic guided waves (GWs) has gained significant attention in the past decades [7, 8]. The use of GWs has proven to be an effective and efficient means for inspecting composite laminates [9]. The measure of amplitude of the scattered GW signals, as well as the GW velocity, can usually provide indices of the macro-damages in the composites. On the other hand, the detection of micro-damages and degradation in composites using nonlinear ultrasonic GW has been reported in recent years. Nonlinear ultrasonic techniques take advantage of the nonlinear effects produced from the interaction between finite amplitude waves and the small-scale defects in materials [10]. In contrast to conventional linear ultrasonic testing approaches, these nonlinear GW techniques provide higher sensitivity to defects of smaller size than the wavelength of the fundamental GW. Second harmonic generation of propagating GWs due to the classical nonlinearity and contact acoustic nonlinearity in materials was reported and used for damage detection in composites [11, 12]. However, most previous investigations focused on the higher harmonic generation of primary GWs propagation in the damaged specimens. The strong anisotropy and high attenuation in fiber reinforced layered composites significantly reduce the magnitude of the generated higher harmonics of primary GW propagation and meanwhile make the corresponding wave propagation become complicated. It is quite challenging to assess the damage in highly attenuative composites by the measure of second harmonics with a double fundamental frequency of the primary GWs. In addition, it is difficult to isolate the material nonlinearity from the instrument induced nonlinearity by the measure of second harmonics generated. The GW mixing technique has shown the potential to locate micro-defects such as degradation in plate and pipe-like structures with the instrumental nonlinearity eliminated [13–15]. However, for materials with classical nonlinearity that arises from the nonlinear strain energy term, the synchronism and non-zero power flux conditions of GW mode pairs are required for generating cumulative mixed-frequency harmonics [15, 16]. This greatly limits the choice of the GW mode pairs. Sub-harmonic [17, 18] and nonlinear resonance [19, 20] are other known nonlinear acoustic phenomena. Nevertheless, the generation of sub-harmonic only results from micro-damages of specific size and form, and the nonlinear resonance methods generally relates to the point-to-point inspection using bulk waves.

When ultrasonic wave propagates through an elastic solid with material nonlinearity, acoustic radiation induced static displacement component will be generated [21–24]. Similar as higher harmonics, such acoustic radiation induced static component (SC) is related directly to the material nonlinearity. As one of the acoustic nonlinear responses of ultrasonic waves propagation in solid media, the SC generation of GWs was reported in recently years, which can promisingly be exploited for NDT&E of fiber reinforced composites circumventing the aforementioned limitations. Wan *et al* and Sun *et al* found

that the acoustic radiation induced SC is physically a secondary wave whose carrier frequency is zero, of which the cumulative effect does not require the phase-matching condition [25, 26]. Jiang *et al* further found that the synchronism condition as is necessary for generating the cumulative secondary GWs is intrinsically satisfied for the SC generated from any propagating GW mode at any frequency in isotropic plates [27]. Regarding damage inspection, Sun *et al* numerically investigated the SC of longitudinal wave induced by micro-cracks using a bilinear stiffness model [26]. Experimental studies were conducted on the detection of early plastic damage and partially closed crack in aluminum plate using the SC generation of Lamb waves [28, 29]. However, previous numerical studies have mostly focused on the SC generation under plane strain condition using two-dimensional models. The duration and shape of the primary GW tone-burst in practical application is expected to influence the temporal waveform of the generated SC pulse. Besides, insufficient attention has been paid to the SC generation in composites and the related damage detection. Due to the rather high attenuation in composites, the feasibility of using SC generation of high-frequency GWs for NDT&E of composites has yet to be verified.

The present study aims to investigate the SC generation of GWs in carbon fiber reinforced polymer (CFRP) composite laminates, as well as to propose a dynamic detection method for damage assessment in composite plates employing the SC generation. Features of the SC pulse generated by GW toneburst with a finite duration are numerically investigated using a three-dimensional model. The dynamic detection method and the phase reversal method are used for experimental verification of the cumulative SC pulse generated by high-frequency GW mode pair under group velocity matching condition. Feasibility study of damage assessments in composites using the proposed method is accordingly carried out. The rest of this paper is organized as follows: section 2 introduces the theoretical considerations on the SC generation of GW propagating in anisotropic materials. Section 3 presents the implementation of three-dimensional finite element (FE) modeling and simulation of the generated SC pulse in the CFRP composite layered plate. Experimental studies are presented in section 4, wherein hygrothermal damage and low-velocity impact damage are successively considered for damage assessment in CFRP composites using the generated SC pulse of high-frequency GW. The effectiveness of the proposed method is analyzed and discussed, and then the paper ends with a conclusion.

2. Theoretical considerations

2.1. SC generation of guided waves in composites

First, we consider the GW propagation in a single anisotropic plate with weak quadratic nonlinearity. Figure 1 shows the coordinate system $x_1 x_2 x_3$ established for the plate model, as well as the material coordinate system $x_1''' x_2''' x_3'''$ under which the second- and third-order elastic constants (C_{ijkl} and C_{ijklmn}) of the anisotropic material are defined.
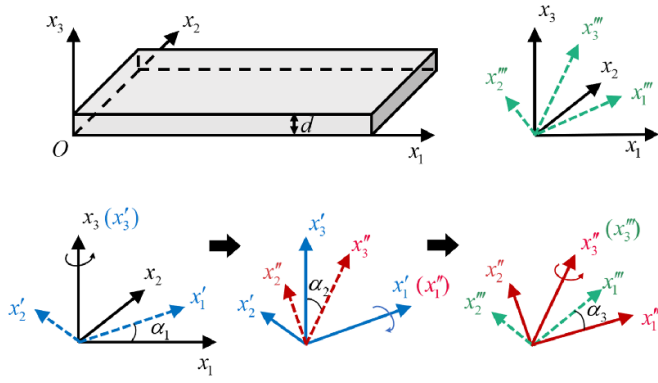
Figure 1. The anisotropic plate and the coordinate systems.

The orientation angles between the two coordinate systems are denoted as α_1, α_2 and α_3. For a GW propagating along the Ox_1 axis, its formal solution can be expressed as $u_i \exp[\mathrm{j}(kx_1 + akx_3 - \omega t)]$ $(i = 1, 2, 3)$. The six roots of a (denoted by $a^{(s)}$, $s = 1, \ldots, 6$) can be obtained from the Christoffel equation for plane wave propagation in anisotropic solids [30]. For each $a^{(s)}$, the corresponding eigen solution $\left(u_1^{(s)}, u_2^{(s)}, u_3^{(s)}\right)$ can also be determined. Further, the general solution of wave motion in terms of a linear combination of the six eigen solution is expressed as

$$U_i = \sum_{s=1}^{6} A_s u_i^{(s)} \exp\left[\mathrm{j}\left(kx_1 + a^{(s)} kx_3 - \omega t\right)\right], i = 1, 2, 3, \quad (1)$$

where U_i $(i = 1, 2, 3)$ is the displacement component along the Ox_1, Ox_2 and Ox_3 axis, respectively, and A_s $(s = 1, \ldots, 6)$ are the arbitrary constants to be determined. Assuming the GW propagation is present, A_s/A_1 can be determined by substituting the driving frequency ω and the corresponding phase velocity into the equations of the mechanical boundary conditions that requires the stress components of U_i to be zero at $x_3 = 0$ and $x_3 = d$. Due to the elastic anisotropy of the plate, the Lamb wave and shear horizontal GW modes are generally coupled.

Considering two primary GWs $U_i^{(a)}$ and $U_i^{(b)}$ excited simultaneously at $x_1 = 0$ and the stress-free boundary condition, the secondary wave field focusing on the cross-interaction of these two primary GWs can be obtained via the normal modal analysis [15, 16], expressed as

$$U_i^{(\omega_a \pm \omega_b)} = \sum_n a_n(x_1) U_{i(n)}^{(\omega_a \pm \omega_b)}(x_3) \exp\left[-\mathrm{j}(\omega_a \pm \omega_b) t\right]$$
$$+ c.c., (i = 1, 2, 3) \quad (2)$$

where $U_{i(n)}^{(\omega_a \pm \omega_b)}(x_3)$ is the field function of the nth GW at sum- or difference-frequency. The corresponding expansion coefficient $a_n(x_1)$ can formally be given by [30]

$$a_n(x_1) = \frac{\left(F_n^{\mathrm{V}} + F_n^{\mathrm{S}}\right)}{4P_{nn}} \frac{\sin\left[(k_a \pm k_b - k_n) x_1/2\right]}{(k_a \pm k_b - k_n)/2}, \quad (3)$$

where F_n^{V} and F_n^{S} are the power flux through the volume and the surfaces of the anisotropic solid plate, respectively, and P_{nn} is

the average power flux per unit width along the Ox_2 axis [15]. The synchronism condition ($k_{\pm} = k_a \pm k_b$ at $\omega_{\pm} = \omega_a \pm \omega_b$) and the non-power flux condition ($F_{\mathrm{V}} + F_{\mathrm{S}} \neq 0$) is necessary for the generation of the mixed-frequency harmonics with cumulative effect. In the specific case where two primary waves propagate in the same direction and satisfy the condition of $\omega_a \to \omega_b$ or $\omega_- \to 0$, the second order difference frequency component is of our interest. The equation (3) for difference frequency $\omega_- \to 0$ components can be expressed as

$$a_n(x_1) = \frac{\left(F_n^{\mathrm{V}} + F_n^{\mathrm{S}}\right)}{4P_{nn}} x_1. \quad (4)$$

The SC at zero frequency can be considered as the special case of difference frequency component ($\omega_- \to 0$), or the component due to the self-interaction of a monochromatic GW at frequency ω. Based on equation (4), it can be found that the synchronism condition is inherently satisfied for the SC generation of GWs.

For GWs propagation in CFRP, if the ultrasonic GWs propagate along the principal material direction of CFRP, the Lamb wave and shear horizontal GW modes can be decoupled. Only the *S*0 mode at zero frequency satisfies the non-zero power flux condition. Hence, the SC generated by GWs is the *S*0 mode at zero frequency. In the case of that GWs propagate along the non-principal material direction of CFRP, the displacement components cannot be decoupled with each other. It will generate multi-type modes at zero frequency (namely SCs). This is the unique feature of the SC generation of GWs in anisotropic composites such as CFRP [24]. Hence, for composite plates, the set of orientation angles (α_1, α_2, α_3) can be optimized for cumulatively generating the SC (the *S*0 mode at zero frequency), of which its magnitude is directly associated with the material nonlinearity.

Since ultrasonic GW tone-burst with a finite duration is excited in most experimental and practical cases, the tone-burst signals with different group velocities will separate from each other with the increase of GW propagation distance. The SC pulse generated by GW tone-burst can have a cumulative effect in amplitude with propagation distance only under the condition that its group velocity exactly or approximately equals that of primary GW [24, 25, 27]. Cumulative effect of SC generation is critical for the experiment and practical applications. Identification of this condition for mode selection is critical for the development of experimental testing and practical applications based on the SC generation of GWs.

2.2. Principle of dynamic measurement of SC pulse

It has been confirmed that, when the group velocity of a primary wave tone-burst matches with that of the generated SC pulse, the SC pulse will exhibit an envelope-like shape that has almost the same duration as the primary wave [24–27]. In general, the envelope shape of a primary wave is largely dependent on the modulation window applied to the RF tone-burst. Since the main lobe of the frequency spectrum of the Hanning window is wider than that of the rectangular window with the same
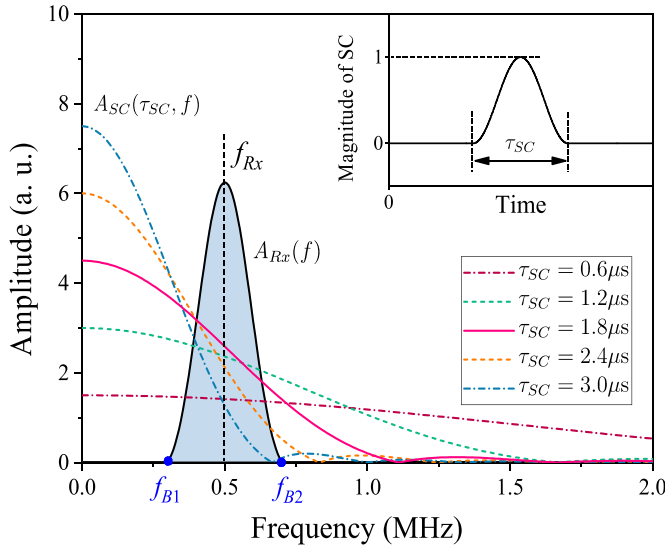
Figure 2. Amplitude-frequency curves of several Hanning window time-domain signals with different duration τ_{SC} and the same magnitude, as well as a schematic amplitude-frequency curve (black solid curve) of a low-frequency receiving transducer.

duration, and the former has a better side lobe suppression, the Hanning window is adopted to modulate the primary wave tone-burst in the proposed method. A low-frequency piezo-electric transducer can be used to directly detect the generated SC pulse that co-propagates with the primary wave. To that end, the main lobe frequency range of the low-frequency transducer is required to adequately overlap with that of the generated SC pulse. When the center frequencies of the transmitting (f_{Tx}) and the receiving (f_{Rx}) transducers are given, one can adjust the cycle number (n_H) of the relatively high-frequency RF tone-burst to achieve the dynamic detection of the SC pulse. Deng firstly proposed the method for detecting the SC pulse generated by longitudinal wave tone-burst [31]. This paper adapted the method for experimental observation of SC pulse generated by ultrasonic GWs in composites.

Figure 2 illustrates the amplitude-frequency response curves of several Hanning window time-domain signals with the same peaks but different durations. The Hanning window signal can well represent the generated SC pulse that co-propagates with the primary wave tone-burst. The corresponding frequency range of the SC pulse can be customized by adjusting its time-domain duration. Specifically, frequency range of the SC pulse will decrease with the increase of time duration (τ_{sc}) and vice versa. When the main lobe frequency range of the SC pulse is matched with that of a given receiving transducer (i.e. $\tau_H \approx 1/f_{Rx}$ or $n_H \approx f_H/f_{Rx}$), the SC pulse can be detected with the highest sensitivity by the low-frequency transducer [32]. Specifically, the spectrum response to the SC pulse using the low-frequency receiving transducer can be expressed as

$$\Gamma_{Rx}^{(SC)} = \int_{f_{B2}}^{f_{B1}} A_{SC}(\tau_{sc}, f) \cdot A_{Rx}(f) \, \mathrm{d}f, \qquad (5)$$

where the integration interval $[f_{B1}, f_{B2}]$ is the bandwidth of the amplitude-frequency curve $[A_{Rx}(f)]$ of the given low-frequency receiving transducer Rx, and $A_{SC}(\tau_{sc}, f)$ is the amplitude-frequency curve of the generated SC pulse. Since τ_H is equal to τ_{SC} when the SC pulse is generated under the group velocity matching condition, a maximized magnitude of response $\Gamma_{Rx}^{(SC)}$ can be obtained by optimizing the duration τ_H of the primary GW tone-burst.

3. Finite element modeling and simulation

3.1. Finite element model of composite laminate

To verify the proposed method, numerical studies are first conducted by employing a three-dimensional FE model as shown in figure 3. Here we consider a CFRP composite plate with a [0/90/0/90]s lay-up configuration. The thickness of the 8-layer composite laminate is $d = 1.36$ mm. The mass density is $1700 \text{ kg} \cdot \text{m}^{-3}$. To model GW propagation in this composite laminate with weak material nonlinearity, hyperelastic material model is adopted. In general, the strain energy function of an anisotropic plate incorporating the nonlinear elastic terms are expressed by

$$W_s = \frac{1}{2!} C_{ijkl} E_{ij} E_{kl} + \frac{1}{3} C_{ijklmn} E_{ij} E_{kl} E_{mn} + O(E^4), \qquad (6)$$

where C_{ijkl} and C_{ijklmn} are the second order elastic constants (SOECs) and third order elastic constants (TOECs), respectively. A single layer of the composite laminate can be considered as a transversely isotropic (TI) material. There are only five independent SOECs and nine independent TOECs [32, 33], which are shown in tables 1 and 2, respectively. For simplicity, the constants are represented using the Voigt notation. The mass density of the TI material is 1700 kg m^{-3}. By separately defining local material coordinate systems for each layer of the composite laminate and input these material properties, the wave propagation problem can be simulated and analyzed using a uniform (X, Y, Z) coordinate system wherein the wave propagation direction is chosen along the X direction (i.e. 0° direction of the material).

The model is discretized with quadratic solid elements, of which the maximum size is determined by $\Delta e = \lambda/20$, where λ is the wavelength of the primary wave. The width of the model in Y direction is chosen as Δe. To save computational resources and calculation time, and in the meanwhile ensure the numerical accuracy, the $S0$ mode at a relatively low frequency of $f_1 = 0.5$ MHz is chosen as the primary GW for the numerical verification. As shown in the dispersion curves of GWs propagation in this composite laminate, the phase velocity and group velocity of the $S0$ mode at 0.5 MHz propagating along 0° direction are 6040 m s^{-1} and 5800 m s^{-1}, respectively. The wavelength is $\lambda_1 = 12$ mm. As shown in figure 3, the displacement load of a Hanning windowed eight-cycle sine tone-burst with maximum amplitude of 100 nm is applied to a rectangular area ($W_{\text{exci}} = 30$ mm) of the front face, and the other end is a fixed support. The length of the plate is $L = 0.4$ m. The width of the plate is $W = 50$ mm. To reduce

Table 1. Second order elastic constants of the transversely isotropic material (unit: GPa).

C_{11}	C_{12}	C_{22}	C_{23}	C_{55}
119	6.2	13.8	4.5	5.7

Table 2. Third order elastic constants of the transversely isotropic material (unit: GPa).

C_{111}	C_{112}	C_{155}	C_{222}	C_{223}	C_{122}	C_{123}	C_{255}	C_{266}
1000	65	−47	−214	−89	−4	65	−33.4	−49.1
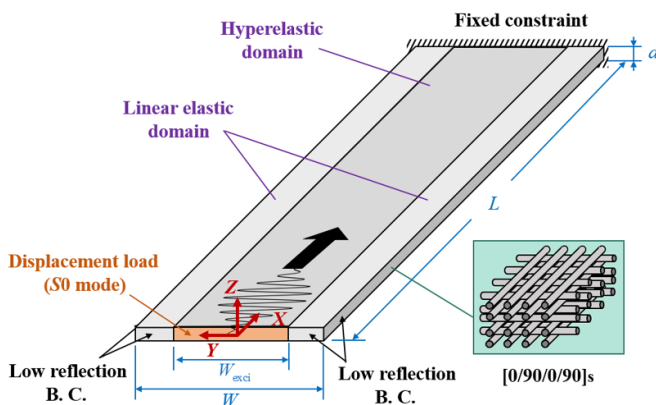
Figure 3. Finite element model of a [0/90/0/90]s composite plate.

the interference of boundary reflected waves, low reflection boundary conditions are assigned to the remaining lateral surfaces. Here, two linear elastic domains are defined at the left and right sides for addressing the incompatibility of the hyperelastic domain with the low reflection boundary conditions [34]. Domain point probes for receiving the GW signal are set at the center of the top surface of the plate. The displacement signals extracted in the *X, Y* and *Z* directions are represented by U_1, U_2 and U_3. Appropriate time step of the transient solver (Δt) and the maximum element size (I_{max}) are adopted following $\Delta t < 1/20f_1$ and $I_{max} < \lambda_1/20$.

3.2. Guided wave signal analysis

The mode of the primary GW at 0.5 MHz is verified first. By comparing the time-domain GW signals received at different locations, the group velocity of the primary wave is calculated to be 6000 m s^{-1}. Due to a small relative error (3.4%) of the group velocity comparing to the theoretical value ($c_g^{S0} = 5800$ m s^{-1}), it is convinced that the propagating primary GW is the expected *S*0 mode. The durations of these Hanning windowed eight-cycle tone-burst GW signals are $\tau_H = 16 \mu$s. Figure 4(a) shows the displacements of primary signal received at $X = 200$ mm in *X, Y* and *Z* directions (represented by U_1, U_2, U_3), respectively. For the observation of the generated SC pulse, the phase-reversal approach [35] is employed to counteract the primary wave, and a low-pass filter with the cutoff frequency of 500 kHz is used to eliminate the higher harmonic components generated. As shown in

figure 4(b), it only remains the components of SC pulse generated by the primary wave propagation in the composite plate. The generated SC pulse displays large in-plane displacement in the *X* direction (i.e. wave propagation direction). Besides, it is found that the SC pulse signal has a temporal waveform of about one-cycle envelope rather than half-cycle one as demonstrated previously for longitudinal wave propagation and GW propagation under plane strain condition using twodimensional models [25]. It should be noted that, in practical test, due to finite-size excitation in the relative large sample, the primary GW has a curved wavefront, and the generated SC pulse signal is supposed to be different from that generated in two-dimensional models.

Figure 5(a) shows the time-domain signals of the generated SC pulse received at different locations using the phase-reversal method. The group velocity of the SC pulse is calculated as around 6186 m s^{-1}. This confirms that the generated SC pulse has the nature of the *S*0 mode at zero frequency. It is found that the magnitude of the generated SC pulse has a cumulative effect versus propagation distance as shown in figure 5(a). This finding is consistent with the theoretical prediction.

Figure 5(b) shows the received time-domain signals of the SC pulse generated by primary GW tone-burst with different durations. When we change the duration of the excitation signal of primary GW tone-burst τ_H from 8 μs to 32 μs, the time-domain duration of the generated SC pulse τ_{SC} increases accordingly. This validates that the frequency range of the generated SC pulse can be adjusted to adequately overlap with that of the receiving transducer for a high efficiency of detection of the generated SC pulse.

It is known that, in the specimen with microdamage or degradation, the SOECs almost keep unchanged, while the TOECs can change significantly [36]. In this investigation, the accumulation of material degradation in the sample is represented by the scale coefficient η of TOECs constants. The amplitude of the SC pulse increases linearly with the scaling coefficient η, as shown in figures 6(a) and (b). Thus, it is further confirmed that the obtained SC pulse signal is linearly proportional to the material nonlinearity. Also, the proposed method for detecting the SC pulse generated by GW and material nonlinearity can be applied in early damage evaluation of composite materials.

4. Experimental investigation

4.1. Specimens

The CFRP composite laminates used in this study are commercially provided by Wuxi Zhishang New Material Technology Co., Ltd, China. The composite plates comprise T300 fibers and YZR-03 epoxy, of which the main properties are listed in tables 3 and 4, respectively. For a unidirectional CFRP plate, the elastic stiffness matrix components obtained by referencing the GB/T 1477 standard are shown in table 5. The purchased pristine composite laminates have a [0/90/0/90]s layup configuration with a thickness of 1.36 mm and a density of
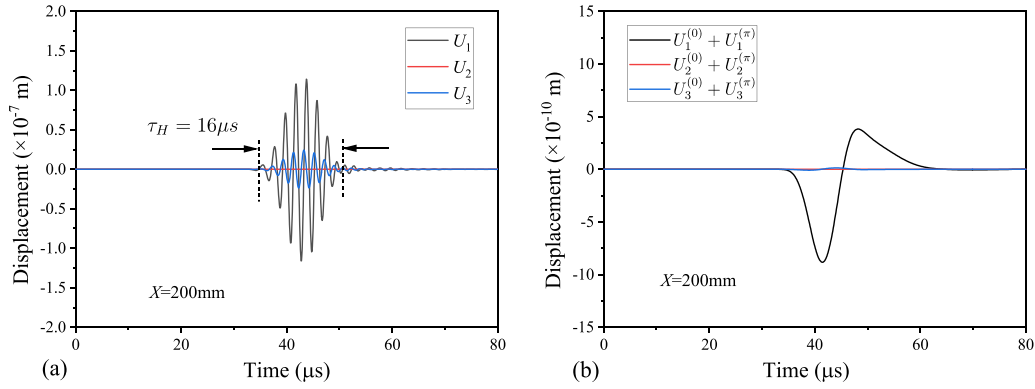
Figure 4. (a) Time-domain displacement signals received at $X = 200$ mm in different directions, and (b) SC pulse signals using phase-reversal method.
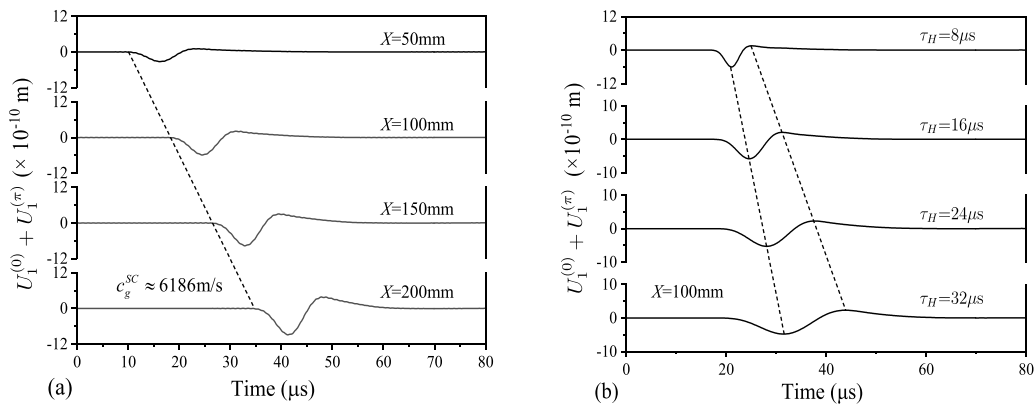

Figure 5. Time-domain signals of the SC pulse: (a) received at different locations, and (b) generated by primary GW tone-burst with different durations.
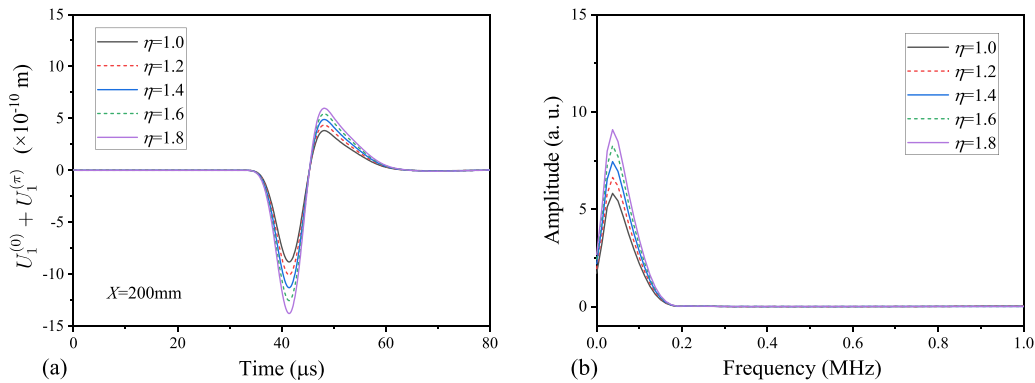

Figure 6. The SC pulse signals received in the given composite with different scaling coefficient η of the material nonlinearity using phase-reversal method: (a) the time-domain signals detected, and (b) the corresponding amplitude-frequency curves.

1700 kg·m^{-3}. Properties of the intact cross-ply laminate are listed in table 6.

In this study, two forms of damage of the composite are considered: (a) hygrothermal damage and (b) low-velocity impact damage. Figures 7(a) and (b) show the experimental setups, respectively. For artificial accelerated hygrothermal damage, two composite laminate specimens #A1 and #A2 with the dimension of 500 mm × 500 mm are in turn put into the water tank for different processing times, and then removed from the water and cool down to room temperature

for the following ultrasonic measurement. The water is heated through a cyclic heating process by a temperature-controlled heater with the water temperature ranges from 55 °C to 95 °C. After each measurement, the specimens are again put into the water for an increased cumulative processing time. For specimens #A1 and #A2, the cumulative processing times between each ultrasonic measurement are from 3 h to 24 h with intervals of 3 h. For low-velocity impact damage, composite specimens #B1, #B2, and #B3 with the dimension of 300 mm × 300 mm are impacted by an impact test machine using the free-fall

Table 3. Properties of the fiber T300.

Item	Specification	Test standard
Tensile modulus	240 GPa	ISO 10618
Tensile strength	4500 MPa	ISO 10618
Density	1790 kg m^{-3}	ISO 10119
Elongation	1.8%	ISO 10618

Table 4. Properties of the epoxy resin YZR-03.

Item	Specification	Test standard
Vitrification transition temperature	125 °C–135 °C	GB/T19466.2
Tensile strength	80 MPa	GB/T2567-2008
Bending strength	115 MPa	GB/T2567-2008
Bending modulus	4.28 GPa	GB/T2567-2008

Table 5. Stiffness matrix components of the unidirectional composite plate (unit: GPa).

C_{11}	C_{12}	C_{13}	C_{22}	C_{23}	C_{33}	C_{44}	C_{55}	C_{66}
119	6.2	6.2	13.8	4.5	13.8	4.65	5.7	5.7

Table 6. Properties of the laminate.

Ply thickness	Lay-up configuration	Density	Thickness
0.17 mm	[0/90/0/90]s	1700 kg·m^{-3}	1.36 mm

drop method conforming to the ASTM D7136 standard. Different impact energies of 4.0 J, 8.0 J and 12.0 J for these three specimens are calculated by the gravitational potential energy equation in terms of the weight and the elevation of the impacting head.

4.2. Ultrasonic measurements

To select the appropriate primary GW mode of which its group velocity matches with the generated SC pulse (whose carrier is the $S0$ mode at zero frequency), the phase and group velocity dispersion curves of the CFRP laminate are calculated using the stiffness matrix components shown in table 5. The $A9$ mode at frequency 9.5 MHz is selected as the primary Lamb wave mode. As presented in figure 8, The group velocity of the $A9$ mode is about 6025 m s^{-1}, which approximately matches with that of the $S0$ mode at zero frequency (6150 m s^{-1}). Under this group velocity matching condition, as is analyzed in sections 2 and 3, the magnitude of the generated SC pulse is linearly proportional to the material nonlinearity and the GW propagation distance. Consequently, the detection of the generated SC using the mode pair $A9$-$s0$ can be a feasible tool for damage assessment of composite plates.

Figure 9 shows the experimental setup of the ultrasonic measurements and the corresponding schematic diagram. The computer-controlled ultrasonic transmitter-receiver system (RITEC 5000 SNAP System) is used to generate RF tone-burst voltages for excitation of the high-frequency wedge

transducer *Tx*, and to receive and process the ultrasonic signals detected by the wedge transducer *Rx*. The digital oscilloscope (Model DPO3032, Tektronix Inc.) is used to record the measured ultrasonic signals. To suppress the transient behavior of the RF amplified voltages from the output of the SNAP system, a high-power load (Model RL-50) and a high-power adjustable attenuator (Model RA-31) is successively used. A high-pass filter (Model RHP-5) with the cutoff frequency of 5 MHz is used to ensure that there is no low-frequency signal applied on the wedge transducer *Tx*, of which the center frequency is around 10 MHz. The wedge transducers both consist of plexiglasses and longitudinal wave transducers. The effective area of the transducers is 13 mm $\times$ 25 mm. The oblique angle $\theta = 18.3°$ for the wedges of transmitting and receiving transducer is calculated according to the Snell's law $c_p^{(L-\text{Wedge})}/\sin\theta = c_p^{(A9-\text{CFRP})}/\sin 90°$, where the longitudinal wave velocity in the plexiglass is around $c_p^{(L-\text{Wedge})} = 2700\,\text{m s}^{-1}$ and the phase velocity of the primary $A9$ mode in the CFRP plate is around $c_p^{(A9-\text{CFRP})} = 8580\,\text{m s}^{-1}$. First, we examine the propagation of the expected $A9$ mode at the frequency $f_1 = 9.5\,\text{MHz}$ using a wedge transducer $Rx^{(H)}$ with a center frequency of 10 MHz. The detected GW signal of low voltage passes through a preamplifier toward the receiver of the SNAP System without using a low-pass filter. Subsequently, a wedge transducer $Rx^{(L)}$ with a relatively low center frequency of 0.5 MHz is used to replace the $Rx^{(H)}$ for directly detecting the SC pulse generated from the primary $A9$ mode. To ensure that the primary GW signal is not included in the received signal, a low-pass filter (Model RLP-3) with the cutoff frequency of around 3 MHz is applied on the detected signal of the wedge transducer $Rx^{(L)}$ before it passes into the preamplifier. For the ultrasonic measurements, the power level of the RF amplifier is 100, and the delay of the generated Hanning windowed tone-burst is $2\,\mu\text{s}$. The attenuation of the adjustable attenuator is 4 dB. The total receiving gain of the SNAP System is 70 dB. For the composite specimens, the same measurement is repeated three times. The results are presented and discussed in section 5.

5. Results and discussion

5.1. Validation of the dynamic measurement method

We first examine the propagation of the primary GW of the $A9$ mode at 9.5 MHz in the intact composite plate. Figure 10 shows the received signal of the wedge transducer $Rx^{(H)}$ with a center frequency of around 10 MHz. The spatial separation of the transmitter and the receiver is $L = 100$ mm. Due to the high frequency of the primary GW and the great material-related ultrasonic attenuation in the cross-ply CFRP laminate, the wedge transducer $Rx^{(H)}$ cannot detect the primary $A9$ mode with sufficient signal-to-noise ratio (SNR). On the other hand, the low-frequency wedge transducer $Rx^{(L)}$ with a center frequency of around 0.5 MHz can directly detect the SC pulse generated from the propagation of the primary GW tone-burst in combination with the use of the low-pass filter. Figure 11 shows the measured amplitude-frequency curve
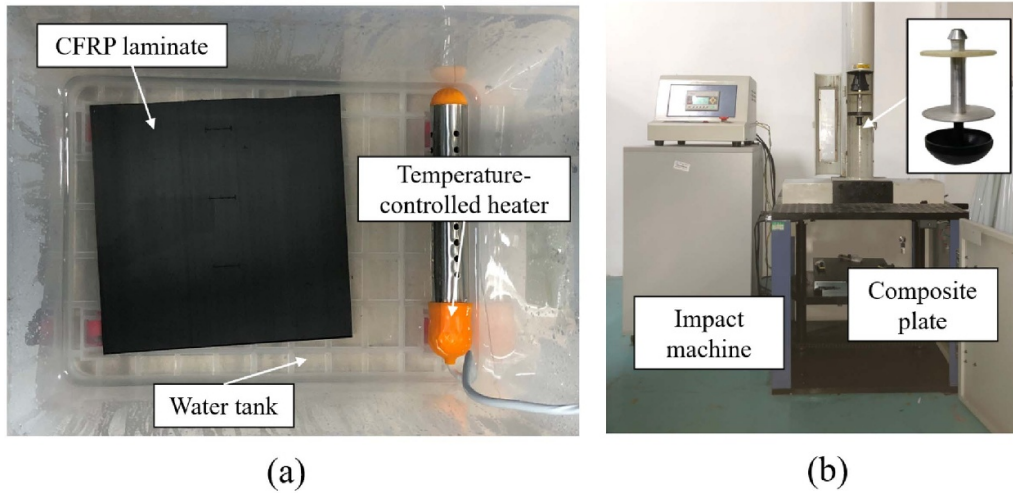
Figure 7. Experimental setups for introducing micro damages to the composite laminates: (a) hygrothermal damage, and (b) low-velocity impact damage.
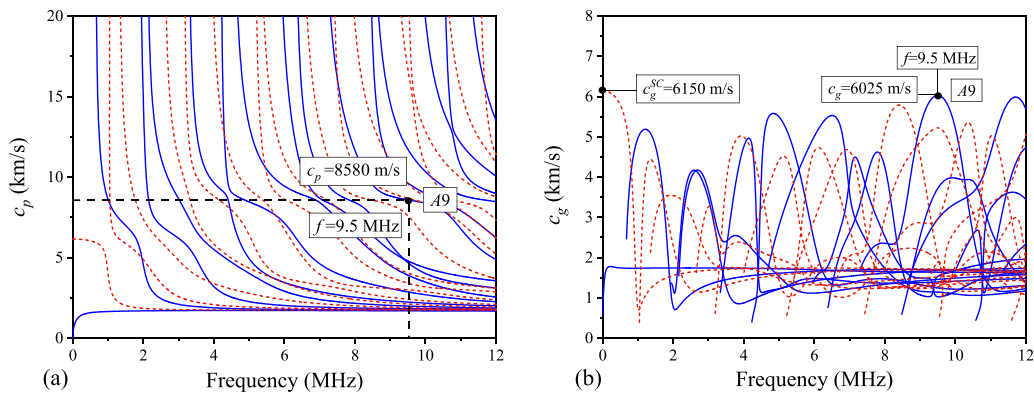

Figure 8. Dispersion curves of GWs propagating in the [0/90/0/90]s CFRP laminate along $0°$ direction: (a) phase and (b) group velocities.
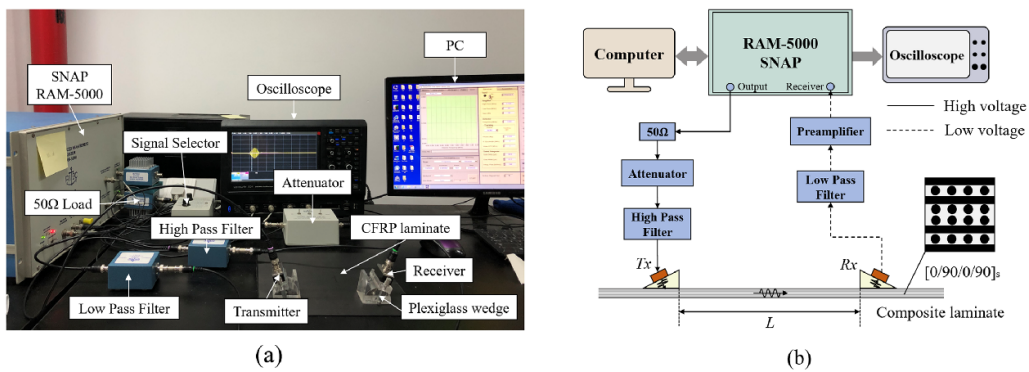

Figure 9. (a) Experimental setup of the ultrasonic measurement and (b) the corresponding schematic diagram.

of the receiving transducer $Rx^{(L)}$ using the pulse-echo technique, through which it is found that the center frequency of the wedge transducer $Rx^{(L)}$ is 515 kHz.

Figure 12 shows the low-frequency signals detected by the low-frequency transducer $Rx^{(L)}$ in the pristine composite laminate. Here, the phase reversal method [35] is used to further confirm that the received low-frequency components are the nonlinear signals associated with the generated SC pulse

of the primary $A9$ mode. With the initial phase of the 6-cycle RF tone-burst voltages applied on the Tx reversed from $0°$ to $180°$, it is observed that the signals received by the low-frequency wedge transducer $Rx^{(L)}$ at $L = 100$ mm are identical. It can be concluded that the measured signals are the secondary nonlinear ones (namely the generated SC pulses). Otherwise, they should have a difference in phase. On the other hand, since the low-frequency components of the RF voltages
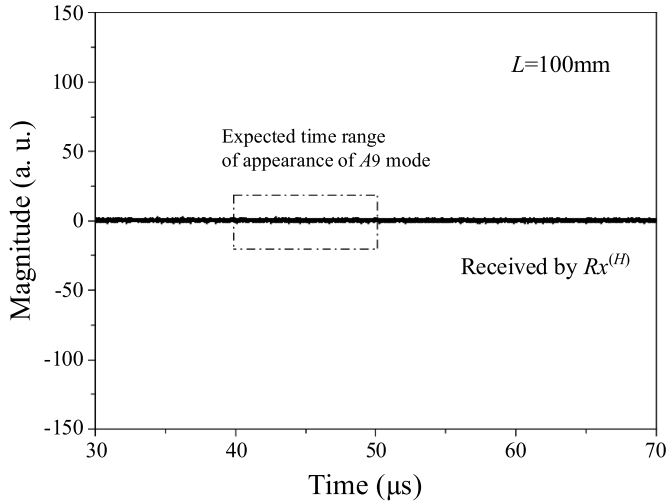
Figure 10. Time-domain signal received by the high-frequency wedge transducer $Rx^{(H)}$ with the spatial separation $L = 100$ mm.

Figure 12. Low-frequency signals received by the low-frequency wedge transducer $Rx^{(L)}$ with excitation signals of $0°$ and $180°$ phases.
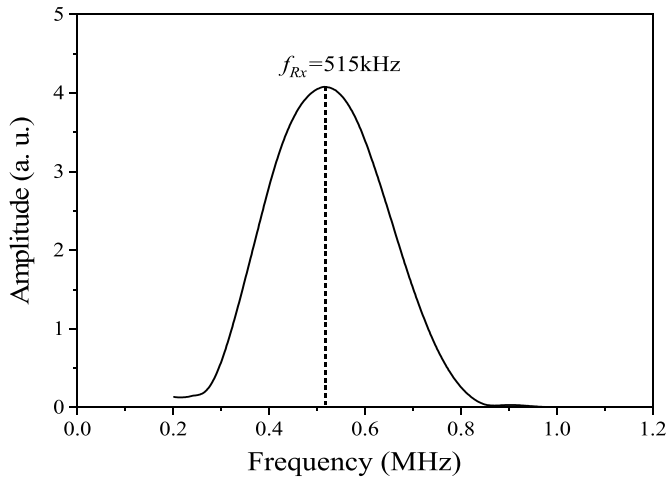

Figure 11. Amplitude-frequency curve of the receiving wedge transducer $Rx^{(L)}$.

in the transmitting terminal are eliminated by the high-pass filter (Model RHP-5) with the cutoff frequency of 5.0 MHz, it is convinced that the measured signals should be attributed to the SC (i.e. $S0$ mode at zero frequency) of the primary $A9$ mode. It should be noted that the measured signals of the SC pulse in experiment (shown in figure 12), are different from those obtained by numerical simulation (shown in figure 6). The reason of this difference is attributed to the fact that the experimental SC pulse measured by the receiving wedge transducer $Rx^{(L)}$ is formally determined by the convolution integral operation of impulse response function of $Rx^{(L)}$ and the generated SC pulse. Moreover, it needs to be pointed out that figures 10 and 12 have the same setup of signal amplification gain.

Figure 13(a) shows the low-frequency signals detected by the wedge transducer $Rx^{(L)}$ with different spatial separations of the transmitting transducer Tx and the receiving transducer $Rx^{(L)}$. Based on the corresponding delay of the propagating wave package, the group velocity of the received low-frequency GW signal is calculated to be around 6094 m s^{-1},
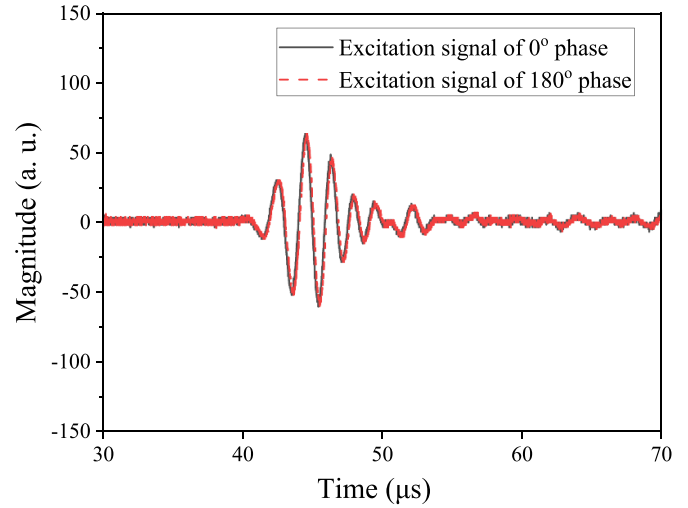
which is very close to the theoretical group velocity of the $S0$ mode at zero frequency as shown in figure 8(b). The relative error of the group velocity between the zero-frequency $S0$ mode and the received low-frequency signal is about 0.9%. Thus, we infer that the carrier of the detected ultrasonic time-domain signal, is the generated SC (i.e. zero-frequency $S0$ mode) of the primary $A9$ mode. Figure 13(b) shows the peak-to-peak voltages of the low-frequency signals received at different locations. In comparison with the primary $A9$ mode that is remarkably attenuated within a short propagation distance in the composite plate, this low-frequency signal can promisingly propagate a relatively long distance in the composite laminate with satisfactory SNR.

To verify the proposed dynamic detection method described in section 2.2, the duration of the RF tone-burst applied on the transmitting transducer is adjusted from $0.5\,\mu$s to $4.0\,\mu$s. Figure 14(a) shows the detected low-frequency signals in the time domain. Figure 14(b) shows the peak-to-peak voltages of the low-frequency signals received by the wedge transducer $Rx^{(L)}$. First, it is observed from figure 14(a) that the received low-frequency signal has a maximum magnitude when the duration of the transmitting RF tone-burst reaches to $\tau_H = 1/f_{Rx} = 2\,\mu$s. As the duration of the RF tone-burst continues to increase from $2\,\mu$s to $4\,\mu$s, the magnitude of the received low-frequency signal decreases. This phenomenon is in good agreement with the theoretical analysis and the numerical analysis as demonstrated in sections 2.2 and 3.2, respectively. When the wedge transducer Tx is driven by the amplified high-frequency (9.5 MHz) RF tone-burst, the primary GW tone-burst (the $A9$ mode) is excited into the composite laminate, and the SC pulse is generated and propagates with the primary $A9$ mode with approximately the same group velocity. When increasing the duration τ_H of the primary wave, the duration of the generated SC τ_{SC} increases correspondingly, and the magnitude of response $\Gamma_{Rx}^{(SC)}$ of the receiving transducer $Rx^{(L)}$ first increases and then decreases.
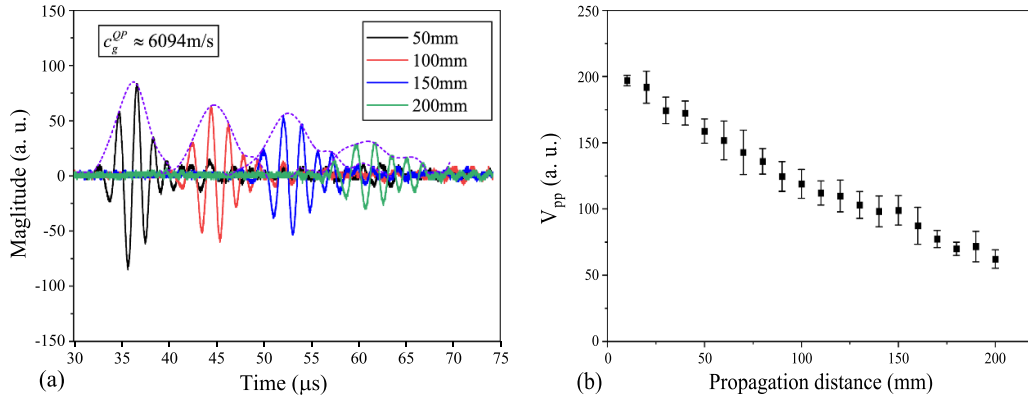
Figure 13. Low-frequency signals received by the low-frequency wedge transducer $Rx^{(L)}$ at different locations: (a) time-domain signals and (b) peak-to-peak voltages.
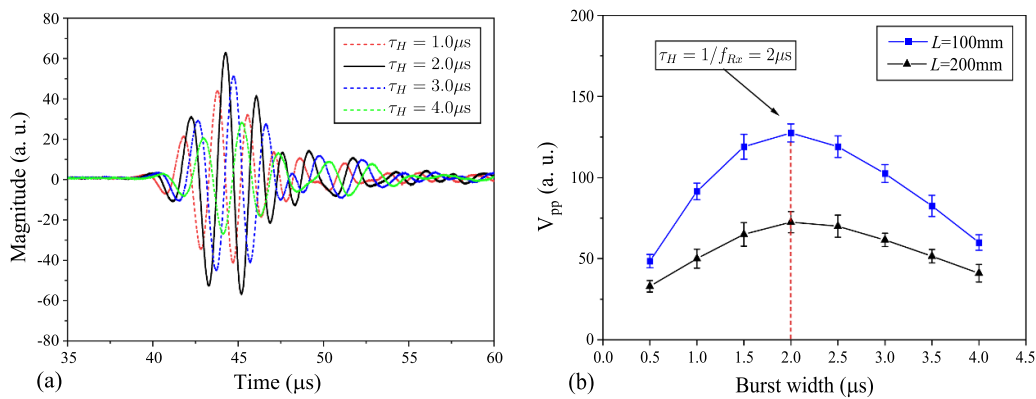

Figure 14. (a) The generated SC pulses of primary $A9$ modes with different tone-burst durations, and (b) the corresponding peak-to-peak voltages.

5.2. Damage assessment

For the composite specimens #A1 and #A2, the evaluation of the artificially introduced hygrothermal damage is conducted using the proposed method. The distance between the transmitting wedge transducer *Tx* and the low frequency receiving wedge transducer $Rx^{(L)}$ is chosen as $L = 100$ mm. First, the tone-burst width of the excitation signal is chosen as $\tau_{\mathrm{H}} = 2\,\mu\mathrm{s}$. Since the center frequency of the receiving transducer is around 0.5 MHz, the low-frequency signal associated with the SC generation is supposed to be detected with the optimized SNR. After three times of measurements, the burst width of the excitation signal is adjusted to $\tau_{\mathrm{H}} = 3\,\mu\mathrm{s}$ for the similar repeated measurements. Figure 15(a) shows the measured peak-to-peak voltages of the received low-frequency signals with respect to the processing time of hygrothermal damage. For both the composite specimens #A1 and #A2, it is observed that the measured amplitudes of the detected low-frequency signals increase notably from around 120 mV to around 180 mV with the cumulative processing time increases to around 12 h. After that, the measured peak-peak voltages of the received low-frequency signals maintains a relatively steady level. Besides, the measured amplitudes of the received signals concerning the different burst widths of the excitation signals have almost the same trends with respect to the

processing time except for a different SNR. This result supports the proposed dynamic detection method that the low-frequency wedge transducer can directly detect the generate SC pulse when the main lobe of the SC pulse adequately overlaps with that of the impulse response of *Rx* in the frequency domain.

Moreover, we define the time-domain SC pulse and the impulse response function of the receiving transducer $Rx^{(L)}$ as $h(t)$ and $r(t)$, respectively. The corresponding time-domain signal received by the transducer $Rx^{(L)}$ is formally given by $R(t) = h(t) * r(t)$, where the sign $*$ means the convolution operation [36]. As the envelop of the detected low-frequency signal can represent the generated SC pulse, the integration amplitude $\bar{A}^{(\mathrm{SC})}$ of the upper envelop of the received signal $R(t)$ is used to quantify the efficiency of the SC pulse generated by the primary $A9$ mode. The integration interval is chosen as $30\,\mu\mathrm{s}$ to completely capture the generated SC pulse. Figure 15(b) shows the measured integration amplitudes $\bar{A}^{(\mathrm{SC})}$ in the composite specimens #A1 and #A2. Normalization was performed with respect to the minimum value of the composite laminate #A1 in pristine status to display only the relative change. The results are consistent with that of the measured peak-to-peak voltage as shown in figure 15(a). The efficiency of the SC generation is directly proportional to the material nonlinearity. Due to the group velocity matching condition
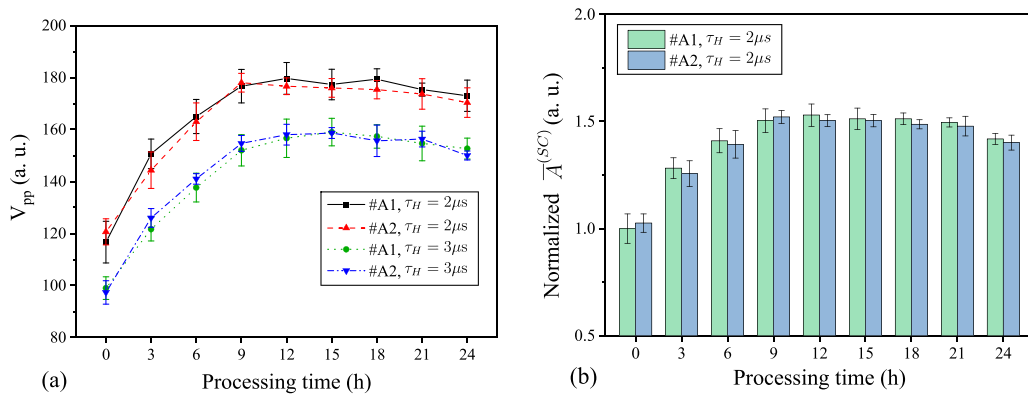
Figure 15. (a) The peak-to-peak voltages and (b) integration amplitudes $\bar{A}^{(SC)}$ of the low-frequency signals obtained in measurement of specimens #A1 and #A2. The spatial separation of the transmitting transducer Tx and the receiving transducer $Rx^{(L)}$ is $L = 100$ mm.
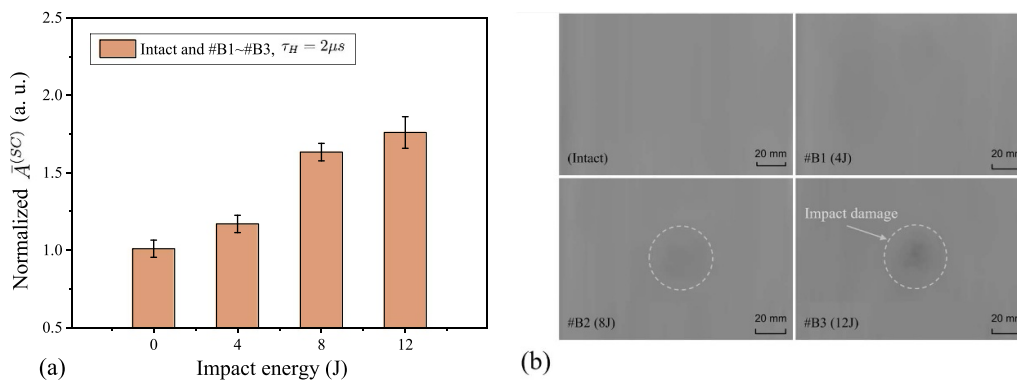

Figure 16. (a) Normalized integrated amplitude of the SC pulses measured on the low-velocity impacted composite specimens, and (b) observation of impact induced internal damage by infrared thermography.

of the generated SC pulse and the primary $A9$ mode, both the time-domain peak and the integration amplitude of the received low-frequency signal can be used to evaluate the hygrothermal damage of the composite laminate. It is noted that the measured V_{pp} and the $\bar{A}^{(SC)}$ on the composite specimens with hygrothermal processing time greater than 12 h stop increasing and tend to decrease after being processed more than 18 h. This can be attributed to the mutual restriction of various material internal factors when the composite laminates are subjected to the artificial accelerated hygrothermal loading. The exposure to the moist environment with an elevated temperature leads to the physicochemical changes of the composites. The polymer matrix is prone to suffer from stress corrosion after the moisture penetrates through the whole laminate [37–40]. Furthermore, plasticization, oxidation, hydrolysis, residual cross-linking, and chain scission, are the primary effects of chemical degradation of the polymer [6, 37, 41, 42]. The moisture absorption combined with the cyclic thermal loading can weaken the fiber/matrix interface, reduce the interlaminar strength, and enhance the material nonlinearity to a certain degree. As a result, the proposed method based on the SC generation of ultrasonic GW can be applied on the assessment of the hygrothermal damage in composite laminates.

For the low-velocity impacted composite specimens, figure 16(a) shows the variations of the integration amplitude $\bar{A}^{(SC)}$ of the SC pulse measured by the low-frequency wedge transducer $Rx^{(L)}$ in four specimens under different impact loadings. The spatial separation of the transmitting transducer Tx and the receiving transducer $Rx^{(L)}$ is $L = 100$ mm. It is observed that the value of the integration amplitude $\bar{A}^{(SC)}$ increases with the impact energy regarding the low-velocity impact testing of the composite specimens #B1, #B2 and #B3. In this study, all measured $\bar{A}^{(SC)}$ of the SC pulses are normalized by the values of the intact specimen to display only the relative change. Since the low-velocity and low-energy impact generally cannot introduce gross detects and serious damage in the composites, it is expected that invisible internal damages such as delamination, debonding, and fiber breakage are induced at the local impacted area. It is known that the contact acoustic nonlinearity by these complex microstructural interfaces in the impacted laminates can generally result in a stronger nonlinear response of ultrasonic GW propagation than the classical material nonlinearity [43, 44]. The existence

of these micro-damages can notably enhance the efficiency of the SC generation of the primary GW, and consequently raise the magnitude of the generated SC pulse signals. Figure 16(b) shows the infrared thermographic images for observing the impact induced internal damage of the composite specimens. The impact damage area of the composite specimen #B3 is approximately a circle with a diameter of 10 mm. However, as one of the conventional NDT methods for evaluating damages of materials, the infrared thermography can barely detect the low-velocity impact damage in composite laminates with a relatively high resolution. In contrast, the proposed method based on the SC generation of the high-frequency GWs can promisingly detect the low-velocity impact damage rendering a considerable sensitivity.

Due to the relatively low attenuation of the SC pulse (whose carrier wave frequency is zero) generated by GW tone-burst, the use of the SC generation has a greater potential for NDT&E of highly attenuative composite structures, than the use of the generation of second harmonics of primary GWs. In addition, experimental instruments including the piezoelectric transmitter cannot introduce the SC. Consequently, the SC generation based technique has an advantage to isolate the material nonlinearity from the instrument-induced one.

It also needs to be noted that the SC generation based technique is generally applicable to test over a region between the transmitter and receiver rather than a specific location, which is the same as the second harmonic generation based technique. However, similar as reported in [45] and [46] for imaging and locating the local damage by the second harmonic generation based technique, it is expected that damage localization can also be realized by the proposed approach. Especially, the generation of the SC is only attributed to the acoustic radiation induced static displacement components, which is helpful to quantify the degree of damage in high attenuative structures.

6. Conclusion

Assessment of damage in CFRP composite laminates using the SC generation of ultrasonic high-frequency GWs was investigated in this study. The SC generation in the composite plate was analyzed through FE simulations wherein a three-dimensional model was used. The proposed dynamic detection method based on piezoelectric transducers was experimentally validated for detecting the SC generation in the composite plate. It was found that the generated SC pulse by primary GW tone-burst exhibits a temporal waveform of approximate one-cycle pulse, and low-frequency piezoelectric ultrasonic transducers can be used to directly detect the quasistatic pulse signal associated with the SC generation. Furthermore, the cumulative SC signal generated by primary $A9$ mode at relatively high frequency under group velocity matching condition was found to be sensitive to the early hygrothermal damage and low-velocity impact damage in CFRP composite laminates. It was found that the magnitude of the SC pulse is linearly proportional to the hygrothermal change and low-velocity impact energies in CFRP composite plates. The

performed experimental examination validates the feasibility of the proposed approach for damage assessment in CFRP composites.

Data availability statement

All data that support the findings of this study are included within the article (and any supplementary files).

Conflict of interests

The authors declare that they have no known competing financial interests or personal relationships that could have appeared to influence the work reported in this paper.

ORCID iDs

Weibin Li ⓘ https://orcid.org/0000-0002-8925-6365
Mingxi Deng ⓘ https://orcid.org/0000-0001-9522-4039
Ching-Tai Ng ⓘ https://orcid.org/0000-0003-4638-2756

References

[1] Rajak D K, Pagar D D, Menezes P L and Linul E 2019 Fiber-reinforced polymer composites: manufacturing, properties, and applications *Polymers* **11** 1667
[2] Barile C, Casavola C and De Cillis F 2019 Mechanical comparison of new composite materials for aerospace applications *Composites* B **162** 122–8
[3] Rokhlin S, Chimenti D and Nagy P 2011 *Physical Ultrasonics of Composites* (Oxford: Oxford University Press)
[4] Krautkrämer J and Krautkrämer H 2013 *Ultrasonic Testing of Materials* (Berlin: Springer)
[5] Nicolais L, Meo M and Milella E (eds) 2011 *Composite Materials: A Vision for the Future* (Berlin: Springer)
[6] Jeffrey A and Hinkley J W C 2012 *Long-term Durability of Polymeric Matrix Composites* (Berlin: Springer)
[7] Yang W and Kundu T 1998 Guided waves in multilayered plates for internal defect detection *J. Eng. Mech.* **124** 311–8
[8] Aranguren G, Etxaniz J, Cantero-Chinchilla S, Gil-Garcia J M and Malik M K 2020 Ultrasonic guided wave testing on cross-ply composite laminate: an empirical study *Sensors* **20** 5291
[9] Su Z, Ye L and Lu Y 2006 Guided Lamb waves for identification of damage in composite structures: a review *J. Sound Vib.* **295** 753–80
[10] Soleimanpour R and Ng C-T 2017 Locating delaminations in laminated composite beams using nonlinear guided waves *Eng. Struct.* **131** 207–19

[11] Yin Z, Li C, Tie Y and Duan Y 2020 Impact damage detection in patch-repaired CFRP laminates using nonlinear Lamb waves *Sensors* **21** 219

[12] Li W, Cho Y and Achenbach J D 2012 Detection of thermal fatigue in composites by second harmonic Lamb waves *Smart Mater. Struct.* **21** 085019

[13] Li W, Lan Z, Hu N and Deng M 2021 Modeling and simulation of backward combined harmonic generation induced by one-way mixing of longitudinal ultrasonic guided waves in a circular pipe *Ultrasonics* **113** 106356

[14] Lv H, Zhang J, Jiao J and Croxford A 2020 Fatigue crack inspection and characterisation using non-collinear shear wave mixing *Smart Mater. Struct.* **29** 055024

[15] Li W, Deng M, Hu N and Xiang Y 2018 Theoretical analysis and experimental observation of frequency mixing response of ultrasonic Lamb waves *J. Appl. Phys.* **124** 044901

[16] Hasanian M and Lissenden C J 2017 Second order harmonic guided wave mutual interactions in plate: vector analysis, numerical simulation, and experimental results *J. Appl. Phys.* **122** 084901

[17] Zhang M Y, Xiao L, Qu W Z and Lu Y 2017 Damage detection of fatigue cracks under nonlinear boundary condition using subharmonic resonance *Ultrasonics* **77** 152–9

[18] Kundu T, Johnson D R, Wang K W and Kim J-S 2010 Investigation of the threshold behavior of subharmonics for damage detection of a structure with a breathing crack *Health Monit. Struct. Biol. Syst.* **7650** 765032

[19] Maier S, Kim J-Y, Forstenhäusler M, Wall J J and Jacobs L J 2018 Noncontact nonlinear resonance ultrasound spectroscopy (NRUS) for small metallic specimens *NDT&E Int.* **98** 37–44

[20] Chakrapani S K and Barnard D J 2017 Determination of acoustic nonlinearity parameter (β) using nonlinear resonance ultrasound spectroscopy: theory and experiment *J. Acoust. Soc. Am.* **141** 919–28

[21] Qu J M, Jacobs L J and Nagy P B 2011 On the acoustic-radiation-induced strain and stress in elastic solids with quadratic nonlinearity (L) *J. Acoust. Soc. Am.* **129** 3449

[22] Nagy P B, Qu J M and Jacobs L J 2013 Finite-size effects on the quasistatic displacement pulse in a solid specimen with quadratic nonlinearity *J. Acoust. Soc. Am.* **134** 1760–74

[23] Qu J M, Nagy P B and Jacobs L J 2012 Pulse propagation in an elastic medium with quadratic nonlinearity (L) *J. Acoust. Soc. Am.* **131** 1827

[24] Jiang C, Li W, Deng M and Ng C-T 2022 Quasistatic pulse generation of ultrasonic guided waves propagation in composites *J. Sound Vib.* **524** 116764

[25] Wan X, Tse P W, Zhang X, Xu G, Zhang Q, Fan H, Mao Q, Dong M, Wang C and Ma H 2018 Numerical study on static component generation from the primary Lamb waves propagating in a plate with nonlinearity *Smart Mater. Struct.* **27** 045006

[26] Sun X, Liu H, Zhao Y, Qu J, Deng M and Hu N 2020 The zero-frequency component of bulk waves in solids with randomly distributed micro-cracks *Ultrasonics* **107** 106172

[27] Jiang C, Li W, Deng M and Ng C-T 2021 Static component generation and measurement of nonlinear guided waves with group velocity mismatch *JASA Express Lett.* **1** 055601

[28] Sun X, Shui G, Zhao Y, Liu W, Hu N and Deng M 2020 Evaluation of early stage local plastic damage induced by bending using quasi-static component of Lamb waves *NDT&E Int.* **116** 102332

[29] Zhu W, Xu Z, Xiang Y, Liu C, Deng M, Qiu X, Sun D and Xuan F 2021 Nonlinear ultrasonic detection of partially closed cracks in metal plates using static component of lamb waves *NDT&E Int.* **124** 102538

[30] Deng M 2008 Second-harmonic generation of ultrasonic guided wave propagation in an anisotropic solid plate *Appl. Phys. Lett.* **92** 111910

[31] Deng M 2020 An experimental approach for detection of the acoustic radiation induced static component in solids *Chin. Phys. Lett.* **37** 074301

[32] Zhao J, Chillara V K, Ren B, Cho H, Qiu J and Lissenden C J 2016 Second harmonic generation in composites: theoretical and numerical analyses *J. Appl. Phys.* **119** 064902

[33] Song J, Kim S, Kim S, Cho Y and Kim Y 2021 Lamb wave propagation on a unidirectional CFRP plate: comparison of FEM simulations, experiments, and analytical calculations *J. Mech. Sci. Technol.* **35** 3863–9

[34] Wan X, Xu G, Zhang Q, Peter W T and Tan H 2016 A quantitative method for evaluating numerical simulation accuracy of time-transient Lamb wave propagation with its applications to selecting appropriate element size and time step *Ultrasonics* **64** 25–42

[35] Li W, Hu S and Deng M 2018 Combination of phase matching and phase-reversal approaches for thermal damage assessment by second harmonic Lamb waves *Materials* **11** 1961

[36] Gao G, Chen H, Hu N and Deng M 2021 Experimental observation of static component generation by Lamb wave propagation in an elastic plate *Ultrasonics* **117** 106537

[37] Liu L, Zhao Z, Chen W, Shuang C and Luo G 2018 An experimental investigation on high velocity impact behavior of hygrothermal aged CFRP composites *Compos. Struct.* **204** 645–57

[38] Cabral-Fonseca S, Correia J R, Rodrigues M P and Branco F A 2012 Artificial accelerated ageing of GFRP pultruded profiles made of polyester and vinylester resins: characterisation of physical-chemical and mechanical damage *Strain* **48** 162–73

[39] Ben Daly H, Ben Brahim H, Hfaied N, Harchay M and Boukhili R 2007 Investigation of water absorption in pultruded composites containing fillers and low profile additives *Polym. Compos.* **28** 355–64

[40] Starkova O, Buschhorn S T, Mannov E, Schulte K M and Aniskevich A 2013 Water transport in epoxy/MWCNT composites *Eur. Polym. J* **49** 2138–48

[41] de Souza Rios A, de Amorim Junior W F, de Moura E P, de Deus E P and de Andrade F J P 2016 Effects of accelerated aging on mechanical, thermal and morphological behavior of polyurethane/epoxy/fiberglass composites *Polym. Test* **50** 152–63

[42] Tsai Y I, Bosze E J, Barjasteh E and Nutt S 2009 Influence of hygrothermal environment on thermal and mechanical properties of carbon fiber/fiberglass hybrid composites *Compos. Sci. Technol.* **69** 432–7

[43] Solodov I Y, Krohn N and Busse G 2002 CAN: an example of nonclassical acoustic nonlinearity in solids *Ultrasonics* **40** 621–5

[44] Chronopoulos D 2018 Calculation of guided wave interaction with nonlinearities and generation of harmonics in composite structures through a wave finite element method *Compos. Struct.* **186** 375–84

[45] Li W and Cho Y 2016 Combination of nonlinear ultrasonics and guided wave tomography for imaging the micro-defects *Ultrasonics* **65** 87–95

[46] Guan R, Lu Y, Wang K and Su Z 2019 Quantitative fatigue crack evaluation in pipeline structures using nonlinear cylindrical waves *Smart Mater. Struct.* **28** 025015

Chapter 6: Quasistatic Component Generation of Group Velocity Mismatched Guided Waves in Tubular Structures for Microdamage Localization

6.1. Introduction, Significance, and Commentary

To extend the research of QSC by guided waves propagation, this study investigates the QSC generation by primary guide waves in pipe-like structures. Due to the geometrical difference, the guided wave types in pipe-like waveguides are rather different from those in plates. The study contains both the finite element simulation and the experiential study and covers the relevant content of QSC generation as much as possible regarding guided waves in isotropic cylindrical shells. This study also proposed a microdamage imaging technique that is based on the group velocity mismatch condition. The advantages of QSC generation in hollow cylinders include that the QSC pulse wave has less divergence loss and always exhibits the fastest pulse velocity. Based on the unique features of QSC, the proposed method can have promising applications on microdamage detection and localization with high sensitivity and cost-effectiveness.

6.2. Publication

This section is presented as published research paper by **Chang Jiang**, Weibin Li, Ching-Tai Ng, and Mingxi Deng (2024) Quasistatic component generation of group velocity mismatched guided waves in tubular structures for microdamage localization, *Applied Acoustics* 217:109813.

Statement of Authorship

Title of Paper	Quasistatic component generation of group velocity mismatched guided waves in tubular structures for microdamage localization
Publication Status	☑ Published ☐ Accepted for Publication ☐ Submitted for Publication ☐ Unpublished and Unsubmitted work written in manuscript style
Publication Details	Chang Jiang, Weibin Li, Ching-Tai Ng, et al. (2024) Quasistatic component generation of group velocity mismatched guided waves in tubular structures for microdamage localization, Applied Acoustics 217:109813.

Principal Author

Name of Principal Author (Candidate)	Chang Jiang		
Contribution to the Paper	Conceptualization, Methodology, Investigation, Data curation, Visualization, Writing - Original Draft		
Overall percentage (%)	80		
Certification:	This paper reports on original research I conducted during the period of my Higher Degree by Research candidature and is not subject to any obligations or contractual agreements with a third party that would constrain its inclusion in this thesis. I am the primary author of this paper.		
Signature		Date	2023.12.29

Co-Author Contributions

By signing the Statement of Authorship, each author certifies that:

  i.   the candidate's stated contribution to the publication is accurate (as detailed above);

  ii. permission is granted for the candidate in include the publication in the thesis; and

  iii. the sum of all co-author contributions is equal to 100% less the candidate's stated contribution.

Name of Co-Author	Weibin Li		
Contribution to the Paper	Resources, Writing - Review & Editing, Supervision, Funding acquisition		
Signature		Date	2023.12.29
Name of Co-Author	Ching-Tai Ng		
Contribution to the Paper	Resources, Writing - Review & Editing, Supervision		
Signature		Date	2023.12.29
Name of Co-Author	Mingxi Deng		
Contribution to the Paper	Writing - Review & Editing, Supervision		
Signature		Date	2023.12.29

Please cut and paste additional co-author panels here as required.

ELSEVIER

Quasistatic component generation of group velocity mismatched guided waves in tubular structures for microdamage localization

Chang Jiang [a,b], Weibin Li [b,*], Ching-Tai Ng [a,*], Mingxi Deng [c]

[a] *School of Architecture and Civil Engineering, University of Adelaide, Adelaide, South Australia 5005, Australia*
[b] *School of Aerospace Engineering, Xiamen University, Xiamen, Fujian 361000, China*
[c] *College of Aerospace Engineering, Chongqing University, Chongqing 400010 China*

ARTICLE INFO

ABSTRACT

Quasistatic component (QSC) of guided wave (GW) has relatively low attenuation due to low frequency and high sensitivity to microdamage. The group velocity matching between primary GW and its QSC or higher harmonics usually facilitates the measurement of nonlinear signals due to cumulative effect of amplitude, but it restricts the determination of microdamage location. While group velocity mismatch is general for most of the wave mode pairs in nonlinear GW testing, this study presents a novel method for identifying the location of early stage microdamage using QSC generation of ultrasonic GW propagation in tubular structures under group velocity mismatching condition. A three-dimensional finite element (FE) model is developed to provide insights into the generation and propagation characteristics of the QSC induced by both global material weak nonlinearity and simulated local microdamage in metallic pipes. The FE analysis verifies the L(0,1) mode of the QSC generated from propagations of different fundamental wave modes. The generation efficiency and cumulation feature of the QSC pulse are obtained and discussed. By exploiting the group velocity mismatching condition, a microdamage localization method is proposed based on the L(0,1)-QSC mode pair, which requires one-way excitation of only one primary wave. Experiments are conducted using early corrosion aluminum specimens to investigate the QSC pulse signals and verify the proposed method. The FE and experimental results demonstrate the fundamental properties of QSC generation by GWs in isotropic metallic hollow cylindrical structures. The feasibility of the proposed microdamage localization method is validated experimentally for promising industrial applications.

1. Introduction

Nonlinear ultrasonic techniques, such as vibroacoustic techniques [1], higher harmonic generation [2], sub-harmonic generation [3], and wave mixing [4,5] have been widely investigated in recent years for early stage microdamage detection and structural health monitoring. Owing to the high sensitivity to the microdamage in structural components, the nonlinear ultrasonic signals generated by the propagation of fundamental waves in materials with nonlinearities (i.e., material elastic nonlinearity, contact nonlinearity, hysteretic nonlinearity, etc.) were used as promising indices for testing and assessing variable materials in a cost-effective and non-destructive manner [6–8]. In particular, nonlinear acoustic methods combined with ultrasonic guided wave (GW) techniques are attracting great attention. By extending the inspection area to large structures in one operational procedure, nonlinear GW techniques can significantly lower the examining cost in comparison

with traditional point-to-point approaches [9,10].

However, one of the main drawbacks of nonlinear GW techniques is that the generated nonlinear waves suffer from great attenuation of many sources, and the signal-to-noise ratio (SNR) can be damped to a neglectable level after the primary wave propagates a long distance. Considering the second harmonic generation and GW mixing techniques, for instance, the synchronism and non-zero power flow conditions [11,12] are expected to be satisfied, such that the amplitude of harmonic wave packet increases continuously to a measurable degree during the period of wave-material nonlinearity interaction. Hence, new methods taking advantage of nonlinear acoustics merits but avoiding these restrictions are of prime importance for practical applications.

This study mainly focuses on the acoustic radiation-induced quasistatic component (QSC) generated by GW in isotropic metallic hollow cylindrical structures. The QSC pulse generation was first theoretically studied in isotropic homogenous one-dimensional space by Thurston,

Shapiro, and Cantrell [13,14]. Subsequently, Jacob, Narasimha, Nagy, and Deng studied the QSC generation in solids by theoretical, numerical, and experimental investigations [15–18]. One of the main findings of these studies in terms of the QSC in solids is that it possesses an envelope-like shape regarding the primary longitudinal tone-burst wave. However, for GW in thin plates or pipes, the dispersion feature of GWs complexes the analysis of QSC generation. Wan, Sun, Gao, and Jiang conducted finite element (FE) simulations and experiments for studying the QSC pulse generated from propagations of different modes of Lamb waves in thin aluminum plates, layered metallic plates, and CFRP laminated plates [19–24]. The QSC generated by Lamb waves was confirmed as S0 mode at near zero frequency for isotropic plates. The temporal waveform and generation efficiency of QSC were investigated and compared with second harmonics. It was found that the QSC generation is cumulative regardless of the synchronism condition as required by the cumulative second harmonic generation and GW mixing. Besides, the generation efficiency of QSC in composite plates is related to the fibre direction, wave mode of primary GW, and the excitation condition.

However, the generation efficiency and propagation characteristics (e.g., waveform, mode conversion, and cumulative effect) of QSC in tubular structures have yet to be explored and further utilized in practical applications. A significant difference between thin plates and tube-like structures is that the wave energy of the QSC generated in pipes has less diffusion than that in plates. Due to the low frequency of the QSC signal and the closed waveguide section, the nonlinear QSC pulse signal can promisingly propagate a longer distance than the higher harmonics. Besides, previous studies on QSC generation mainly employ piezoelectric transducers as signal receivers [18,20,21,24]. In those cases, the QSC signal can only be readily received and extracted when the primary GW acts as the carrier wave of QSC (i.e., the primary GW packet propagates simultaneously along with the QSC by the same group velocity). This is one of the main restrictions that limits the wave mode pairs selection and applications of QSC generation. More importantly, although the group velocity matching condition leads to the cumulative magnitude increase of nonlinear signals, it usually disables the microdamage localization when exciting only one fundamental GW and exploiting the correspondingly generated either QSC pulse or higher harmonics.

The present work aims at extending our recent investigations of QSC generation in thin plates [22–24] to the case of pipe-like structures. Importantly, the wave mode, waveform, cumulative feature, and generation efficiency of the QSC generated by different fundamental GW modes in pipes are investigated. Furthermore, a novel microdamage localization technique is proposed based on the use of QSC generation in pipes. The group velocity mismatch between the primary GW and the QSC is exploited as the key feature of the proposed method. Comparing to conventional techniques, firstly, the proposed damage detection and imaging method is based on the measurement of nonlinear ultrasonic response generation, which is closely related to the nonlinear elastic aspects and micro-structural misalignments of materials [11,12,23,24]. This feature makes it possible to detect the early-stage micro-damages in materials. On the contrary, traditional methods mostly measure the linear ultrasonic transmission, reflection, and scattering to evaluate the macro-damages and are insensitive to early-stage micro-damages [25]. For instance, Zhang et al. proposed a time-varying damage index based on one-dimensional convolutional neural network for detecting damages in plate-like structures [26]. However, the measured signals are mostly macro-damage scattered waves, which barely contain nonlinear ultrasonic responses induced by micro-damages. Other damage localization techniques involving Bayesian methods [27] are also based on the measurement of linear acoustic responses, presenting the similar drawback of being insensitive to micro-damages. Secondly, the proposed approach in this work takes advantage of the features of long-distance propagation and large inspection area of guided waves [25]. By contrast, traditional methods usually adopt the point-to-point inspection style, which is much less cost effective than guided wave

techniques [28,29]. Besides, the carrier wave of QSC of ultrasonic waves has a rather low frequency, which makes the QSC signal suffer from little attenuation during the propagation in solids [23,24]. Thus, the measurement of QSC generation can usually lead to higher SNR than that of higher harmonic generation.

The paper is structured as follows: in Section 2, the theoretical backgrounds of GW propagation and QSC generation in isotropic cylindrical structures are introduced. In Section 3, numerical study is conducted, and the FE signals are analysed and discussed. The microdamage localization technique is then developed in Section 4. In Section 5, an experimental study using a three-dimensional (3D) laser detecting system on an aluminum pipe with early corrosion is performed to validate the FE results and the proposed technique. Concluding remarks are presented in Section 6.

2. Theoretical considerations

2.1. Guided wave propagation in hollow cylinders

For analysis of the propagation of GWs in a hollow cylindrical structure, Fig. 1(a) shows the schematic of a hollow cylinder waveguide. The cylindrical coordinate system (r, θ, z) is used. For GW propagation along the Z axis, the displacement field of a fundamental mode can be deposed as $\boldsymbol{u}^{(1)} = (u_r^{(1)}, u_\theta^{(1)}, u_z^{(1)})$. The three particle displacement components can be expressed by

$$
\begin{aligned}
u_r^{(1)} &= U_r(r)\cos(n\theta)\exp[j(kz - \omega t)], \\
u_\theta^{(1)} &= U_\theta(r)\sin(n\theta)\exp[j(kz - \omega t)], \\
u_z^{(1)} &= U_z(r)\cos(n\theta)\exp[j(kz - \omega t)],
\end{aligned}
\tag{1}
$$

where $n = 0, 1, 2, \ldots$ is the circumferential order. Axis-symmetric modes are labelled by $n = 0$, and $n \geq 1$ for the flexural modes. $U_r(r)$, $U_\theta(r)$, and $U_z(r)$ are displacement amplitudes in terms of Bessel functions [25]. Due to the stress-free boundary conditions at the inner and outer surfaces of the cylindrical structure $\sigma_{rr} = \sigma_{rz} = \sigma_{r\theta} = 0$, $(r = a, b)$, the solution of the wave motion equation indicates that propagating GWs are dispersive, and are usually classified into three types: longitudinal mode: L(0, m), torsional mode: T(0,m), and flexural mode: F(n,m) [25].

In practical applications, the longitudinal and torsional modes, as the axisymmetric wave modes, are preferable to flexural mode due to advantageous excitability and abilities for convenient signal receiving and analysis. Furthermore, the lower order modes of longitudinal and torsional GWs are usually adopted in applications owing to less complex resultant GW signals when exciting a tone-burst GW of relatively low central frequency. For higher order GW modes at higher frequencies, it is generally difficult to excite and receive them with acceptable efficiency, and the multi-mode feature of GWs can make the signals rather complicated.

2.2. QSC generation in cylindrical shells

The QSC generation of GWs propagation in isotropic pipe-like waveguides has yet to be reported in literature. Based on the previous reports of QSC generation in thin plates [22–24], we can assume that, in a second order perturbation manner, the material nonlinearity of cylindrical structures can induce the second-order bulk driving force and surface driving traction due to the propagation of a primary GW, in the same way as the Lamb waves propagation in plates. As illustrated in Fig. 1(b), accompanying the primary GW propagation in materials with weak quadratic nonlinearity, there exists the QSC pulse and higher-order harmonic waves, which are generated by second-order bulk driving force $f^{(2)}(r, \theta)$ within the waveguide and second-order driving traction $s^{(2)}(r, \theta)|_{r=a,b}$ at the surfaces $r = a, b$. The $f^{(2)}$ and $s^{(2)}$ emerge from the quadratic terms in the nonlinear equation of motion. Hence,
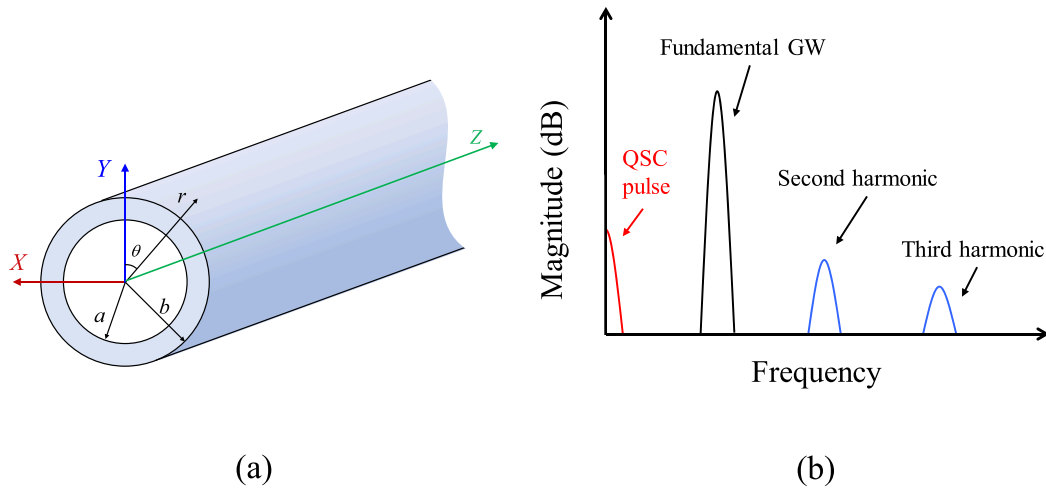
Fig. 1. (a) Schematic of hollow cylinder waveguide, (b) illustration of GW components in frequency domain.

the total GW field is $\boldsymbol{u} = \boldsymbol{u}^{(1)} + \boldsymbol{u}^{(2)}$. The Navier's governing wave equation for the traction-free waveguide and the corresponding boundary conditions at outer and inner surfaces are

$$\mu\nabla^2\boldsymbol{u} + (\lambda + \mu)\nabla\nabla\cdot\boldsymbol{u} = \rho\ddot{\boldsymbol{u}}, \tag{2}$$

$$\boldsymbol{P}(\boldsymbol{H})\cdot\boldsymbol{n}_r = 0. \tag{3}$$

where λ, μ are Lamé constants, ρ is the mass density, $\boldsymbol{P}$ is the first Piola-Kirchhoff stress tensor, $\boldsymbol{H}$ is the displacement gradient tensor, and $\boldsymbol{n}_r$ is the unit vector along the r axis.

By neglecting the second harmonic wave that usually requires satisfying the synchronism and non-zero power flow conditions [12,13] to form cumulative generation, the QSC generated by the zero-frequency components of $\boldsymbol{f}^{(2)}$ and $\boldsymbol{s}^{(2)}$ in the secondary GW field $\boldsymbol{u}^{(2)}$ is our focus. Analogous to QSC generation in plates, the QSC generated in pipes-like structures is assumed to have an invariable cumulative effect, since it is the temporal superposition of a series of nonlinear wave packets of zero-frequency (i.e., DC components). However, the cumulative effect of in QSC is supposed to display in two forms: the increase of amplitude when its group velocity is matched with that of the primary GW, and the increase of temporal width when its group velocity is different from that of the primary GW. In practice, tone-burst primary GW is widely adopted, and the DC components generated at each Z position during primary GW propagation are superposed into one nonlinear pulse signal, namely the QSC signal. However, the generation efficiency of QSC by different GWs is expected to be different, since the wave energy that flows from primary GWs to the nonlinear signals is affected by many factors, such as the mode shape and excitation magnitude of primary GWs.

3. Numerical studies

3.1. Dispersion curves & mode shapes

To study the features of QSC in tubular structures, and further confirm the feasibility of early-stage damage detection and localization using the QSC generation, numerical studies are conducted first. Table 1 lists the dimensions of the aluminum pipe, along with the density and

Table 1
Dimensions and material properties of aluminum pipe.

Outer diameter	Inner diameter	Density	Young's modulus	Poisson's ratio
38 mm	35 mm	2700 kg/m^3	70GPa	0.33

the elastic properties. Accordingly, the phase velocity and group velocity dispersion curves of such pipe are calculated by DISPERSE [30] and plotted in Fig. 2(a) and 2(b). To compare the generation efficiency and cumulative effect of QSC by different primary GWs, GWs of L(0,1), T(0,1), and L(0,2) modes at 200 kHz are in turn chosen as the fundamental modes. The properties of these three mode pairs are summarized from the DISPERSE calculations and listed in Table 2. Moreover, the mode shapes of these three primary modes, as well as a low-frequency L(0,1) mode at 1 kHz (for comparing with QSC by 3D FE analysis), are calculated by SAFE method [31] and shown in Fig. 3. It should be noted that the calculated results by DISPERSE and SAFE method are compared to each other and are verified to be correct.

3.2. 3D FE model

The 3D FE wave propagation analysis is achieved in Abaqus/Explicit CAE software. GWs of three different modes in an aluminum pipe are adopted as primary waves to induce the interaction of the ultrasound with the material nonlinearity of the pipe. The material nonlinearity of the metallic pipe is carried out by incorporating a user-defined subroutine of Murnaghan constitutive material model. The 3D FE model is illustrated in Fig. 4(a). The primary GWs are introduced into the pipe by prescribing Hann windowed sinewave displacements on the left end boundaries of the pipe. The cycle numbers of the tone-burst signals are 10. The primary waves propagate along the Z direction. According to the mode shapes shown in Fig. 3, for primary L(0,1) mode, the displacement prescribed on the outer boundary at the left end is identical to that prescribed on the inner boundary at the left end in the r direction. This is to excite a pure L(0,1) mode such that other modes are in absence of complicating the subsequent signal analysis. The maximum displacement is 2.8×10^{-6}m. Fig. 4(b) shows the displacement boundary conditions and several snapshots of the L(0,1) GW propagation in Abaqus/CAE views. Similarly, for primary T(0,1) mode, only the outer boundary is prescribed with the displacement in the circumferential θ direction. The maximum displacement is 1.0×10^{-6}m. For L(0,2) mode, the same Hann windowed displacements are prescribed on the outer and inner boundaries at the left end in the Z direction. The maximum displacement is 1.3×10^{-6}m. These three excitation conditions are parametrically optimized such that the introduced GWs have the same fundamental amplitudes (1.0×10^{-6}m) while propagating in the pipe, which facilitates the analysis and comparison of the correspondingly generated nonlinear signals.

Since the focus of this study is early-stage damage detection using QSC, we avoid the macro-damage modelling in terms of thickness reduction. During the early stage of general corrosion process in
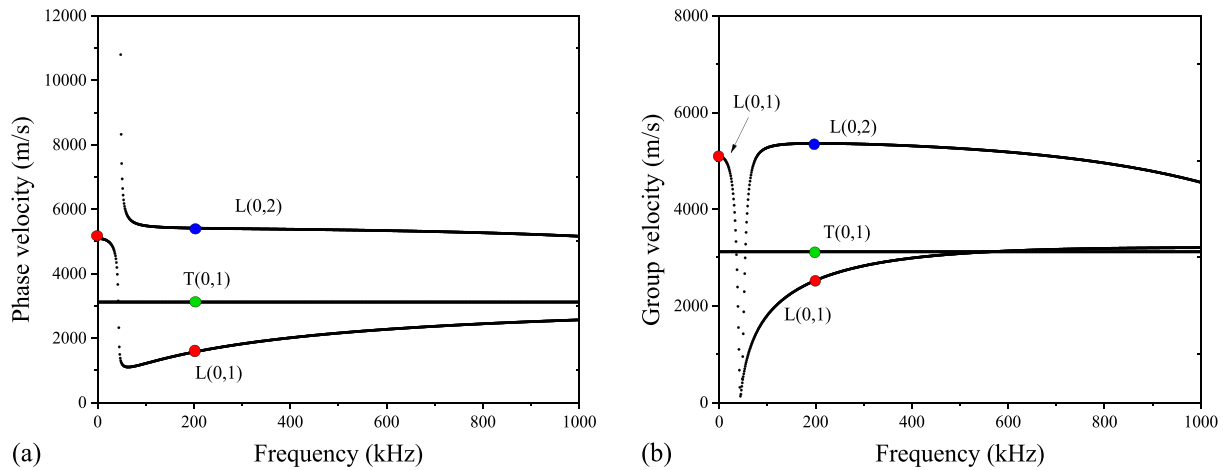
Fig. 2. Dispersion curves of aluminum pipe with outer diameter 38 mm and inner diameter 35 mm, (a) phase velocity, (b) group velocity.

Table 2
Theoretical wave mode properties.

Primary wave	L(0,1)	T0,1)	L(0,2)
Frequency (kHz)	200	200	200
Phase velocity (m/s)	1574	3122	5415
Group velocity (m/s)	2531	3122	5361
Wavelength (mm)	7.9	15.6	27.1

aluminum, it is the microstructural change (e.g., the nucleation and growth of corrosion pits) that dominates [32]. The diameter and depth of corrosion pits are usually on the order of microns, and the effect on strength is neglectable. This type of microdamage is usually undetectable for kilohertz-level linear ultrasonic approaches due to their size smaller than the wavelength. On the other hand, the modelling of these geometric microstructures (e.g., corrosion pits and crevices) is also undesirable in the time-domain 3D FE analysis of relatively large computational load, as they can readily cause singularities and non-convergence in the numerical study [33]. A feasible approach is to approximately equate the microdamage to reasonable increases of third-order elastic constants (TOECs), as they both lead to evident nonlinear ultrasonic responses due to similar mechanisms for fatigue and thermal damages in materials [28]. Based on these considerations, we keep the Young's modulus and Poisson's ratio of the damaged area invariant, and scale up the original TOECs (Murnaghan model: $l = -2.5 \times 10^{11}$, $m = -3.3 \times 10^{11}$, $n = -3.5 \times 10^{11}$, unit: Pa) of the material strain energy function by different times in the local area. The damage area starts at Z_1, and the width is denoted as d. The central angle of the damaged area is denoted by α. For signal receiving, point-probes are placed on the circumferential outer surface of the pipe. The global coordinate of a point position is denoted by (x, y, z). The received displacement in the X, Y, and Z directions are denoted by $U1$, $U2$, and $U3$, respectively. Alternatively, for an intuitive understanding of GW propagation, the circumferential and radial displacements described in a cylindrical coordinate system are denoted by U_θ, U_r and U_z, respectively. To avoid boundary reflections of GWs, the total length of the 3D model is 4 m. The whole geometry is meshed with structured hex element of size 4.0×10^{-4}m ($< \lambda/20$, λ is the wavelength of fundamental wave) for suitable computational accuracy of all possible secondary GW modes. The time step of computation is set as 5×10^{-8}s. The convergence of the model is confirmed by the fact that the velocity and amplitude of the fundamental wave barely change when furthermore decreasing the mesh size and time step.

3.3. Results & discussion

Firstly, the generation and propagation characteristics of QSC in pipes are obtained and discussed. There are three primary FE cases in total: (i) L(0,1)-QSC case, (ii) T(0,1)-QSC case, and (iii) L(0,2)-QSC case. In each primary mode pair case, there are two sub-cases: (a) propagation in an intact pipe, and (b) propagation in a locally damaged pipe. After the mode verifications of the excited fundamental GWs, the wave mode, waveform, generation efficiency, and cumulative effect of the correspondingly generated QSCs are analysed and discussed. Secondly, a parametric study of the local damage is conducted based on variations of size, TOECs, and locations. The resultant QSC generations are compared and further referred to for proposing the microdamage localization technique.

3.3.1. L(0,1)-QSC case

For the L(0,1)-QSC excitation case, Fig. 5 shows the received time-domain signals by the point-probes set at 0°at different locations (Fig. 5(a): without local damage; Fig. 5(b): with local damage). As shown in Fig. 5(a), the primary wave mode L(0,1) (black line, mainly U_r) is excited into the aluminum pipe. From the time-of-flight calculation, the group velocity of the L(0,1) mode is about 2524 m/s, which accords with the dispersion curves in Fig. 2. Due to the global weak material nonlinearity, the red lines (U_z) show the nonlinear signals (i.e., QSC and second harmonic) obtained by applying the phase-reversal method [3,23]. The first quasistatic displacement is confirmed as the QSC pulse signal and the calculated group velocity is about 5071 m/s, which is consistent with the dispersion curve of L(0,1) mode at zero frequency. Since there exists a group velocity mismatch between the primary L(0,1) mode and the QSC pulse (L(0,1) mode at nearly zero frequency), the cumulative effect of the QSC generation is evidenced by the increase of its pulse width after its amplitude increases to a certain degree. This cumulative phenomenon of QSC pulse is similar to that of GW propagations in plates [22–24].

For the local damage case (Fig. 5(b)), the microdamage is created by artificially increasing the value of TOECs. The magnification factor for the nonlinear elastic coefficients is $\xi_N = 1.5$, and the microdamage is modelled at: $Z_1 = 0.3$ m, $d = 0.05$ m, $\alpha = 360°$. Thus, there is a local pulse (at about 3×10^{-4}s) after the first quasistatic displacement pulse (at about 2×10^{-4}s). The local damage increases the amplitude of the QSC signal to a greater level. This is because the local micro-damage is acting as a wave energy transfer station, where the power of primary GW transfers into the nonlinear signals. Consequently, due to the group velocity mismatch, the newly generated QSC pulse signal is propagating faster than the primary L(0,1) mode, and slower than the QSC pulse signal induced by the global weak material nonlinearity. Hence, this
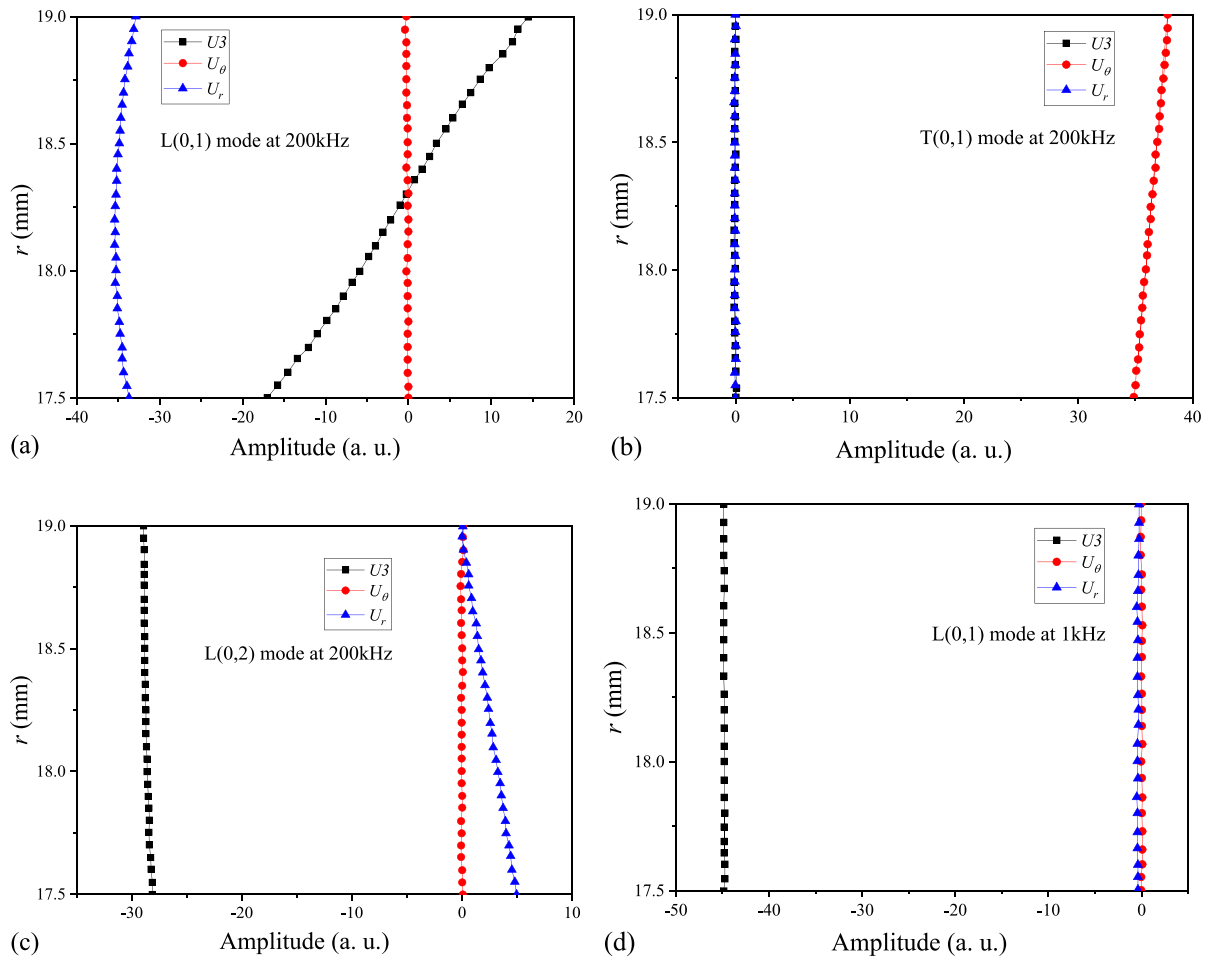
Fig. 3. Wave structures of (a) L(0,1), (b) T(0,1), and (c) L(0,2) modes at 200 kHz, (d) wave structure of L(0,1) mode at 1 kHz in the hollow cylinder of outer diameter 38 mm and inner diameter 35 mm.

local pulse occurring at about $t = 3 \times 10^{-4}$s can be a promising index to determine the location of the microdamage.

3.3.2. T(0,1)-QSC Case

For the T(0,1)-QSC excitation case, Fig. 6 shows the time domain signals of the primary T(0,1) mode picked up in the circumferential θ direction and the corresponding nonlinear signals received in Z direction. The mode of the primary wave is confirmed by the calculated group velocity (around 3135 m/s). The first displacement shift of the nonlinear signal indicates the QSC generated from the global material nonlinearity. The calculated group velocity of this first QSC pulse is about 5102 m/s. These results confirm the modes of the primary wave and the nonlinear QSC pulse signal as T(0,1) and L(0,1), respectively. Besides, as shown in Fig. 6(a), the cumulative effect of QSC is similar to the case of L(0,1)-QSC. The group velocity mismatch leads to an increase in pulse width during the primary wave propagation.

On the other hand, when there is a local microdamage same as that in Section 3.3.1, the temporal waveform of the QSC signal is similar to that generated from the propagation of L(0,1) mode shown in Fig. 5(b). Since the waveform at the ending part of the received signal is usually influenced by the excitation conditions [16,23], only three segments of this nonlinear signal draw our attention: (i) the QSC generated by global weak material nonlinearity, (ii) the QSC generated by the local microdamage, and (iii) the second harmonic generated by either one of both. A difference exists between these two nonlinear signals shown in Fig. 5(b) and Fig. 6(b). By keeping the magnitudes of primary GWs of L(0,1) and T(0,1) identical, we find that the QSC displacement generated by L

(0,1) with the microdamage is larger than the globally generated QSC, while this is opposite to the T(0,1)-QSC case. This is mainly because generation efficiencies of QSC signals from these two primary GWs with different mode shapes are different. Similar characteristic of QSCs in thin plate-like structures has been reported [22–24]. Besides, for the L(0,1)-QSC case, the retained L(0,2) mode of a quite small magnitude during excitation can result in the second harmonic generation of the L(0,2) mode as the phase-matching condition is satisfied [12,13]. For the T(0,1)-QSC case, only T(0,1) mode is excited into the pipe, and the resultant second harmonic is generated mainly due to the local microdamage without showing an obvious cumulative effect. However, the amplitudes of these second harmonics are too small to be exploited, and the focus of this study is on the QSC signals.

3.3.3. L(0,2)-QSC case

For the L(0,2)-QSC excitation case, the mode of the primary wave is validated by the calculated group velocity of around 5341 m/s. Besides, it is noted from the dispersion curves in Fig. 2 that the primary L(0,2) at 200 kHz has almost the same phase velocity and group velocity as that of L(0,2) at 400 kHz. As a result, the synchronism and non-zero power flow conditions, which are required by the cumulative second harmonic generation, are satisfied to a large extent. As shown in Fig. 7, the cumulatively generated second harmonic propagates with the primary L(0,2) mode. In the meantime, the generated QSC pulse also has a similar group velocity to the primary wave, and is confirmed as L(0,1) mode. Based on our previous studies [22–24], we infer that the QSC generated in pipes gains much more energy from the primary GW propagation than
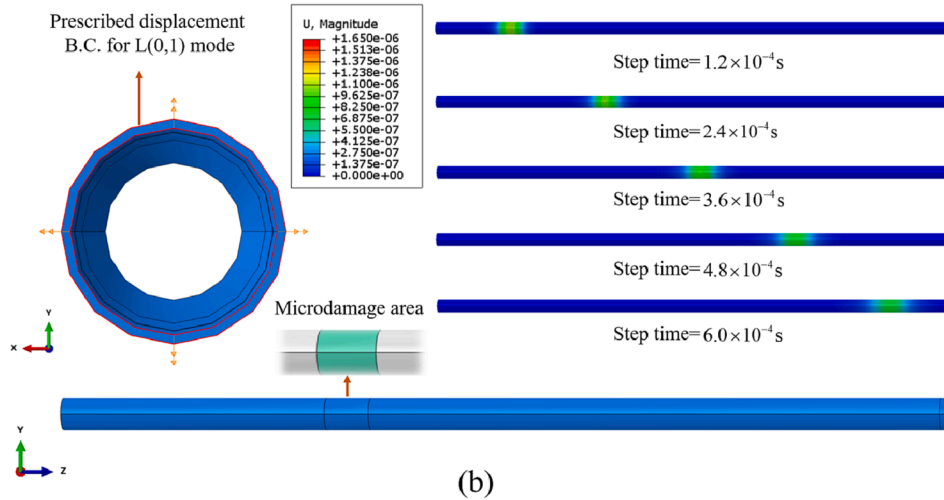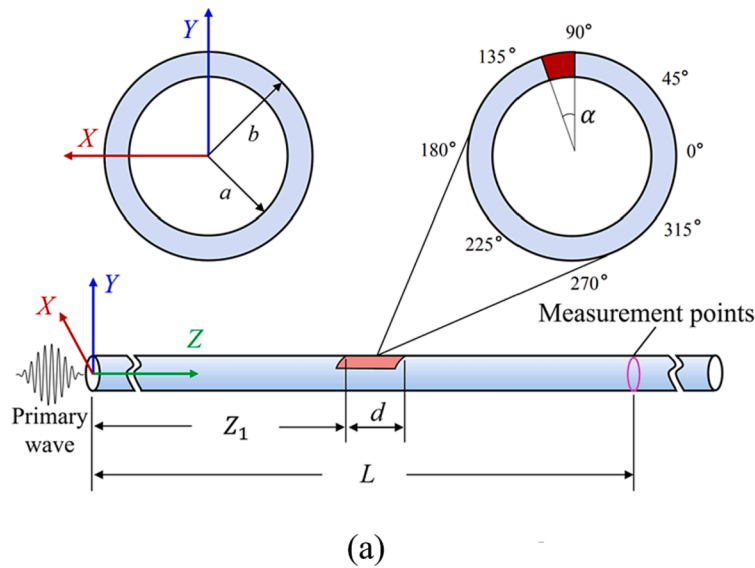
(a)

(b)

Fig. 4. 3D FE model of GW propagation in aluminum pipe with local microdamage: (a) schematic, (b) CAE views of 3D model and snapshots of GW propagation.

a phase-match second-order harmonic due to little divergence of GW from the closed cross-section of pipes. However, with both phase velocity and group velocity matched with each other, this L(0,2)-L(0,2) mode pair for second harmonic generation, and L(0,2)-L(0,1) mode pair for QSC generation, are both not feasible for microdamage localization. The nonlinear signals generated by the global material nonlinearity and the local damage is always accompanied by each other, which do not provide any location information of the local damage.

3.3.4. Parametric study of QSC generation

As we have confirmed that the QSC induced by different GW modes in isotropic metallic tubular structures is always L(0,1) mode at near-zero frequency, a parametric study is conducted to further analyse the generation efficiency of QSC. As shown in Fig. 8(a), the magnitude of QSC (denoted by time-domain integration $\int U_z$) is always linear proportional to the square of the amplitude of primary GW. Also, the L(0,2) mode can induce the QSC at the largest efficiency in terms of excitation amplitude, followed by T(0,1), and L(0,1) the least. Besides, as shown in Fig. 8(b), by keeping the amplitude, frequency, and cycle number of primary GW identical, the comparative ranking of generation efficiency of QSC with respective to propagation distance by these primary modes is still L(0,2) > T(0,1) > L(0,1). However, as shown in Fig. 8(c), the QSC generation by primary L(0,1) is most sensitive to the increase of

nonlinear elastic constants, followed by L(0,2), and T(0,1) the least. Table 3 summarizes the main features of QSC generation by GW propagation in tubular structures.

To develop the microdamage localization technique, we further conducted a parametric study of the QSC generated from primary GW modes with local microdamage. By adjusting the magnification factor ξ_N, microdamage area, and microdamage location, the resultant QSC signals are analysed and compared. As shown in Fig. 9(a), for a fixed microdamage area at $Z_1 = 0.3$m, $d = 0.05$m, and $\alpha = 360°$, the second local pulse signal increases with the magnification factor ξ_N. However, as shown in Fig. 9(b), this trend is more obvious for L(0,1) excitation, which is consistent with the result shown in Fig. 8(c). It indicates that larger nonlinear elastic coefficients of the material can lead to larger amplitude of the QSC signal generated by the primary L(0,1) GW. As the existence of microdamage in metallic materials can usually be related with the nonlinear elastic property [28], this result also indicates that the magnitude of a measured QSC signal can be promisingly used for quantitatively evaluate the damage degree of a local microdamage.

Moreover, we keep the $Z_1 = 0.3$m, $d = 0.05$m, and $\xi_N = 1.5$ unchanged, and adjust the α parameter to obtain Fig. 9(c). It is found that, as the microdamage area increases in the circumferential direction, the amplitude of the QSC increases as well. However, while we keep the $Z_1 = 0.3$m, $\xi_N = 1.5$, and $\alpha = 360°$ unchanged, and adjust the
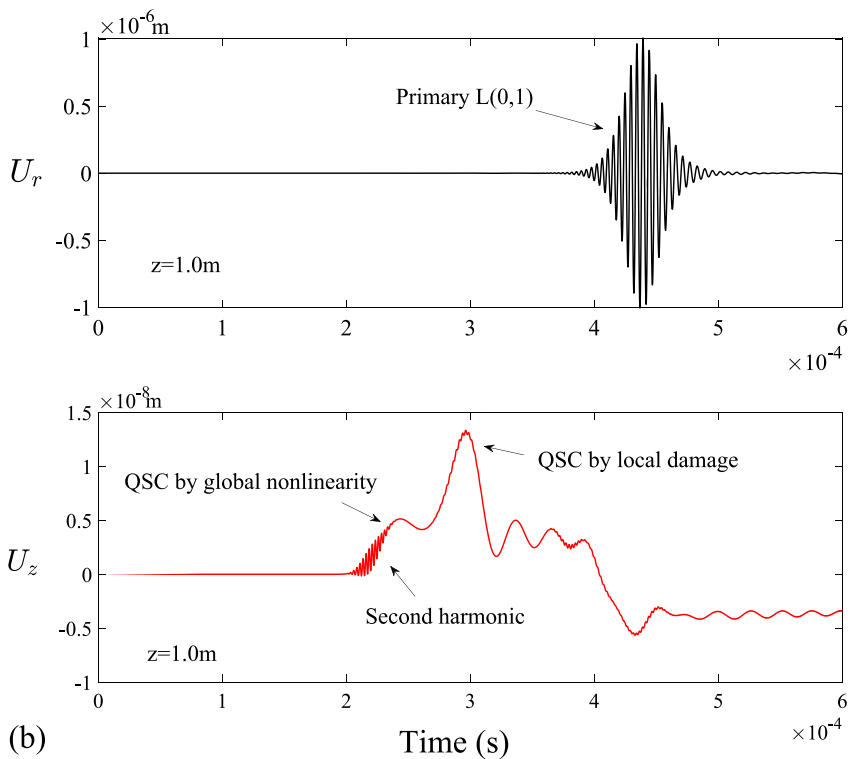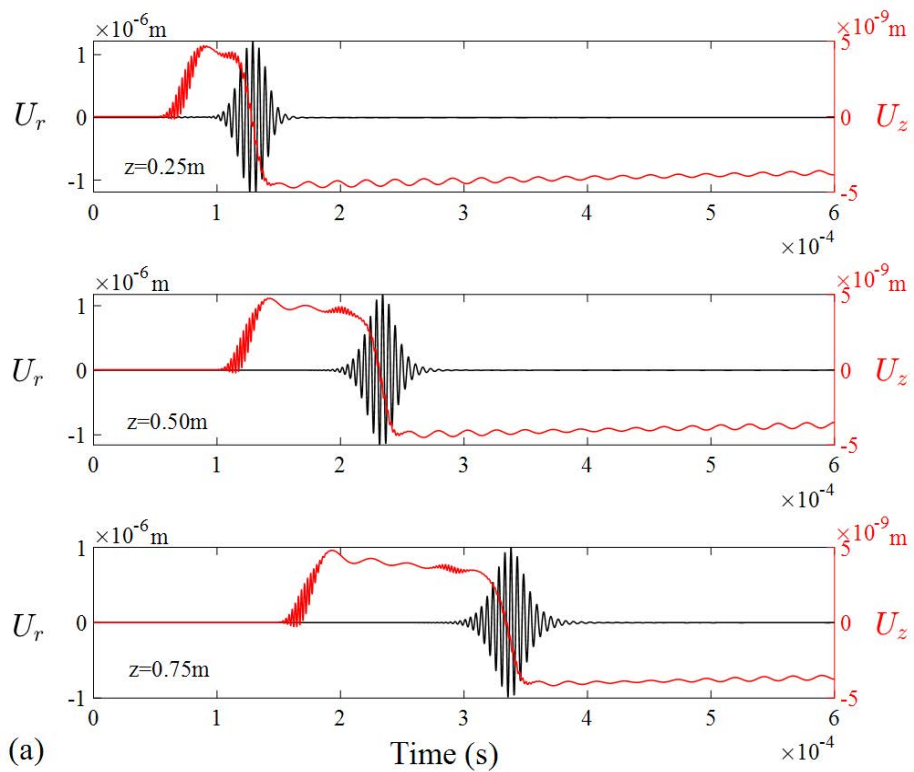
Fig. 5. Time domain signals of primary L(0,1) GW received in *r* direction (black lines) and nonlinear signals received in *Z* direction (red lines): (a) for intact pipe, (b) pipe with a local damage.
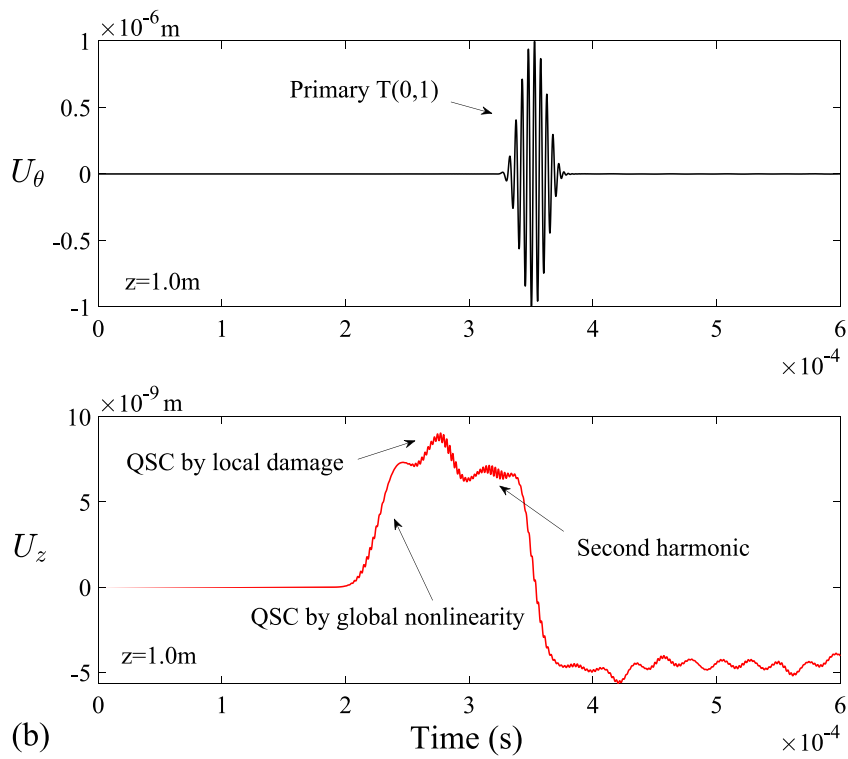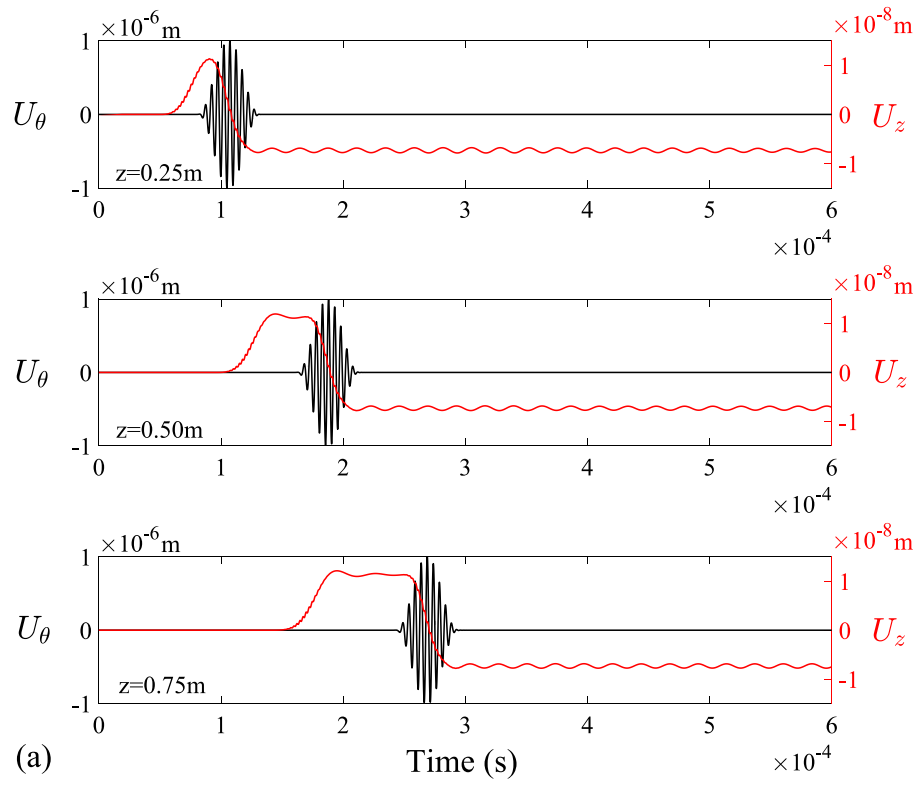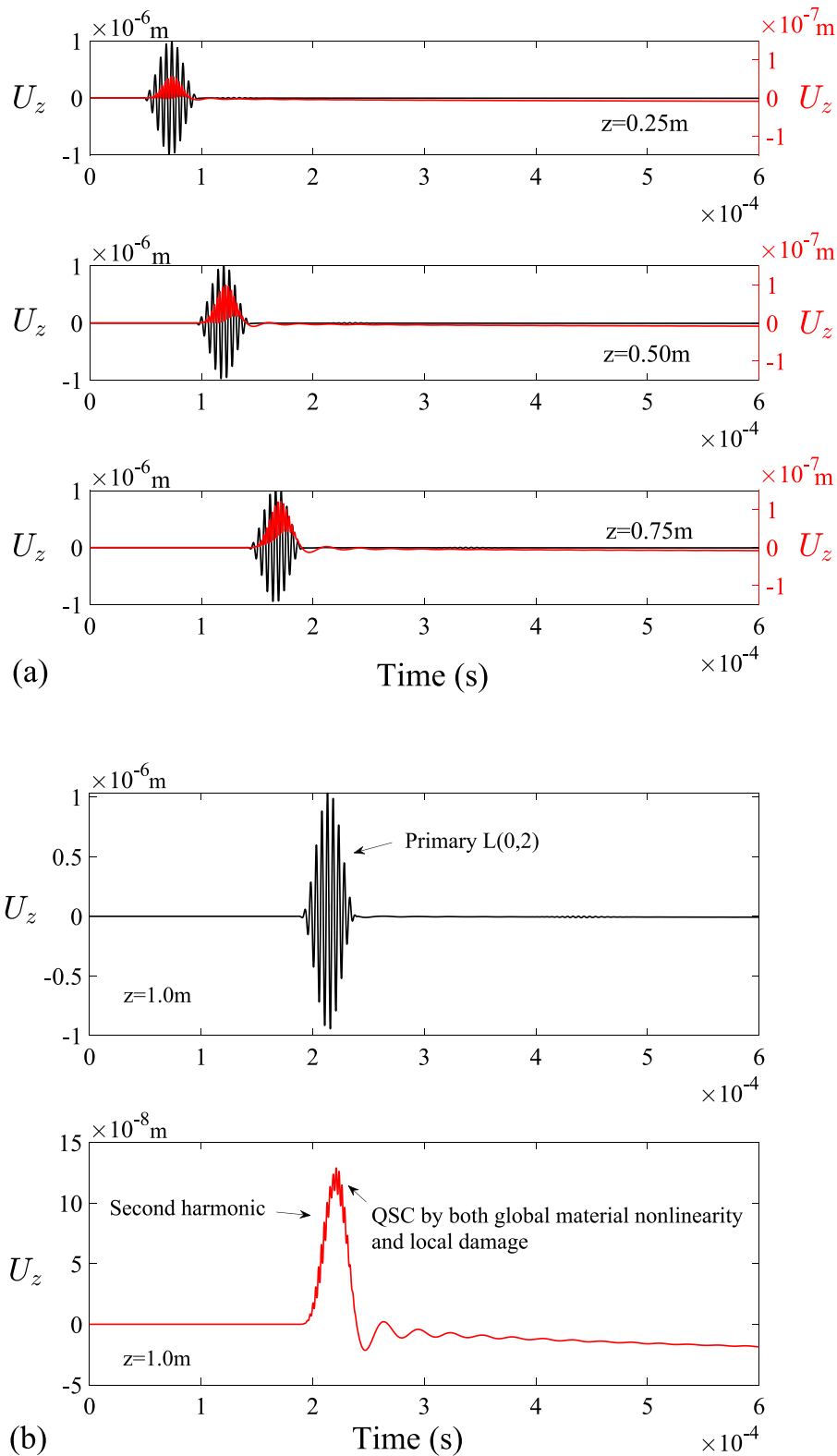
Fig. 6. Time domain signals of primary T(0,1) GW received in θ direction (black lines) and nonlinear signals received in Z direction (red lines): (a) for intact pipe, (b) pipe with a local damage.

Fig. 7. Time domain signals of primary L(0,2) GW (black lines) and nonlinear signals (red lines) received in *Z* direction: (a) for intact pipe, (b) pipe with a local damage.

d parameter, the result presented in Fig. 9(d) shows that the magnitude of QSC signal increases both in amplitude and in temporal width. The increase in amplitude dominates first and stops after the amplitude increases to a certain degree. Finally, the increase of QSC magnitude only occurs in temporal width. Based on the previous studies of QSC in thin

plates [22–24], and the QSC generations in intact cylindrical structures (see Fig. 5(a) and Fig. 6(a)), it is suggested that this phenomenon is due to the group velocity mismatch between the primary L(0,1) GW and the correspondingly generated QSC. Thus, an integral of the local QSC pulse displacement over a certain time range can be a promising index to
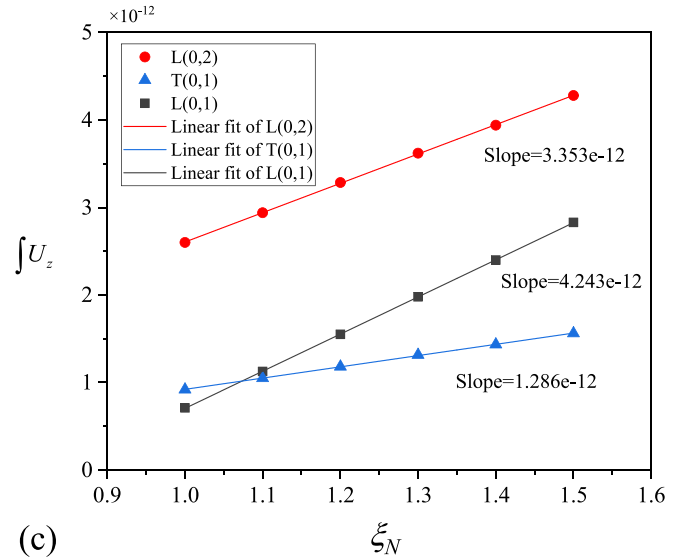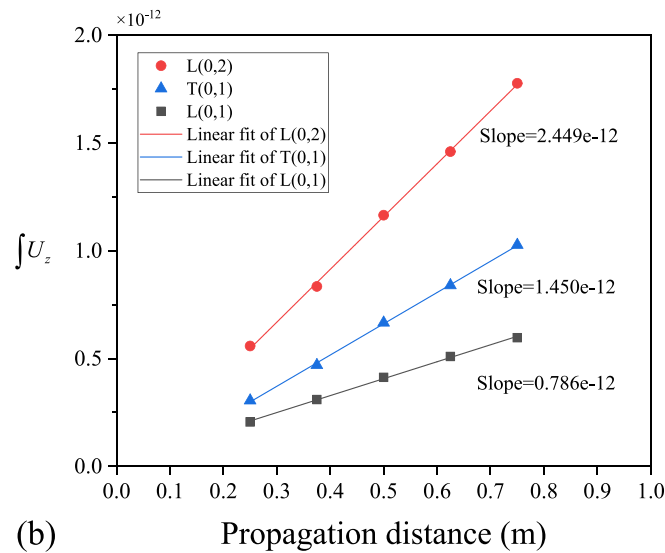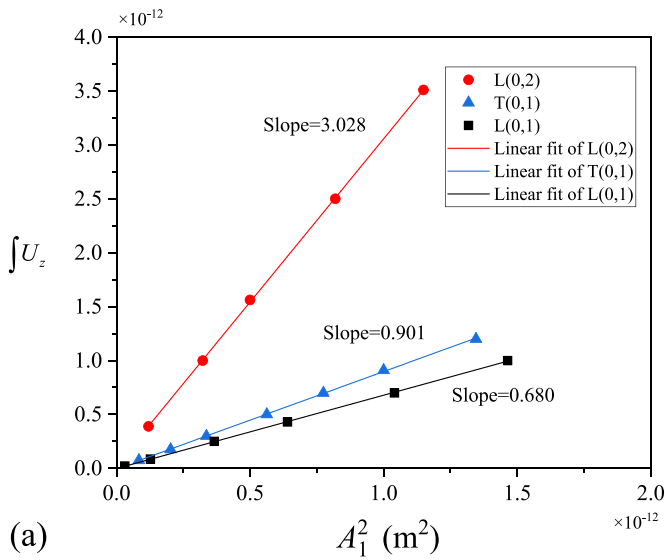
Fig. 8. Comparisons of QSC generation efficiency in intact pipe: magnitude of QSC with respect to (a) amplitude of primary GW, (b) propagation distance, and (c) magnification factor of nonlinear elastic constants.

Table 3
Features of QSC by GWs in tubular structures.

Primary wave mode (200 kHz, 10 cycles)		L(0,1)	T0,1)	L(0,2)
Generated QSC mode ($\approx$0Hz)		L(0,1)	L(0,1)	L(0,1)
Group velocity mismatch	Yes	Yes	No	
QSC generation efficiency (unit: a. u.) with respect to:				
	Primary wave amplitude	0.680	0.901	3.028
	Propagation distance	0.786	1.450	2.449
	Nonlinear elasticity	4.243	1.286	3.353

evaluate the total damage degree of the local area. Finally, Fig. 9(e) shows the different QSC signals by adjusting the Z_1 parameter while keeping the others unchanged. It is found that the second displacement

pulse in the QSC signal induced by the local microdamage occurs at different times corresponding to the starting position of the microdamage area. This further indicates that a local microdamage can be promisingly localized using the QSC generation of a primary GW under the group velocity mismatch condition.

4. Microdamage localization method

After confirming the propagation features of the QSC pulse signal in isotropic hollow cylindrical structures, a microdamage localization technique is proposed as follows. By choosing a suitable mode pair with the group velocity mismatch condition, the L(0,1) mode at frequency f is adopted as primary GW. As shown in Fig. 10(a), by reasonably overlooking the thickness of the thin-walled cylindrical structure, we unwrap its outer surface into a planar area (coloured dark blue) and discretise it into a number of grid points. The position of a given local microdamage point on the aluminum pipe can be denoted by $(z, R\theta)$, where R denotes the outer radius of the pipe-like structure. Thus, the primary wave first propagates from $z = 0$ m to the damage location $(z, R\theta)$. Then, the QSC pulse signal is generated from the interaction of microdamage with the

primary wave. Finally, the QSC pulse signal propagates towards the receiving probes. The group velocity on the first propagation path is

$$\tau_i^Q(z, R\theta) = \frac{z}{c_g^{L(0,1)}} + \frac{\sqrt{\min^2\left(|R\theta - R\theta_i|, 2\pi R - |R\theta - R\theta_i|\right) + (L + W - z)^2}}{c_g^{SC}}, \qquad i = 1, \quad 2, \quad \ldots \quad , \quad M, \tag{5}$$

denoted by $c_g^{L(0,1)}$, and is denoted by c_g^{SC} on the second propagation path. The excitation signal is expressed by

$$S^{L(0,1)}(\tau) = \frac{A}{2}\sin(2\pi f\tau)\left[1 - \cos\left(\frac{2\pi f\tau}{N}\right)\right], \qquad \tau \in \left[0, \frac{N}{f}\right], \tag{4}$$

where A is the maximum displacement, f is the frequency, and N is the cycle number of the tone-burst. For the wave-damage interaction at $(z, R\theta)$, the theoretical arrival time of the newly generated QSC pulse is calculated as

where R is the outer radius of the pipe, θ_i denotes the circumferential position of a receiving probe i, W is the wave-packet length of the primary mode, M is the total number of probes, and Q denotes the arrival time point as shown in Fig. 10(b) and 10(c). Referring to the previous studies [22–24] and the temporal signals obtained in Section 3, the theoretical QSC signal is then constructed as
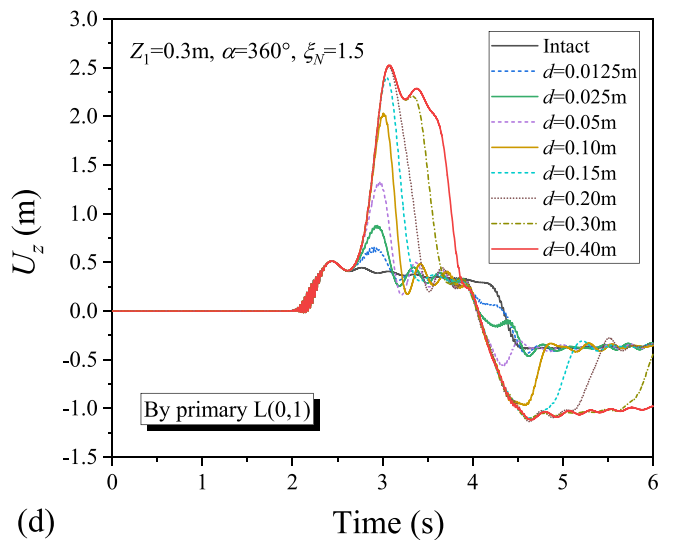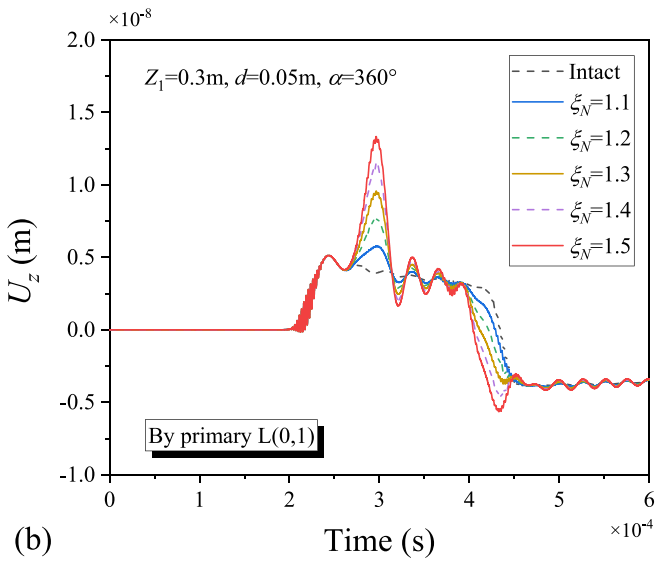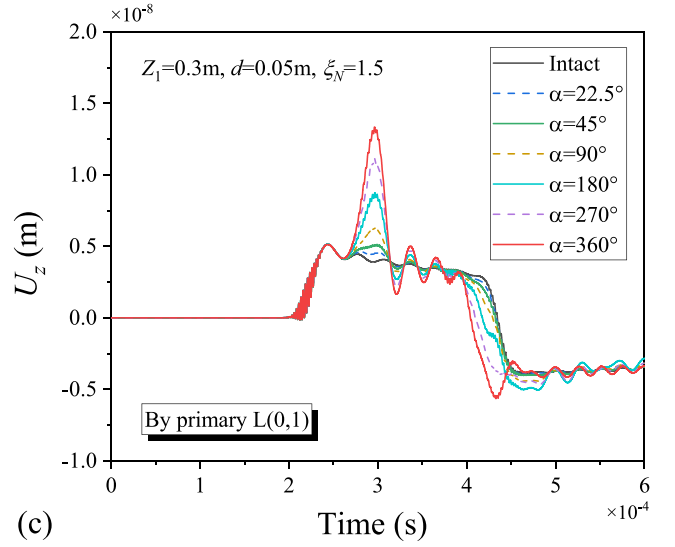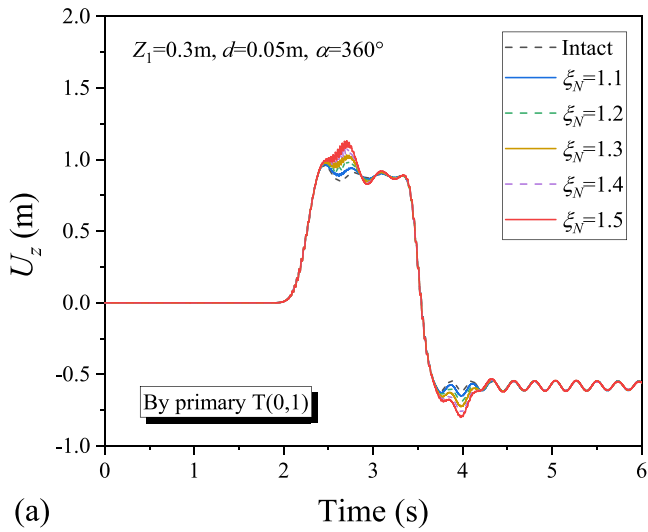

Fig. 9. Parametric study of QSC generation: (a) adjusting only ξ_N for T(0,1) excitation, (b) adjusting only ξ_N for L(0,1) excitation, (c) adjusting only α, (d) adjusting only d, and (e) adjusting only Z_1.
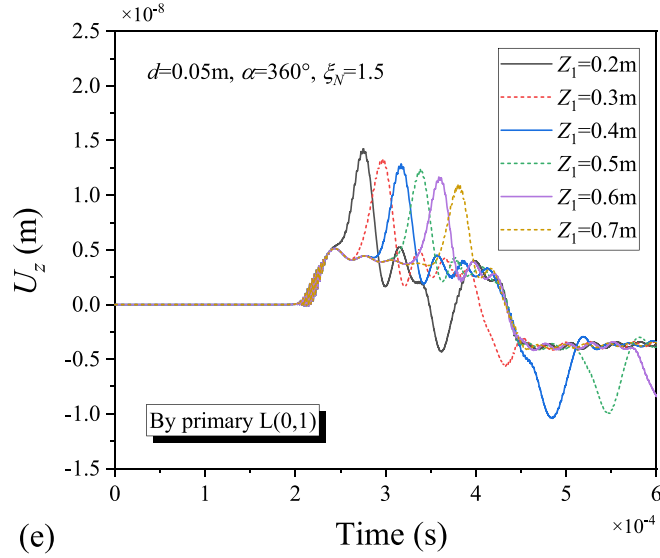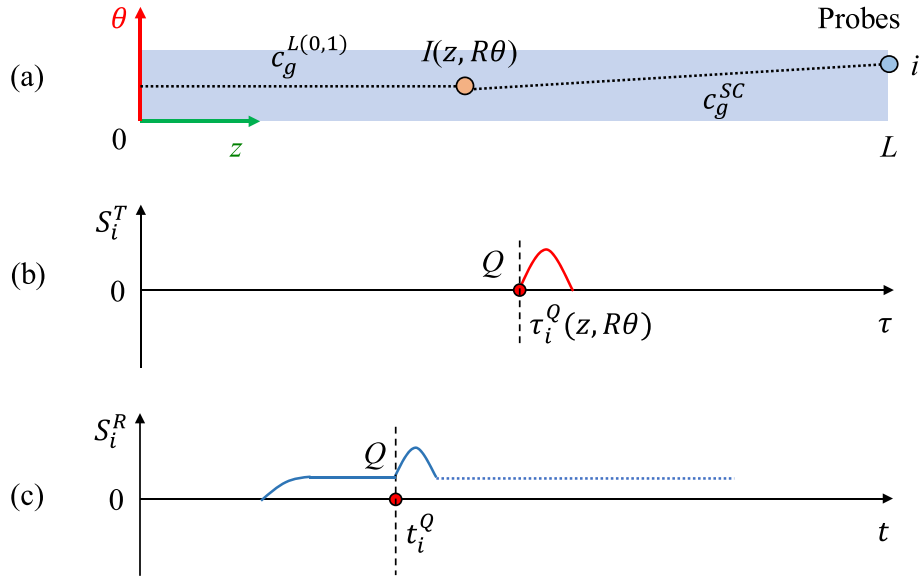
Fig. 9. (*continued*).

Fig. 10. Microdamage localization method: (a) illustration of GW propagation path, (b) constructed theoretical signal, (c) illustration of a typical received QSC signal.

$$S_i^T(\tau) = \left| S^{L(0,1)}\left(\tau - \tau_i^Q\right) + jH\left[S^{L(0,1)}\left(\tau - \tau_i^Q\right)\right] \right|, \qquad \tau \in \left[0, \frac{L+W}{c_g^{L(0,1)}}\right], \tag{6}$$

where H denotes the Hilbert transform, j is the imaginary unit. Fig. 10(b) shows the illustration of the theoretical QSC signal by Eq. (6). The physics here is that every DC component that constructs the final QSC signal by superposition possesses an envelop-like shape regarding the primary wave. Subsequently, the intrinsic correlation of the theoretical damage signal $S_i^T(\tau)$ and the practical received QSC signal $S_i^R(t)$ is calculated as

$$XR_i(\delta) = \int_{t_1}^{t_2} \overline{S_i^T(\tau)}\left[S_i^R(\tau+\delta) - S_i^{R0}(\tau+\delta)\right]d\tau, \tag{7}$$

$$t_1 = \frac{L+W}{c_g^{SC}} + \frac{N}{f}, t_2 = \frac{L}{c_g^{L(0,1)}},$$

where $\overline{S_i^T}$ is the complex conjugate of S_i^T, S_i^{R0} is the measured QSC signal by receiving probe i in an intact specimen, and δ is the time shift variable of the cross-correlation result. The nonlinear signals S_i^R and S_i^{R0} can be extracted from the measured data using phase reversal approach and low-pass filtering [23]. Finally, the microdamage index at each grid point $(z, R\theta)$ is given by

$$I(z, R\theta) = \sum_{i=1}^{M} XR_i(0). \tag{8}$$

It should be noted that, in practical applications, the propagating primary GW excited by a tone-burst high voltage through the transducer usually contains a few other GW modes of relatively smaller magnitudes. This is mainly due to the imperfect boundary excitation conditions of the primary GW, such as the inconsistent coupling conditions of the transducers attached around the cylindrical specimen. However, based on the analysis of QSC generation in Section 3, all GW modes in the isotropic hollow cylindrical structures are expected to induce the QSC signals of

the same L(0,1) mode at near-zero frequency. This characteristic of QSC generation facilitates the eventual signal postprocessing. The theoretical QSC signal S_i^T in Eq. (6) constructed for the calculation of signal correlation can then be modified to

$$S_i^T(\tau) = \left| P_i^R\left(\tau + t_2 - \tau_i^O\right) + jH\left[P_i^R\left(\tau + t_2 - \tau_i^O\right)\right] \right|, \qquad \tau \in \left[0, \frac{L+W}{c_g^{L(0,1)}}\right],$$
(9)

where P_i^R is the received primary GW signal by probe i at location $z = L$. Thus, following Eqs. (7) and (8), the optimized index for localizing and evaluating a local microdamage in thin-walled pipe-like structures can be obtained. Since the nonlinear signals of S_i^R and S_i^{R0} are orders of magnitude lower than the primary wave P_i^R, and the magnitude of QSC signal is mostly linear proportional to the microdamage degree as investigated in Section 3, the proposed method based on signal correlation can be used for quantitatively assessing the microdamage in addition to the localization.

5. Experiment

5.1. Specimens & micro-corrosion implementation

To verify the effectiveness of the proposed microdamage localization method, we conduct experiments in 6061 aluminum pipes. The four pipe specimens used in the experiments are of the same outer and inner radii as in the FE simulations ($a = 17.5$mm, $b = 19$mm). The lengths are 1.5 m. One pipe was left intact (#0), and the others were artificially damaged.

The damage implementation process for the specimens involved a systematic procedure to induce artificial early-stage corrosion in local areas. Firstly, we used the Keller reagent ($1HF + 1.5HCl + 2.5HNO_3 + 95H_2O$) on the designed surface areas of the specimens (See Table 4) for 30 s as preprocessing [34]. There are three corrosion specimens. The corrosion of the specimens was carried out in a fume hood with double-sided sponge tape applied to the surface of the specimen to form a square groove preventing the spreading of the corrosion solution. Then, we added concentrated hydrochloric acid to the respective areas of two pipes for 30 s (#1), and 60 s (#2) to generate corrosion-related micro-defects of different degrees. The same corrosion process by hydrochloric acid was applied to pipe #3 for 60 s as well, but the implementation was at a different location.

It should be noted that the induced micro-defects did not form into a uniform thickness reduction of the specimen as a complete faceted crater. The leaching of the chemical process formed a small primary cell between the grain and the grain boundary, and due to the potential difference, the grain boundary corroded first. The different degrees of corrosion of grain boundaries and grains resulted in the formation of small corrosion pits on and near the surface of the specimens, thus leading to heterogeneity in the microstructure of the corrosion areas [32]. At the end of the etching time, the surface of the specimen was washed with water and blown dry, and any residual sponge was removed with an organic solvent.

5.2. Experimental setup & measurement

The measuring process was performed using the experimental setup shown in Fig. 11. The excitation tone-burst signal was generated by a NI signal generation module (Model: PXIe-5122), then amplified by a high-power amplifier (Model: CIPRIAN HVA-800A). A load resistance 50 Ω was used for impedance matching. An oscilloscope was used to observe the input signal. Eight rectangular PZTs (Meggitt Ceramics, dimensions: 5.0 mm × 6.0 mm × 1.0 mm) were attached around the left end outer surface using conductive epoxy (Chemtronics CW2400) for the wave generation in the pipe. The propagating tone-burst wave in the pipe was then measured using a 3D laser Doppler scanning vibrometer (LDV) and acquisition system (Model: Polytech PSV-400). The OFV-5000 vibrometer controller combined with the DD-900 displacement decoder provides a minimum 0.5 pm resolution and maximum ±50 mm displacement ranging from 0 Hz to 5 MHz [35]. The measurement area was painted with a reflective coating (CRC 18015) for improving the magnitude of reflected laser signals.

The tone-burst signal generated by the NI system is 15-cycle sine wave of 200 kHz, and is amplified by the CIPRIAN with 150 V peak-to-peak voltage. Afterwards, the amplified high-voltage signal was sent to the attached PZT actuators. For generating the expected L(0,1) mode wave, the polarized main displacement direction of the PZTs is in the thickness direction, as the radian displacement of L(0,1) mode is larger than the other direction displacements according to the theoretical wave structure shown in Fig. 3(a). For signal receiving, the 3D laser measurement system was set up and calibrated. The recorded signals were averaged 1500 times to improve the signal-to-noise ratio. The sampling frequency of acquisition was set as 2.56 MHz with 390.6 ns sampling resolution, and a low-pass filter was applied with an upper limit of 600 kHz. Each measuring process was repeated three times to determine the uncertainty of the experimental results.

5.3. Results & discussion

5.3.1. Verification of primary wave mode

Firstly, the primary L(0,1) mode wave is verified by checking the group velocity calculated from time domain signals. As shown in Fig. 12 (a), the wave packets extracted in the radius r direction (out-of-plane displacement) received by the 3D laser acquisition system scanning at different locations (Z = 0.55 m, 0.75 m, 0.95 m) are obtained. Due to imperfect excitation conditions, multiple wave packets are picked up. It is also observed that the first wave packet is slightly dispersive during the propagation such that its packet length is increasing while the amplitude is decreasing. This is in line with the theoretical dispersion curve of L(0,1) mode at 200 kHz (See Fig. 2). Besides, by time–frequency domain analysis, Fig. 12(b) shows the Short Time Fourier Transform (STFT) results of the three temporal signals. The main frequency of these three signals is confirmed as 200 kHz in the power spectrum plots. The group velocity of the first wave packet is calculated as about 2510 m/s using the time-of-flight method. Due to less than 1 % error compared to the theoretical value, the primary L(0,1) mode is confirmed. Moreover, there barely exists the faster L(0,2) mode in the received signals, which facilitates the following analyses of the nonlinear QSC pulse signals. In addition, it is found that the group velocities measured from the four pipes are almost identical (relative errors are within 1 %.). This indicates that the corrosion zone scarcely has effect on the wave velocity of fundamental L(0,1) GW, and such linear ultrasonic characteristic cannot detect the early damage.

5.3.2. Observation of QSC generation

Secondly, to observe the secondary wave field, the phase-reversal method conducted for the FE simulation was also applied in the experiments to counteract the primary waves and double the magnitude of the nonlinear waves. Specifically, based on the numerical results in Section 3, the QSC pulse vibration is confirmed to be in-plane displacement polarized in the axial Z direction. Thus, we focus on the signal processing of axial displacement components obtained by the 3D laser system. Typical received time-domain signals in the intact and corrosion pipes
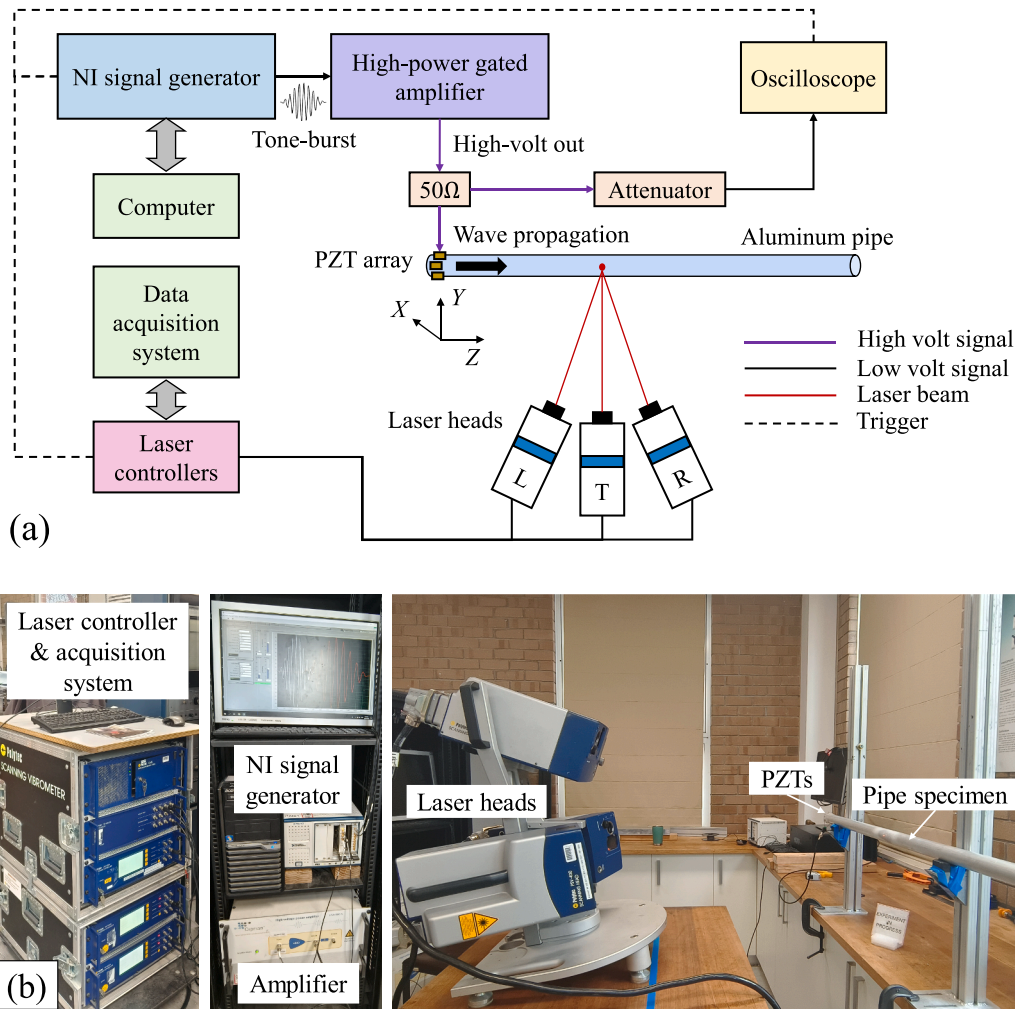
Table 4
Corrosion damage processing areas and times in 6061 aluminum pipes.

Pipe	Z_1 (m)	d (m)	$\alpha(°)$	Processing time (s)
#0	NA	NA	NA	0
#1	0.3	0.05	180	30
#2	0.3	0.05	180	60
#3	0.65	0.05	180	60

Fig. 11. Experimental setup: (a) measurement system diagram, (b) physical pictures of key parts.

after applying the phase-reversal processing and low-pass filtering are shown in Fig. 13(a). It is found that the nonlinear signals contain both the global material nonlinearity-induced QSC and the local corrosion-induced QSC. The former is received by the laser system (picking point: $z = 1.0$m) at around 2.0×10^{-4}s for all four pipes. This is in accordance with the theoretical prediction. It is noted that the post-processed QSC signals induced by the global weak material nonlinearity shows low SNR considering the noisy vibrations at the ending parts of the temporal signals. This is because the global QSC signals are not cumulative due to group velocity mismatch, and their wave energies are not converged on the amplitudes at certain time sections. However, the QSC signal induced by a local microdamage can have a large amplitude such as that measured in specimens #2 and #3. Besides, since the QSC signals always propagate at the largest group velocity and do not suffer significant divergence like in plates, this local damage-induced QSC pulse can be recognized.

For the corrosion induced QSC, the local DC vibration at around 3.2×10^{-4}s is not obvious for pipe #1, which suffered the artificial corrosion processing for only 30 s. However, there exists a significant DC displacement around 3.2×10^{-4}s and 3.8×10^{-4}s for pipe #2 and pipe #3, respectively. This is mainly due to that the 60 s artificial corrosion process has resulted in many micro-corrosion pits in the two pipes. While the primary L(0,1) GW propagates through the corrosion areas, the fundamental GW power partly flows to the QSC pulse signal due to all types of nonlinear response to the microstructural changes. Furthermore, by time–frequency analysis, Fig. 13(b) shows the power

spectra of the nonlinear signals in dB scale. The main frequencies of these signals are near zero, and the local damages in #1, #2, and #3 lead to three power peaks in the spectra. The time-of-flight for local DC displacements caused by the three local corrosion damages can be extracted and used for centre damage location estimation by a set of equations

$$
\begin{aligned}
c_g^{L(0,1)} \cdot t_1 + c_g^{SC} \cdot t_2 &= L + W, \\
t_1 + t_2 &= TOF, \\
Z_c &= c_g^{L(0,1)} \cdot t_1,
\end{aligned}
\tag{10}
$$

where *TOF* denotes the arrival time of the power peak in the time–frequency spectrum and Z_c is the estimated centre location of the local damage.

Moreover, by applying the proposed microdamage localization method described in Section 4, the results are shown in Fig. 14. The laser measuring points are evenly distributed at 8 locations along the circumference of the specimen. The discretising resolution of the pipe surface is 1 mm × 1 mm. The resulting graphs are plotted using the same axes and colour ranges. For specimen #0, the microdamage index is reasonable since no early corrosion damage has been made. For pipe #1, the local DC displacement pulse caused by the corrosion damage is not obvious such that the localization result is not accurate in terms of both the damage size and the centre location of the damage. For pipes #2 and #3, the localization results are promising regarding the longitudinal resolution in the axial *Z* direction. It is noted that the proposed method
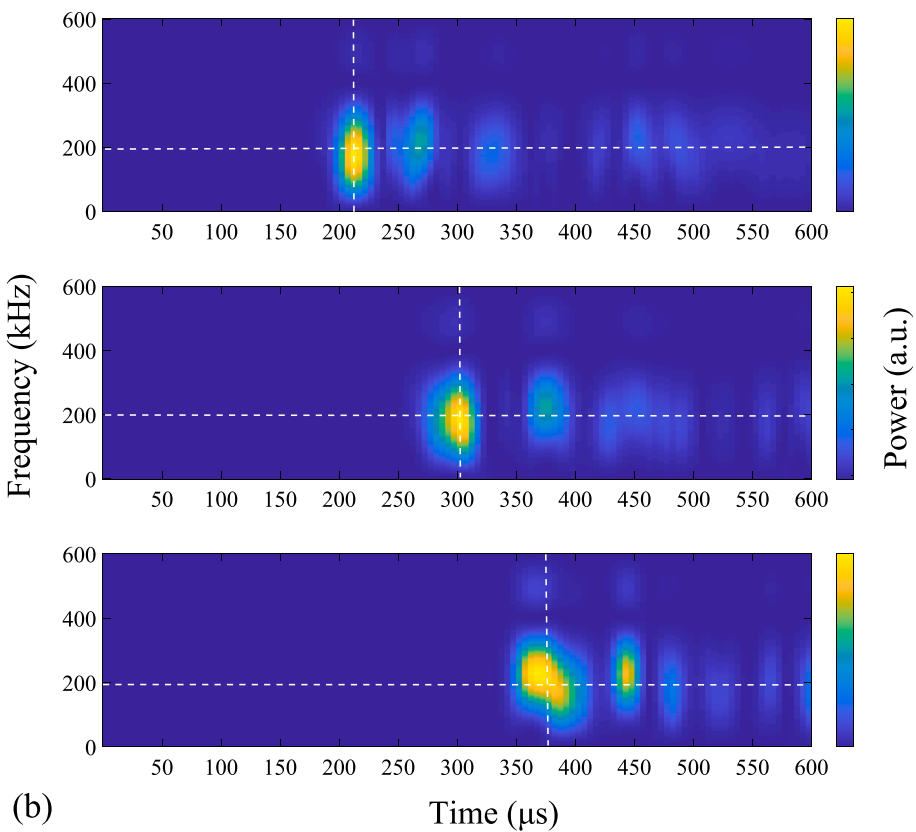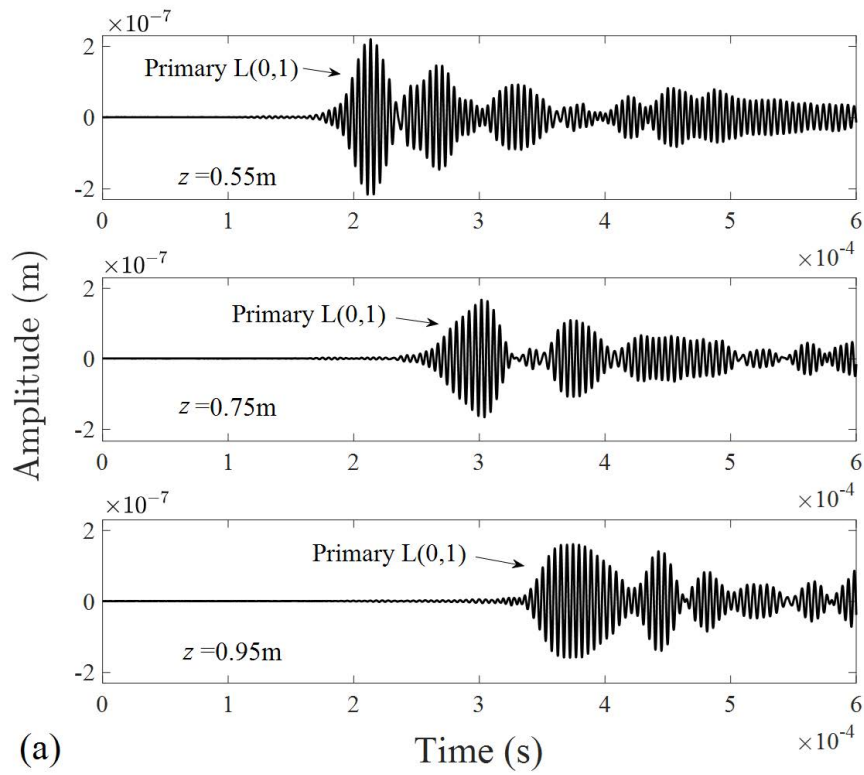
Fig. 12. (a) Typical time domain signals of primary waves and (b) corresponding time–frequency domain analysis.

did not perform an accurate assessment of the damage location in the circumferential direction of the pipe. This is because the aluminum specimens in this experiment are of relatively small radius, and the path length difference of GW propagation by the circumferential receiving

points at $z = 1.0$ m is negligible. However, the localization in the z direction for thin-walled cylindrical structures of small radius is satisfactory, and the proposed method is compatible with structures of large radius and length. Also, although the 8 measuring points did not
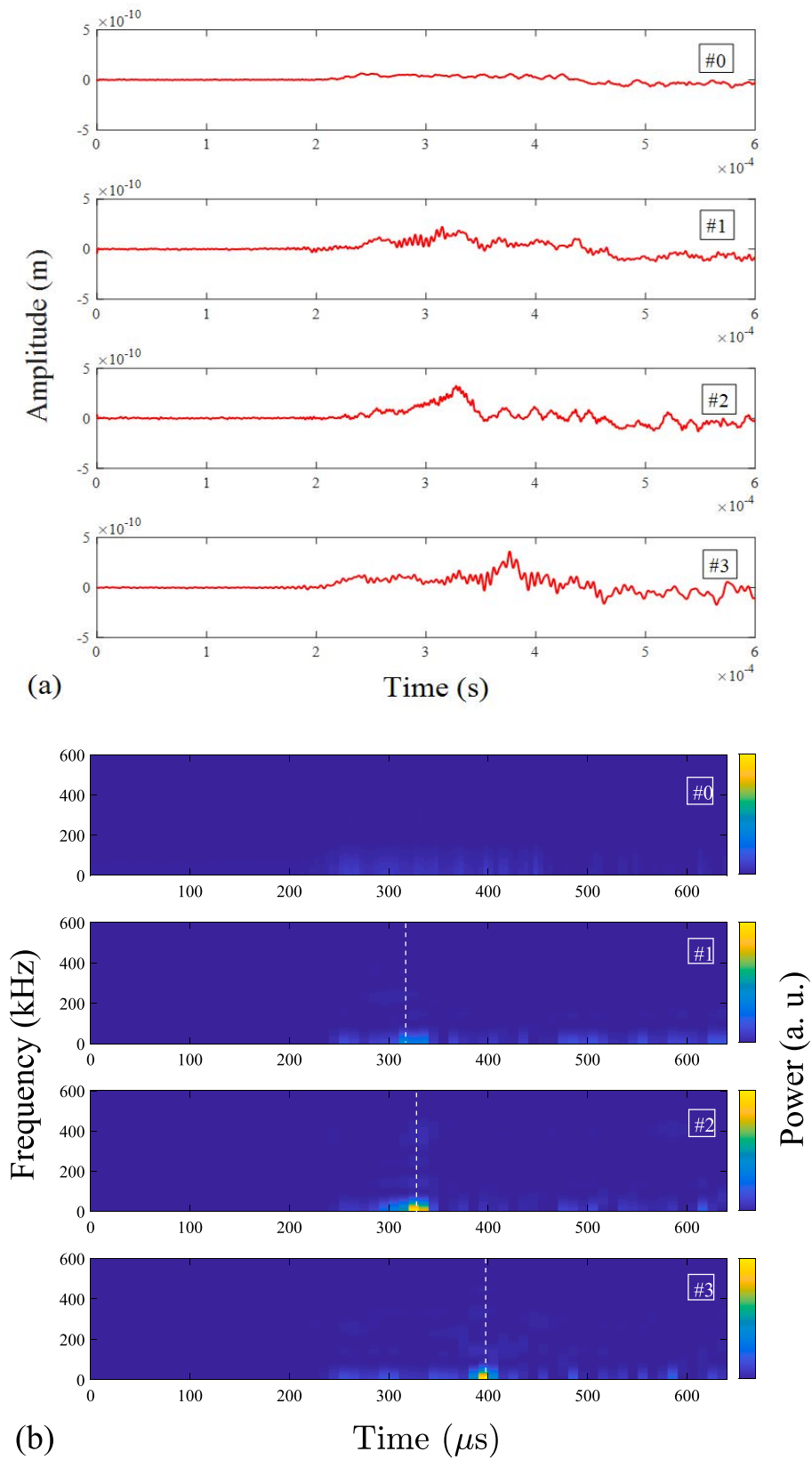
Fig. 13. (a) Time domain signals and (b) corresponding time–frequency domain analysis of QSC signals after phase-reversal processing.
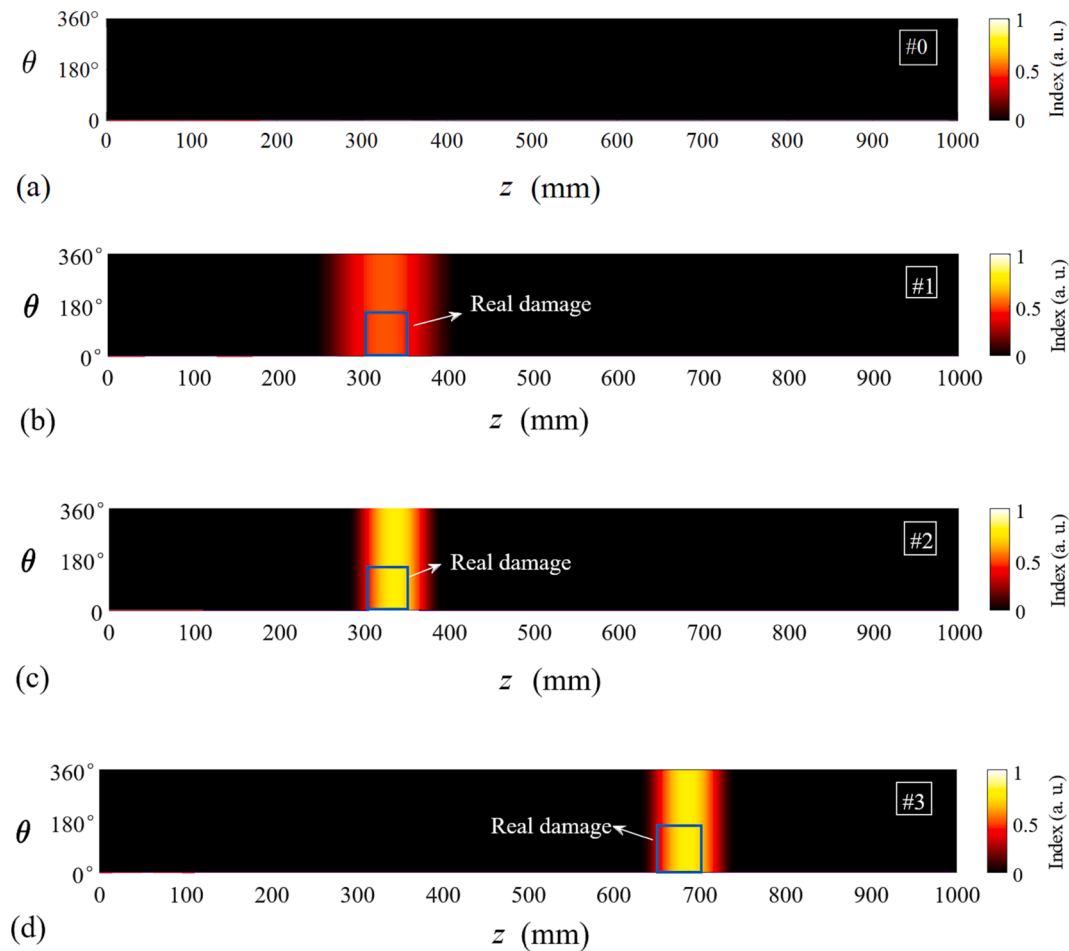
Fig. 14. Microdamage localization results for aluminum specimens: (a) #0 pipe, (b) #1 pipe, (c) #2 pipe, (d) #3 pipe.

contribute to the circumferential resolution of the localization result, the value of i in the proposed technique still plays an important role in enhancing the SNR of the nonlinear signal considering the random measurement errors.

6. Conclusion

In this paper, the QSC generation from the propagation of guided waves in isotropic metallic hollow cylindrical structures has been investigated. The wave mode, waveform, generation efficiency, along with the cumulative effect of the generated QSCs by different primary guided wave modes, have been numerically studied. The QSC pulse signals have been confirmed as zero-frequency L(0,1) mode with an only uniform axial displacement, and the group velocity mismatch condition has been found as the factor that influences the pulse width increase of the QSC signal. Besides, based on the analysis of numerical results, a local micro-damage localization method involving only a single one-way primary wave propagation has been proposed. The method has been validated by experiments using L(0,1)-QSC mode pair with group velocity mismatch, 3D laser vibrometer, and early corrosion damaged aluminum specimens. The experimental results show there is good agreement with the numerical results, and indicate promising applications of the method in early-stage microdamage detection, localization, and monitoring for metallic structures.

CRediT authorship contribution statement

Chang Jiang: Conceptualization, Data curation, Formal analysis, Methodology, Writing – original draft. **Weibin Li:** Funding acquisition, Supervision, Writing – review & editing. **Ching-Tai Ng:** Resources, Supervision, Writing – review & editing. **Mingxi Deng:** Supervision, Writing – review & editing.

Declaration of competing interest

The authors declare that they have no known competing financial interests or personal relationships that could have appeared to influence the work reported in this paper.

Data availability

Data will be made available on request.

References

[1] Pieczonka L, Klepka A, Martowicz A, Staszewski W. Nonlinear vibroacoustic wave modulations for structural damage detection: an overview. Opt Eng 2015;55: 011005. https://doi.org/10.1117/1.OE.55.1.011005.

[2] Li W, Hu S, Deng M. Combination of phase matching and phase-reversal approaches for thermal damage assessment by second harmonic Lamb waves. Materials 2018;11:30322066. https://doi.org/10.3390/ma11101961.

[3] Zhang M, Xiao L, Qu W, Lu Y. Damage detection of fatigue cracks under nonlinear boundary condition using subharmonic resonance. Ultrasonics 2017;77:152–9. https://doi.org/10.1016/j.ultras.2017.02.001.

[4] Li W, Deng M, Hu N, Xiang Y. Theoretical analysis and experimental observation of frequency mixing response of ultrasonic Lamb waves. J Appl Phys 2018;124: 044901. https://doi.org/10.1063/1.5028536.

[5] Sun M, Xiang Y, Deng M, Xu J, Xuan F. Scanning non-collinear wave mixing for nonlinear ultrasonic detection and localization of plasticity. NDT and E Int 2018; 93:1–6. https://doi.org/10.1016/j.ndteint.2017.09.010.

[6] Zhu W, Xiang Y, Liu C, Deng M, Xuan F. Symmetry properties of second harmonics generated by antisymmetric Lamb waves. J Appl Phys 2018;123:104902. https://doi.org/10.1063/1.5010058.

[7] Yang Y, Ng CT, Kotousov A. Bolted joint integrity monitoring with second harmonic generated by guided waves. Struct Health Monitor Internat J 2019;18: 193–204. https://doi.org/10.1177/1475921718814399.

[8] J Chen, T Yin, JY Kim, Z Xu, Y Yao. Characterization of thermal damage in sandstone using the second harmonic generation of standing waves. 2017; 91:81-89. https://doi.org/10.1016/j.ijrmms.2016.11.014.

[9] H Cho, M Hasanian, S Shan, CJ Lissenden. Nonlinear guided wave technique for localized damage detection in plates with surface-bonded sensors to receive Lamb waves generated by shear-horizontal wave mixing. 2019; 102: 35-46. https://doi.org/10.1016/j.ndteint.2018.10.011.

[10] Zhu H, Ng CT, Kotousov A. Frequency selection and time shifting for maximizing the performance of low-frequency guided wave mixing. NDT and E Int 2023;133: 102735. https://doi.org/10.1016/j.ndteint.2022.102735.

[11] Hasanian M, Lissenden CJ. Second order harmonic guided wave mutual interactions in plate: Vector analysis, numerical simulation, and experimental results. J Appl Phys 2017;122:084901. https://doi.org/10.1063/1.4993924.

[12] Deng M. Second-harmonic generation of ultrasonic guided wave propagation in an anisotropic solid plate. Appl Phys Lett 2008;92:111910. https://doi.org/10.1063/1.2899938.

[13] Thurston RN, Shapiro MJ. Interpretation of Ultrasonic Experiments on Finite-Amplitude Waves. J Acoust Soc Am 1967;41:1112. https://doi.org/10.1121/1.1910443.

[14] Cantrell JH. Acoustic-radiation stress in solids. I Theory Physical Review B 1984; 30:3214. https://doi.org/10.1103/PhysRevB.30.3214.

[15] Nagy PB, Qu J, Jacobs LJ. Finite-size effects on the quasistatic displacement pulse in a solid specimen with quadratic nonlinearity. J Acoust Soc Am 2013;134: 1760–74. https://doi.org/10.1121/1.4817840.

[16] Jacob X, Takatsu R, Barrière C, Royer D. Experimental study of the acoustic radiation strain in solids. Appl Phys Lett 2006;88:134111. https://doi.org/10.1063/1.2191428.

[17] Narasimha KT, Kannan E, Balasubramaniam K. Simplified experimental technique to extract the acoustic radiation induced static strain in solids. Appl Phys Lett 2007; 91:134103. https://doi.org/10.1063/1.2793181.

[18] Deng M. An experimental approach for detection of the acoustic radiation induced static component in Solids. Chin Phys Lett 2020;37:074301. https://doi.org/10.1088/0256-307x/37/7/074301.

[19] Wan X, Tse PW, Zhang X, Xu G, Zhang Q, Fan H, et al. Numerical study on static component generation from the primary Lamb waves propagating in a plate with nonlinearity. Smart Mater Struct 2018;27:045006. https://doi.org/10.1088/1361-665X/aaafeb.

[20] Sun X, Shui G, Zhao Y, Liu W, Hu N, Deng M. Evaluation of early stage local plastic damage induced by bending using quasi-static component of Lamb waves. NDT and E Int 2020;116:102332. https://doi.org/10.1016/j.ndteint.2020.102332.

[21] Gao G, Chen H, Hu N, Deng M. Experimental observation of static component generation by Lamb wave propagation in an elastic plate. Ultrasonics 2021;117: 106537. https://doi.org/10.1016/j.ultras.2021.106537.

[22] Jiang C, Li W, Deng M, Ng CT. Static component generation and measurement of nonlinear guided waves with group velocity mismatch. JASA Express Letters 2021; 1:055601. https://doi.org/10.1121/10.0004847.

[23] Jiang C, Li W, Deng M, Ng CT. Quasistatic pulse generation of ultrasonic guided waves propagation in composites. J Sound Vib 2022;524:116764. https://doi.org/10.1016/j.jsv.2022.116764.

[24] Jiang C, Zhang C, Li W, Deng M, Ng CT. Assessment of damage in composites using static component generation of ultrasonic guided waves. Smart Mater Struct 2022; 31:045025. https://doi.org/10.1088/1361-665X/ac5a77.

[25] Rose JL. Ultrasonic guided waves in solid media. Cambridge University Press; 2014.

[26] Zhang SY, Li CM, Ye WJ. Damage localization in plate-like structures using time-varying feature and one-dimensional convolutional neural network. Mech Syst Sig Process 2021;147:15. https://doi.org/10.1016/j.ymssp.2020.107107.

[27] Cantero-Chinchilla S, Chiachío J, Chiachío M, Chronopoulos D, Jones A. A robust Bayesian methodology for damage localization in plate-like structures using ultrasonic guided-waves. Mech Syst Sig Process 2019;122:192–205. https://doi.org/10.1016/j.ymssp.2018.12.021.

[28] Marcantonio V, Monarca D, Colantoni A. Ultrasonic waves for materials evaluation in fatigue, thermal and corrosion damage: A review. Mech Syst Sig Process 2018; 120:32–42. https://doi.org/10.1016/j.ymssp.2018.10.012.

[29] Li W, Deng M, Xiang Y. Review on second-harmonic generation of ultrasonic guided waves in solid media (I): Theoretical analyses. Chin Phys B 2017;26: 114302. https://doi.org/10.1088/1674-1056/26/11/114302.

[30] M Lowe. Disperse: Guided wave dispersion curve calculation. www.disperse.software.

[31] Wu J, Jiang C, Fang H, Ng CT. Damage detection in the T-welded joint using Rayleigh-like feature guided wave. NDT and E Int 2023;135:102806. https://doi.org/10.1016/j.ndteint.2023.102806.

[32] Davis JR. Corrosion of aluminum and aluminum alloys. ASM Internat 1999.

[33] Dassault Systeme SIMULIA. Abaqus/CAE user's manual. www.3ds.com.

[34] ASTM E407-07 Standard practice for microetching metals and alloys, ASTM International, 2016. www.astm.org.

[35] Polytec GmbH. OFV-5000 vibrometer controller datasheet. www.polytec.com.

Chapter 7: Numerical and Experimental Investigations on Quasistatic Pulse Generation of Ultrasonic Guided Waves in Fiber Reinforced Composite Pipes

7.1. Introduction, Significance, and Commentary

This study investigates the QSC generation in anisotropic composite pipes. Different primary guided waves are employed and the results of QSC generation are compared. By use of semi-analytical finite element method and time-domain simulation of wave propagation, the QSC generation in fiber reinforced composite pipes is studied regarding the mode type, propagation feature, and generation efficiency. Moreover, experimental investigation is conducted for measuring the nonlinear QSC pulse signals and use it for early-stage thermal fatigue microdamage evaluation. The numerical perspectives provide comprehensive understandings on the QSC generation in composite pipes, and the experiment showed good agreement with the theoretical predictions, paving the way for more future NDT applications based on the special nonlinear ultrasonic phenomena of QSC.

7.2. Publication

This section is presented as published research paper by **Chang Jiang**, Weibin Li, Ching-Tai Ng, Mingxi Deng (2024) Numerical and experimental investigations on quasistatic pulse generation of ultrasonic guided waves in fiber reinforced composite pipes, *Journal of Sound and Vibration*.

Statement of Authorship

Title of Paper	Numerical and experimental investigations on quasistatic pulse generation of ultrasonic guided waves in fiber reinforced composite pipes
Publication Status	☑ Published ☐ Accepted for Publication ☐ Submitted for Publication ☐ Unpublished and Unsubmitted work written in manuscript style
Publication Details	Chang Jiang, Weibin Li, Ching-Tai Ng, et al. (2024) Numerical and experimental investigations on quasistatic pulse generation of ultrasonic guided waves in fiber reinforced composite pipes, Journal of Sound and Vibration.

Principal Author

Name of Principal Author (Candidate)	Chang Jiang		
Contribution to the Paper	Conceptualization, Methodology, Investigation, Data curation, Visualization, Writing - Original Draft		
Overall percentage (%)	80		
Certification:	This paper reports on original research I conducted during the period of my Higher Degree by Research candidature and is not subject to any obligations or contractual agreements with a third party that would constrain its inclusion in this thesis. I am the primary author of this paper.		
Signature		Date	2023.12.29

Co-Author Contributions

By signing the Statement of Authorship, each author certifies that:

i. the candidate's stated contribution to the publication is accurate (as detailed above);

ii. permission is granted for the candidate in include the publication in the thesis; and

iii. the sum of all co-author contributions is equal to 100% less the candidate's stated contribution.

Name of Co-Author	Weibin Li		
Contribution to the Paper	Resources, Writing - Review & Editing, Supervision, Funding acquisition		
Signature		Date	2023.12.29
Name of Co-Author	Ching-Tai Ng		
Contribution to the Paper	Resources, Writing - Review & Editing, Supervision		
Signature		Date	2023.12.29
Name of Co-Author	Mingxi Deng		
Contribution to the Paper	Writing - Review & Editing, Supervision		
Signature		Date	2023.12.29

Please cut and paste additional co-author panels here as required.

Numerical and experimental investigations on quasistatic pulse generation of ultrasonic guided waves in fiber reinforced composite pipes

Chang Jiang [a,b], Weibin Li [b,*], Ching-Tai Ng [a,*], Mingxi Deng [c,*]

[a] School of Architecture & Civil Engineering, University of Adelaide, Adelaide, South Australia, 5005, Australia
[b] School of Aerospace Engineering, Xiamen University, Xiamen, Fujian, 361000, PR China
[c] College of Aerospace Engineering, Chongqing University, Chongqing, 400010, PR China

ARTICLE INFO

ABSTRACT

The quasistatic pulse (QSP) generation of ultrasonic guided waves in composite pipes can exhibit many features that are useful for early-stage material characterization and structural health monitoring. The intrinsic relationship between the QSP generation and the weak elastic nonlinearity of solids is complex. It has yet promised for developing the nonlinear ultrasonic guided wave technique that combines its advantages of high sensitivity to microdamage and low ultrasonic attenuation in composite materials. This study presents a systematic investigation of the QSP generation in fiber reinforced composite pipes. Using a three-dimensional finite element simulation with a nonlinear material model, the temporal waveform, mode conversion effect, cumulative effect, generation efficiency, and duration effect of QSP generation are revealed. The nonlinear QSP signals in laminated composite pipes are confirmed as the fastest wave mode that only has axial displacement. The shape of QSP depends on the group velocity difference between the QSP and the primary wave. The magnitude of QSP is related to the excitation level, frequency, and tone-burst duration of the primary wave. Experiments are conducted using carbon fiber reinforced composite pipes and the signals are measured using a laser vibrometer scanning system for verifying the QSP generation. The experimental results are consistent with the numerical findings. A relative nonlinear acoustic parameter based on the QSP generation is proposed and used to evaluate the early-stage thermal fatigue damage in the pipes. The measured nonlinear acoustic parameter demonstrates high sensitivity to the damage, indicating considerable potential for industrial applications.

1. Introduction

Due to corrosion resistance, lightweight nature, high strength-to-weight ratio, durability, and design flexibility, fiber reinforced polymer (FRP) composites have gained significant interest in various industrial applications [1]. Detecting damage in composites is crucial for ensuring structural integrity in aerospace, automotive, construction, and other fields [2]. Ultrasonic techniques, specifically guided wave (GW) methods [3–5] combined with nonlinear acoustic approaches [6,7], offer advantages such as high sensitivity, deep penetration, portability, and real-time imaging. These methods enhance ultrasound's sensitivity to smaller defects compared to the

wavelength, while reducing inspection costs for large structures. In industries like pipelines and storage containers, nonlinear ultrasound-based structural health monitoring (SHM) techniques play a more vital role in providing early-stage damage information than conventional nondestructive techniques.

Recent advances in the research and application of nonlinear GW (NGW) mostly involve the measurement of higher harmonic generation [7–9]. However, for detecting material nonlinearity-related damages, higher harmonic generation normally requires satisfaction of synchronism and non-zero power flux conditions [10,11]. The cumulative effect, by which the magnitude of the higher harmonic grows with the propagation distance, benefits the measurement of nonlinear signals. Li et al. [12] used the phase velocity and group velocity matched mode pair for evaluating thermal fatigue damage in metallic pipes. Another study [13] on the nonlinear response of early damage in the inner layer of a composite metallic tube by circumferential GW also involved strict mode selection for achieving cumulative second harmonic generation. However, the appropriate selection of suitable mode pairs usually requires advanced knowledge of dispersion features and vibrational characteristics of GWs. Owing to the complex mechanical properties and damage mechanisms of FRP composites, the process of wave mode selection requires significant effort. A similar situation is encountered when applying GW mixing technique [11,14,15]. Considering the wavelength and mode shape of the GW to be excited, the number of available mode pairs for assessing material nonlinearity-related microdamage is often limited. Apart from the complex dispersion features of GW and damage mechanism in anisotropic composite pipe-like structures, ultrasound attenuation is also one of the key factors in developing a suitable NGW technique. Due to the known exponential attenuation characteristic of ultrasound with respect to frequency (especially strong attenuation effect in composites), the advantage of long propagation distance of GWs is still limited when using higher harmonic generation.

An important aspect of nonlinear ultrasound that has not been studied widely is the generation of the quasistatic pulse (QSP) response of tone-burst GWs. The study on the quasistatic response of GWs origins from the research on acoustic static strain (i.e., DC response) by plane longitudinal waves [16–19]. In the context of classical nonlinear stress-strain relation, the temporal shape of QSP by finite-size longitudinal wave has been confirmed as the envelop-like shape of the fundamental wave, which can also be influenced by boundary conditions. Due to zero frequency of the carrier wave, the QSP generated from ultrasound propagation is traditionally neglected by signal filtering. There has been literature [20,21] reporting the QSP generation of GWs in both isotropic metallic and anisotropic composite materials by numerical studies. The mode of QSP generated by different primary GWs in thin plates has been verified as S0 mode at near-zero frequency with only in-plane displacement. However, as one of the nonlinear responses, the QSP signal usually propagates along the plate with large energy divergence (i.e., the induced QSP has poor directivity due to low frequency). This indicates that ultrasound excitations with large amplitude and higher frequency are desired for effective signal-to-noise ratio (SNR) of practical QSP applications in plate structures. For hollow cylinders, there exists a scarce amount of documentation regarding the QSP generation in pipe structures. In view of the closed cross-sections of tubular waveguides, it is expected that the QSP in pipes has much less energy dissipation than that in plates. An additional advantage of QSP generation is the zero frequency of its carrier wave that can contribute to neglectable acoustic attenuation and a much longer propagation distance than higher harmonics. Furthermore, the QSP as nonlinear signal is typically independent of instrumental nonlinearity and can be detected by either low-frequency transducers or laser vibrometers. Previous studies [22,23] on early damage detection in polymer materials with great ultrasonic attenuation using QSP generation of bulk waves and Lamb waves has shown the high sensitivity of QSP to microscale thermal damage and low velocity impact damage. Thus, the potential of applying QSP generation for the assessment of material nonlinearity and local damages in composite pipes is promising.

The objective of this study is to investigate the generation of QSP in anisotropic FRP composite pipes and further verify the applicability of using QSP of GW for assessing material nonlinearity-related damage in FRP composite pipes. A systematic study on the QSP generation mechanism and propagation characteristics in composite pipes is conducted. To gain insights into the QSP generation in complex FRP pipes, numerical analyses of dispersion characteristics and wave structures of GWs in FRP composite pipes are performed first using the semi-analytical finite element (SAFE) method [24,25] with efficient and accurate frequency-domain numerical results. Moreover, a three-dimensional (3D) finite element (FE) model is developed considering the material nonlinearity of anisotropic materials. The temporal shape, mode conversion effect, cumulative effect, and generation efficiency of QSP by GWs in composite pipes are investigated. For regional microscale damage in composite pipes, a simplified material model with microdamage is represented by variations of third-order elastic constants (TOECs) and incorporated in the time-domain 3D FE analysis. The proposed microdamage assessment method based on the measure of QSP is then discussed and compared with the experimental results measured in thermal fatigue damaged carbon fiber reinforced polymer (CFRP) pipes.

The paper is structured as follows. Section 2 describes the theoretical generation mechanism of QSP by longitudinal and transverse waves in anisotropic materials with weak quadratic material nonlinearity. In Section 3, a CFRP layered pipe is numerically analyzed regarding the dispersion and mode shape of GWs using the SAFE method. The time-domain 3D FE model for analyzing NGW propagation is also described. Section 4 shows the FE results and discusses the features of QSP in composite pipes. In Section 5, experiments are carried out using CFRP pipes, piezoelectric transducer array, and 3D laser vibrometer system. The results are analyzed and compared with FE data. Conclusions are drawn in Section 6.

2. Mechanism of quasistatic pulse generation

In general, FRP materials have polymer as a matrix and fiber as a strengthening substance. They are widely produced by stacking multiple layers to achieve the desired mechanical properties. A single layer, which consists of unidirectional fiber, can be regarded as transversely isotropic material. From a theoretical point of view, the material nonlinearity of such unidirectional FRP material can be expressed by the strain energy function that includes the strain terms up to third order as reported in [21,26]:

$$
\begin{aligned}
W = &\ \alpha_1 (tr\mathbf{E})^2 + \alpha_2 (tr\mathbf{E})(\mathbf{a} \cdot \mathbf{Ea}) + \alpha_3 (tr\mathbf{E}^2) + \alpha_4 (\mathbf{a} \cdot \mathbf{Ea})^2 + \alpha_5 (\mathbf{a} \cdot \mathbf{E}^2 \mathbf{a}) \\
&+ \beta_1 (tr\mathbf{E})^3 + \beta_2 (tr\mathbf{E})(tr\mathbf{E}^2) + \beta_3 (tr\mathbf{E})(\mathbf{a} \cdot \mathbf{Ea})^2 \\
&+ \beta_4 (tr\mathbf{E})(\mathbf{a} \cdot \mathbf{E}^2 \mathbf{a}) + \beta_5 (tr\mathbf{E})^2 (\mathbf{a} \cdot \mathbf{Ea}) + \beta_6 (tr\mathbf{E}^2)(\mathbf{a} \cdot \mathbf{Ea}) \\
&+ \beta_7 (tr\mathbf{E}^3) + \beta_8 (\mathbf{a} \cdot \mathbf{Ea})^3 + \beta_9 (\mathbf{a} \cdot \mathbf{Ea})(\mathbf{a} \cdot \mathbf{E}^2 \mathbf{a}) + O(\mathbf{E}^4),
\end{aligned} \tag{1}
$$

Where $\mathbf{E}$ is the strain tensor, $\alpha_1 \sim \alpha_5$ are the linear elastic coefficients, $\beta_1 \sim \beta_9$ are the nonlinear elastic coefficients, $\mathbf{a}$ is the fiber direction unit vector. Assuming a Cartesian coordinate system (x_1, x_2, x_3), the primary wave propagates along the x_1 direction. The second Piola-Kirchhoof stress $\mathbf{S}$ is expressed by $\mathbf{S} = \partial W / \partial \mathbf{E}$, and the first Piola-Kirchhoff stress tensor is expressed by $\mathbf{P}(\mathbf{H}) = (\mathbf{I} + \mathbf{H})\mathbf{S}(\mathbf{H})$, where $\mathbf{I}$ is the identity tensor, and $\mathbf{H}$ is the displacement gradient tensor. Based on the balance of linear momentum $\mathbf{Div}(\mathbf{P}(\mathbf{H})) = \rho \ddot{\mathbf{u}}$, we can obtain the following results from five independent representative cases:

(i) For longitudinal wave $\mathbf{u} = (u_1^L, 0, 0)$ propagating along the fiber direction $\mathbf{a} = (1, 0, 0)$, the nonlinear wave equation can be written as

$$
\rho \ddot{u}_1 - A \frac{\partial^2 u_1}{\partial x_1^2} = B \frac{\partial u_1}{\partial x_1} \frac{\partial^2 u_1}{\partial x_1^2}, \tag{2}
$$

where

$$
\begin{aligned}
A &= 2\alpha_1 + 2\alpha_2 + 2\alpha_3 + 2\alpha_4 + 2\alpha_5, \\
B &= 6\alpha_1 + 6\alpha_2 + 6\alpha_3 + 6\alpha_4 + 6\alpha_5 + 6\beta_1 + 3\beta_2 + 6\beta_3 + 4\beta_4 + 6\beta_5 + \frac{11}{2}\beta_6 + 6\beta_7 + 6\beta_8 + 6\beta_9.
\end{aligned} \tag{3}
$$

For $|BU^2 k^2 x_1 / A| \ll 1$ and assuming the linear wave field as $u_1^L = U \exp[j(kx - \omega t)]$ (U is the amplitude of primary wave, k is the wavenumber, and ω is the angular frequency), by using the perturbation technique, the solution to the Eq. (2) under the consistency condition [17] can be written as

$$
u_1 = U \sin\left[\omega\left(t - \frac{x_1}{c_L}\right)\right] - \frac{BU^2 \omega^2 \rho}{8A^2} x_1 - \frac{BU^2 \omega^2 \rho}{8A^2} x_1 \cos\left[2\omega\left(t - \frac{x_1}{c_L}\right)\right], \tag{4}
$$

where c_L is the longitudinal wave velocity and ρ is the mass density. Here we can find the term $-BU^2 \omega^2 \rho x_1 / 8A^2$ represents the static strain caused by material nonlinearity and polarized in the wave propagation x_1 direction. It is noted that the coefficient A in Eq. (2) is a combination of second order elastic constants, and B indicates a combination of both second order and third order elastic constants. In practical applications, tone-burst ultrasound is widely used, and the propagating static strain exhibits a finite temporal width, namely QSP. When the material nonlinearity increases, the coefficient B increases, and the generation efficiency of QSP increases accordingly.

(ii) For longitudinal wave $\mathbf{u} = (u_1^L, 0, 0)$ propagating perpendicular to the fiber direction $\mathbf{a} = (0, 1, 0)$ or $\mathbf{a} = (0, 0, 1)$, the equation of motion keeps the form of Eq. (2), while the coefficients in Eq. (3) are changed to:

$$
\begin{aligned}
A &= 2\alpha_1 + 2\alpha_3, \\
B &= 6\alpha_1 + 6\alpha_3 + 6\beta_1 + 3\beta_2 + 6\beta_7.
\end{aligned} \tag{5}
$$

Similarly, the QSP can be calculated by the second order perturbation method and expressed as:

$$
u_{QSP} = -\frac{BU^2 \omega^2 \rho}{8A^2} x_1. \tag{6}
$$

(iii) For shear wave $\mathbf{u} = (0, u_2^L, 0)$ propagating along the fiber direction $\mathbf{a} = (1, 0, 0)$, the linear part of wave field can be written as

$$
\rho \ddot{u}_2^L - A \frac{\partial^2 u_2^L}{\partial x_1^2} = 0, \tag{7}
$$

where $A = \alpha_3 + \alpha_5 / 2$. For the nonlinear part of the wave field, the nonlinear term of the wave equation exists in the x_1 direction and can be expressed as

$$
B \frac{\partial u_2^L}{\partial x_1} \frac{\partial^2 u_2^L}{\partial x_1^2} = \rho \ddot{u}_1, \tag{8}
$$

where

$$
B = 2\alpha_1 + 2\alpha_2 + 2\alpha_3 + 2\alpha_4 + 2\alpha_5 + \beta_2 + \frac{\beta_4}{2} + \beta_6 + \frac{3\beta_7}{2} + \frac{\beta_9}{2}. \tag{9}
$$

It should be noted that the nonlinear term can act as the second order bulk driving force, which eventually leads to the generation of a static displacement polarized in the wave propagation x_1 direction.

(iv) For shear wave $\mathbf{u} = (0, u_2^L, 0)$ propagating perpendicular to the fiber direction $\mathbf{a} = (0, 1, 0)$, the linear part of the wave field keeps the form of Eq. (7), and the coefficient A remains $A = \alpha_3 + \alpha_5 / 2$. For the nonlinear part of the wave field, the nonlinear term of

the wave equation exists in the x_1 direction and keeps the form of Eq. (8), while the coefficient B changes into

$$B = 2\alpha_1 + 2\alpha_3 + \beta_2 + \frac{\beta_4}{2} + \frac{3\beta_7}{2}. \tag{10}$$

(v) For shear wave $\mathbf{u} = (0, u_2^{\mathrm{L}}, 0)$ propagating perpendicular to the fiber direction $\mathbf{a} = (0,0,1)$, the linear part of wave field keeps the form of Eq. (7), while the coefficient A changes into $A = \alpha_3$. For the nonlinear part of the wave field, the nonlinear term of the wave equation exists in the x_1 direction and keeps the form of Eq. (8), while the coefficient B changes into

$$B = 2\alpha_1 + 2\alpha_3 + \beta_2 + \frac{3\beta_7}{2}. \tag{11}$$

It should be noted that there are three more cases, in which the combination of shear wave displacement direction and the fiber direction, results in the equivalent wave equations as in the case of (iii), (iv), and (v). Table 1 summarizes the above theoretical analysis. The significant feature of QSP is that its main displacement direction is always identical to the primary wave propagation direction. This feature remains true when it comes to GW propagation in anisotropic composites, as GW can be regarded as the superposition of a series of bulk waves. During the primary GW propagation, the QSPs generated by all the bulk wave components interfere with each other under the boundary conditions, and eventually form into one nonlinear signal with its displacement polarized in the propagation direction of the primary wave. Besides, the magnitude of QSP is partly dependent on the nonlinear elastic constants $\beta_1 \sim \beta_9$. With the increase of material nonlinearity, the magnitude of QSP increases as well. Moreover, the generation of QSP by material nonlinearity is independent of the synchronism condition and non-zero power flux condition as required by the cumulative generation of higher harmonics and wave mixing combined harmonics [20]. The inherent cumulative effect of QSP exhibits in the increases of amplitude when its group velocity matches the primary tone-burst wave and exhibits in the increases of temporal width when its group velocity is different from that of the primary tone-burst wave [20,21].

3. Numerical analysis

3.1. Determination of dispersion & mode shapes using SAFE method

Without loss of generality, in the subsequent numerical investigations, an analysis is conducted on a 2 mm thick CFRP pipe that comprises both circumferential and axial fibers. The inner radius of the composite pipe is 48 mm, and the outer radius is 50 mm. The CFRP pipe is constructed by stacking 10 layers of ply, as illustrated in Fig. 1. Due to the anisotropy of such material, the properties of GW propagation regarding the dispersion feature and mode shapes are calculated by the SAFE method [25]. The mechanical properties of a single unidirectional layer of the CFRP pipe and its mass density are listed in Table 2. The eigenvalue problem in the frequency domain is then solved by considering both the analytical expression along the waveguided and the FE discretization imposed on the section of the waveguide. Fig. 2 shows the phase velocity and group velocity dispersion curves. Fig. 3 shows the mode shapes (i.e., wave structures) of the three lowest order axisymmetric GW modes at 200 kHz propagating in the CFRP pipe. In Fig. 3, the black arrows indicate the displacement component in the cross-section plane (XY plane in Fig. 1), and the color maps indicate the displacement component in the Z direction (wave propagation direction). As shown in Fig. 3(b), the T(0,1) wave mode has only torsional displacement polarized in the XY plane. Comparing Fig. 3(a) and (c), the L(0,2) has greater Z-displacement than the L(0,1) wave mode. This characteristic of longitudinal modes is in line with the mode shapes of GWs in isotropic metallic pipes [27]. The GW modal

Table 1
QSP generation of ultrasonic waves with different configurations in transversely isotropic materials. The primary wave propagates along x_1 direction.

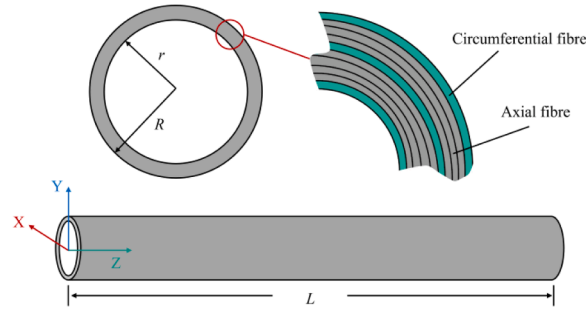| Configuration	(i)	(ii)	(iii)	(iv)	(v)
Displacement direction of primary wave / Fiber direction					
Displacement direction of QSP	Primary L wave propagation x_1 direction	Primary L wave propagation x_1 direction	Primary S wave propagation x_1 direction	Primary S wave propagation x_1 direction	Primary S wave propagation x_1 direction
$A\ (\rho c^2)$	$2\alpha_1 + 2\alpha_2 + 2\alpha_3 + 2\alpha_4 + 2\alpha_5$	$2\alpha_1 + 2\alpha_3$	$\alpha_3 + \alpha_5/2$	$\alpha_3 + \alpha_5/2$	α_3
B	$6\alpha_1 + 6\alpha_2 + 6\alpha_3 + 6\alpha_4 + 6\alpha_5$ $+ 6\beta_1 + 3\beta_2 + 6\beta_3 + 4\beta_4 + 6\beta_5$ $+ \frac{11}{2}\beta_6 + 6\beta_7 + 6\beta_8 + 6\beta_9$	$6\alpha_1 + 6\alpha_3 + 6\beta_1$ $+ 3\beta_2 + 6\beta_7$	$2\alpha_1 + 2\alpha_2 + 2\alpha_3 + 2\alpha_4 + 2\alpha_5$ $+ \beta_2 + \frac{\beta_4}{2} + \beta_6 + \frac{3\beta_7}{2} + \frac{\beta_9}{2}$	$2\alpha_1 + 2\alpha_3 + \beta_2 + \frac{\beta_4}{2} + \frac{3\beta_7}{2}$	$2\alpha_1 + 2\alpha_3 + \beta_2 + \frac{3\beta_7}{2}$

Fig. 1. Schematic of CFRP pipe with stacking order [C/A$_4$/C/A$_3$/C] (C: circumferential fiber, A: axial fiber), inner radius r = 48 mm, outer radius R = 50 mm.

Table 2
Second order stiffness constants (Unit: GPa) and mass density (kg/m^3) of a single CFPR layer used in numerical analysis.

C$_{11}$	C$_{12}$	C$_{13}$	C$_{22}$	C$_{23}$	C$_{33}$	C$_{44}$	C$_{55}$	C$_{66}$	Density
143.8	6.2	6.2	13.3	6.5	13.3	3.4	5.7	5.7	1560
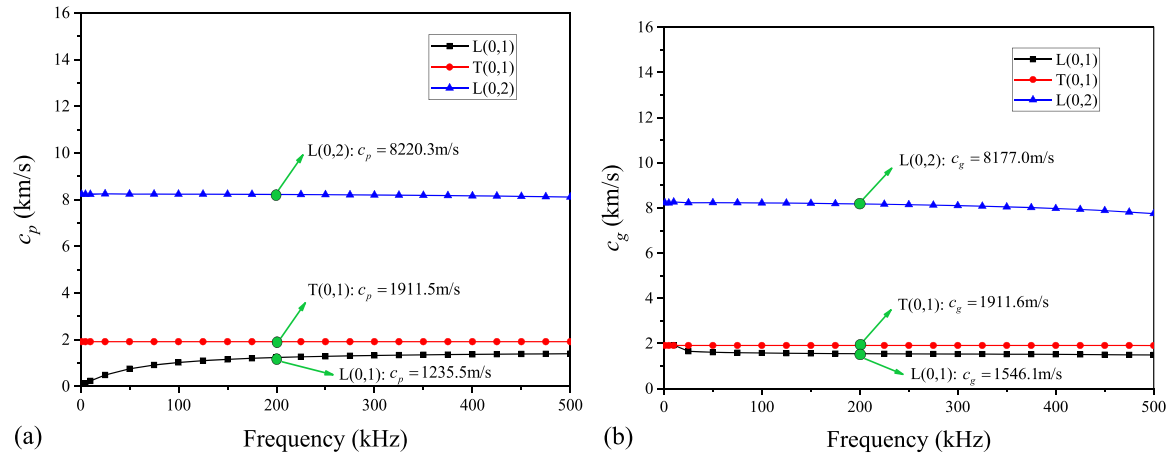
Fig. 2. Dispersion curves of GWs: (a) phase velocity, (b) group velocity.

analysis of such composite structure provides guidance for effective wave excitation and receiving in the following 3D time domain simulation and experiments.

3.2. FE modelling of GW propagation

To verify the wave modal analysis in Section 3.1, time domain modelling and simulation are conducted. The three lowest order of axisymmetric GW modes are in turn employed as primary wave for the wave propagation simulation using a 3D FE model developed in Abaqus/CAE Explicit. Fig. 4 shows the schematic of the FE model. For tone-burst GW excitation, the left end surface is loaded with a user-defined displacement function. The displacement is a Hann windowed sinusoidal wave with its frequency, cycle, and maximum amplitude respectively denoted as *f, N*, and U_{max} (excitation: f = 200 kHz, N = 10, U_{max} = 100nm; receiving: θ = 0°). For ease of signal interpretation, a cylindrical coordinate system ($r - \theta - z$) is used with the origin is located at the center of the left end face (i.e., $r - \theta$ plane) and the z direction is in line with the global X-Y-Z coordinate system. According to the mode shapes shown in Fig. 3, the displacement functions for the three primary wave modes are respectively prescribed in r, θ, and z directions as shown in Fig. 4. This is to ensure that a relatively pure mode can be introduced into the pipe for each simulation, which facilitates the signal analysis. For receiving the signal, several measuring points are set at $Z = L$ surrounding the outer surface of the composite pipe. The geometry is meshed with structured hex elements of type C3D8R. Referring to [28], the maximum mesh size of the model is determined by $\Delta_m \le \lambda /20$ (λ is the wavelength of the primary wave). The time step of the transient response study is determined by $\Delta_t \le 1/20f$ (f is the wavelength of the primary wave). The convergence of the model is confirmed by the fact that the wave velocity and amplitude of the primary GW barely change when further decreasing the mesh size and time step.

(a)

(b)

(c)

(d)

(e)

(f)
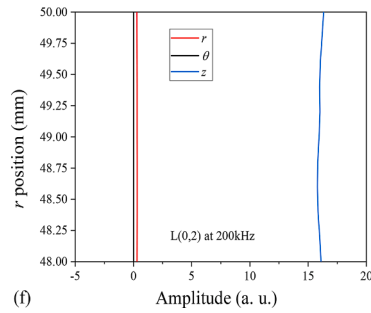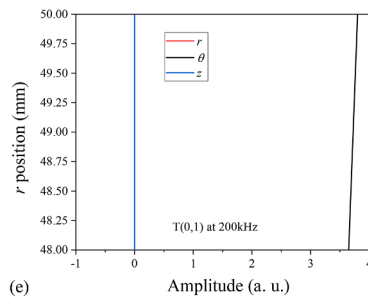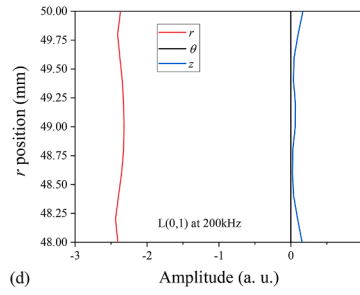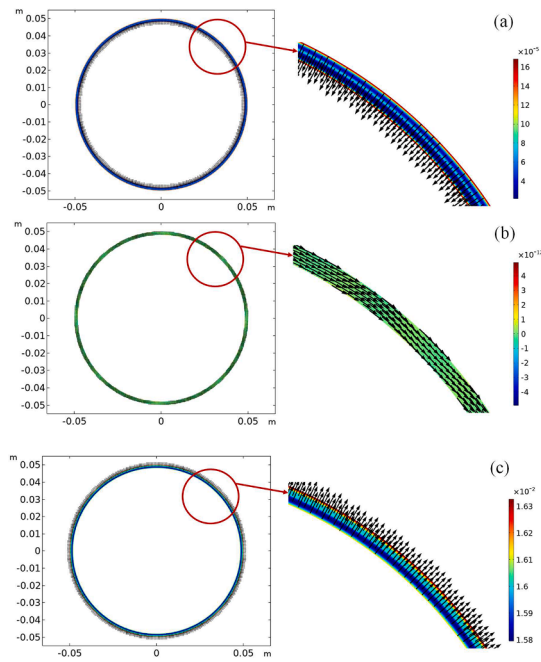
(caption on next page)

Fig. 3. Mode shapes of GWs at 200kHz: (a) L(0,1) mode, (b) T(0,1) mode, (c) L(0,2) mode. Black arrows indicate the displacement component in the cross-section plane, and color maps indicate the displacement component in the wave propagation direction; wave structures of (d) L(0,1) mode, (e) T(0,1) mode, (f) L(0,2) mode at 200 kHz.
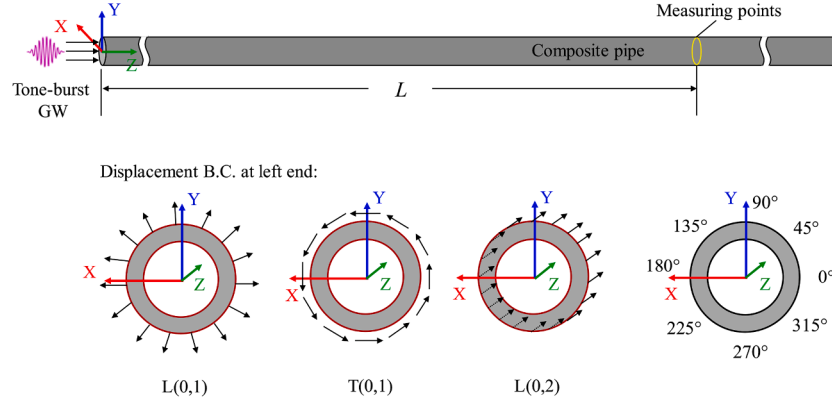

Fig. 4. Illustrations of FE models for simulation of time domain wave propagation.

To analyze the QSP generation induced by material nonlinearity, the third order elastic stiffness constants of the composite pipe are introduced into the simulation using a user-defined subroutine that customized the material constitutive model. Based on Section 2.1, the nonlinear elastic coefficients of $\beta_1 \sim \beta_9$ are related to the nine independent third order stiffness constants of a single CFRP layer [21], which are shown in Table 3. Besides, the regional micro-damage is modelled by scaling up ξ_N times the third order stiffness constants. Given the complexity of the microscale properties inherent in CFRP materials, this method serves as a highly effective approximation for detecting the presence of microdamage, as it elicits discernible nonlinear responses.

As a pre-validation of the 3D time domain model, Fig. 5 shows the typical temporal signals of the primary L(0,1), T(0,1), and L(0,2) modes received at $Z = 0.25$ m, 0.50 m, and 0.75 m. The group velocities of these three primary modes are calculated as 1612.8 m/s, 1995.6 m/s, and 8011.3 m/s, respectively. These values of group velocity are consistent with the theoretical dispersion curves shown in Fig. 2 with less than 5 % errors. Besides, the main displacements of these three modes are polarized in the r, θ and z directions. This is also in line with the theoretically predicted mode shapes shown in Fig. 3.

4. Features of quasistatic pulse in composite pipes

4.1. Mode conversion and cumulative effect

The observation of QSP in the CFRP pipe with quadratic material nonlinearity is achieved using the phase reversal method [29,30], as the QSP displacements are nonlinear signals and have similar properties to the even harmonics. Fig. 6 shows the temporal QSP signals generated from the propagations of the primary modes of L(0,1), T(0,1), and L(0,2). The primary waves at 200 kHz are presented in Fig. 5. The displacements detected in Z direction of two primary waves of opposite phases are superposed and denoted by U_z'. As shown in Fig. 6(a)–(c), the three generated QSP signals have almost the same pulse velocity $c \approx 8200$ m/s of L(0,2) mode. Besides, the displacement of QSP is mostly polarized in Z direction. This indicates that different fundamental GWs can generate the QSP of L(0,2) mode in the anisotropic CFRP pipes considering the material nonlinearity.

Besides, the effect of group velocity mismatching is also observed in Fig. 6(a) and (b). Due to the difference in velocity between the primary L(0,1)/T(0,1) mode and the corresponding QSP of L(0,2) mode, the pulse width of QSP starts increasing shortly after its amplitude increases to a certain degree. The leading edge of the QSP signal has the velocity of L(0,2) mode, and the ending edge has the velocity of the corresponding primary mode. Since the shape of the ending part of the QSP signal is related to the displacement excitation condition in the FE simulation [17], we can focus on the leading part of the QSP signal in the following analysis. Specifically, when the primary mode is L(0,2) mode, the generated QSP can propagate along with the primary wave and only its amplitude increases with propagation distance as shown in Fig. 6(c). This feature of QSP generation on the condition of group velocity matching is significantly useful for microdamage detection in a large area, as the cumulative increase of displacement amplitude of QSP can readily indicate the level of material nonlinearity of materials.

Table 3
Third order stiffness constants (Unit: GPa) of a single CFPR layer used in numerical analysis [26].

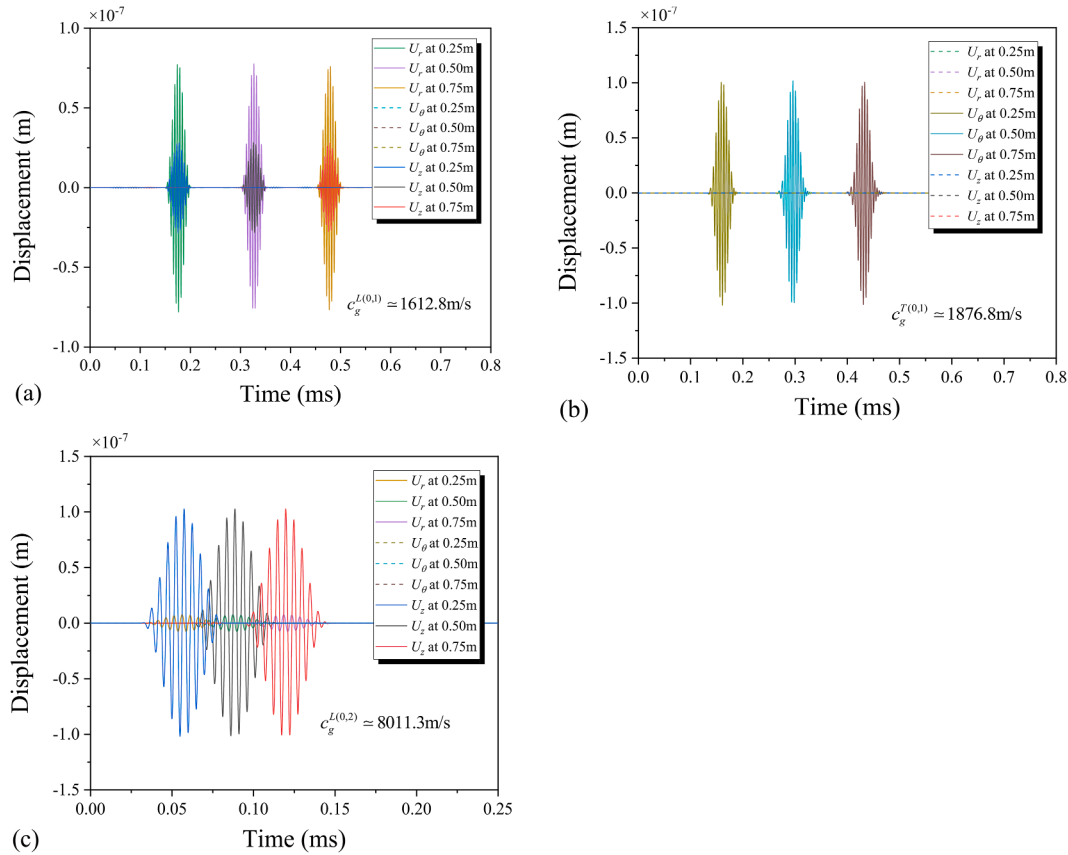| C_{111}	C_{112}	C_{155}	C_{222}	C_{223}	C_{122}	C_{123}	C_{255}	C_{266}
1000	65	−47	−214	−89	−4	65	−33.4	−49.1

Fig. 5. Time domain signals of primary modes: (a) L(0,1), (b) T(0,1), (c) L(0,2). The modes are consistent with the theoretical dispersion curves regarding their group velocities.

4.2. Generation efficiency

Since the wave structures of different primary modes are different, and there are nine independent third order elastic constants in a single unidirectional FRP composite layer, the generation efficiency of QSP can vary with the primary modes and many other factors. Based on the time-domain accumulation feature of QSP and for consistency of comparison, the integration of QSP amplitude over time ($|\int U_z|$) is employed as an index of generation efficiency of QSP by all primary modes. The integration interval is defined as between two time points of the QSP with zero displacement amplitudes at the nearest left and right sides of the pulse. As shown in Fig. 7(a), the generation efficiency of QSP in terms of the amplitude of primary waves is ranked as: L(0,1)>L(0,2)>T(0,1). Similarly, by keeping the amplitude of primary waves at the same level as 100 nm, the generation efficiency of QSP regarding the propagation distance is also ranked as: L(0,1)>L(0,2)>T(0,1) (See Fig. 7(b)). However, the interferences between the different effects of the third order elastic constants on the QSP generation result in the opposite trend of QSP generation in terms of the scaling coefficient ξ_N of third order elastic constants. As shown in Fig. 7(c), the QSP generation of primary L(0,1) and T(0,1) waves decreases when increasing all the third order elastic constants, while the generation efficiency increases for L(0,2) primary wave. This indicates that the effective detection of material nonlinearity in FRP composite pipes using QSP generation is greatly dependent on the optimized combination of primary wave mode, excitation magnitude, and wave propagation distance.

4.3. Duration effect on QSP generation

Another important feature of QSP generation is that the number of cycles of the primary tone-burst GW can influence the absolute amplitude of QSP generated by the group velocity-mismatched primary wave. As shown in Fig. 8(a) and (b), while keeping the frequency and excitation magnitude of primary waves the same, the absolute amplitude of QSPs by L(0,1) and T(0,1) can increase with the number of cycles (i.e., tone-burst duration) of the primary GW. For the case of L(0,2) mode, since the cumulative effect of QSP only displays in the amplitude and not in the temporal width for group velocity matching, the increase of duration of primary GW can only lead to the increase of wave packet length rather than the amplitude of QSP. Fig. 8(c) shows the comparison of the duration effect on QSP generation in pipes across these three primary modes.

It should be noted that, in the FE simulation, GW propagations of different single primary modes are modeled and analyzed
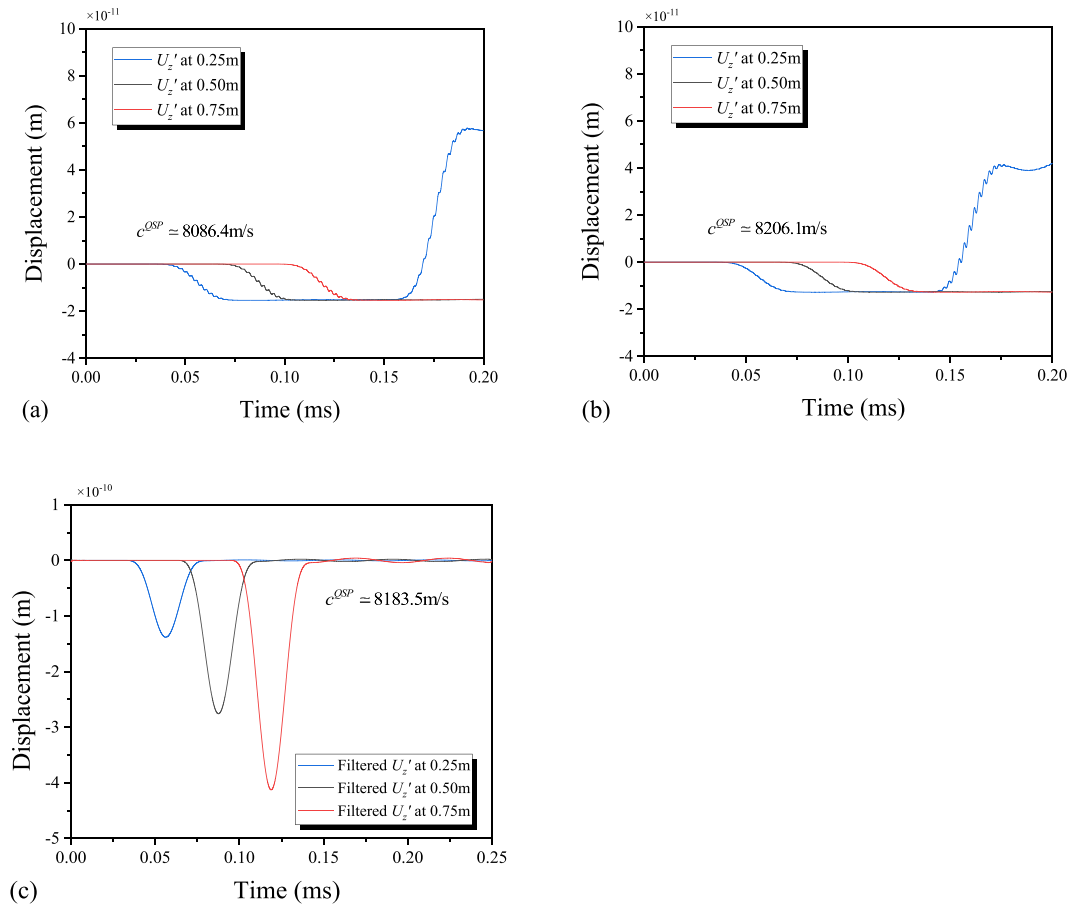
Fig. 6. Time domain signals of QSP generated by primary waves and processed by phase reversal method: (a) by L(0,1) mode, (b) by T(0,1) mode, (c) by L(0,2) mode.

regarding the QSP generation. This facilitates the demonstration of QSP generation and enhances the understanding of the physical mechanism. However, in practical applications, multimodal GWs can be readily excited into the pipe-like waveguides due to different boundary conditions from the perfect mode shapes of the desired mode. For instance, the excitation of L(0,2) mode using a transducer array attached around the pipe inevitably introduces the L(0,1) mode into the pipes. However, based on the above analysis of QSP generation, it is indicated that the induced nonlinear QSPs can possess the same fastest group velocity among all the possible fundamental GW modes. Hence, in scenarios where multiple primary modes are present, the analysis of QSP primarily concentrates on the initial segment of the measured signal, which exhibits polarization in the axial Z direction.

5. Experiments

5.1. Specimens

The specimens used in the following experiments are commercially purchased CFRP pipes. The pipes comprise 10 unidirectional layers with a stacking order of $[C/A_4/C/A_3/C]$ (C: circumferential fiber, A: axial fiber). The inner radius is 48 mm, the outer radius is 50 mm, and the length is 1.5 m. The total thickness of the pipes is 2 mm. The mass density of the pipe is 1560 kg/m^3. The properties of carbon fiber and epoxy resin as separated materials are listed in Tables 4 and 5, respectively. The pipe specimens were produced using carbon fiber and epoxy under high temperature and pressure in specialized equipment. For a unidirectional layer of such CFRP materials, the stiffness matrix components are around the values provided by the manufacturer and listed in Table 2.

For the feasibility study of microdamage assessment using QSP generation, artificial thermal fatigue damage was introduced into the CFRP pipes. A heat gun (BOSCH GHG 600–3) was set 30 mm upon the CFRP pipe with the heating temperature set as 300 °C . Regional thermal fatigue damage was incurred across the entire pipe by moving the heating point at regular intervals of 0.05 m along the pipe's length and rotation of 22.5° around its circumference for each specified processing time. The pipe was heated for 30 s at each fixed position, and the process was carried on for different times to compare the results of ultrasonic GW tests. Fig. 9 shows a picture of the CFPR pipes, heat gun, and illustration of the heating process. In the process of thermal cycling, composite laminates experience
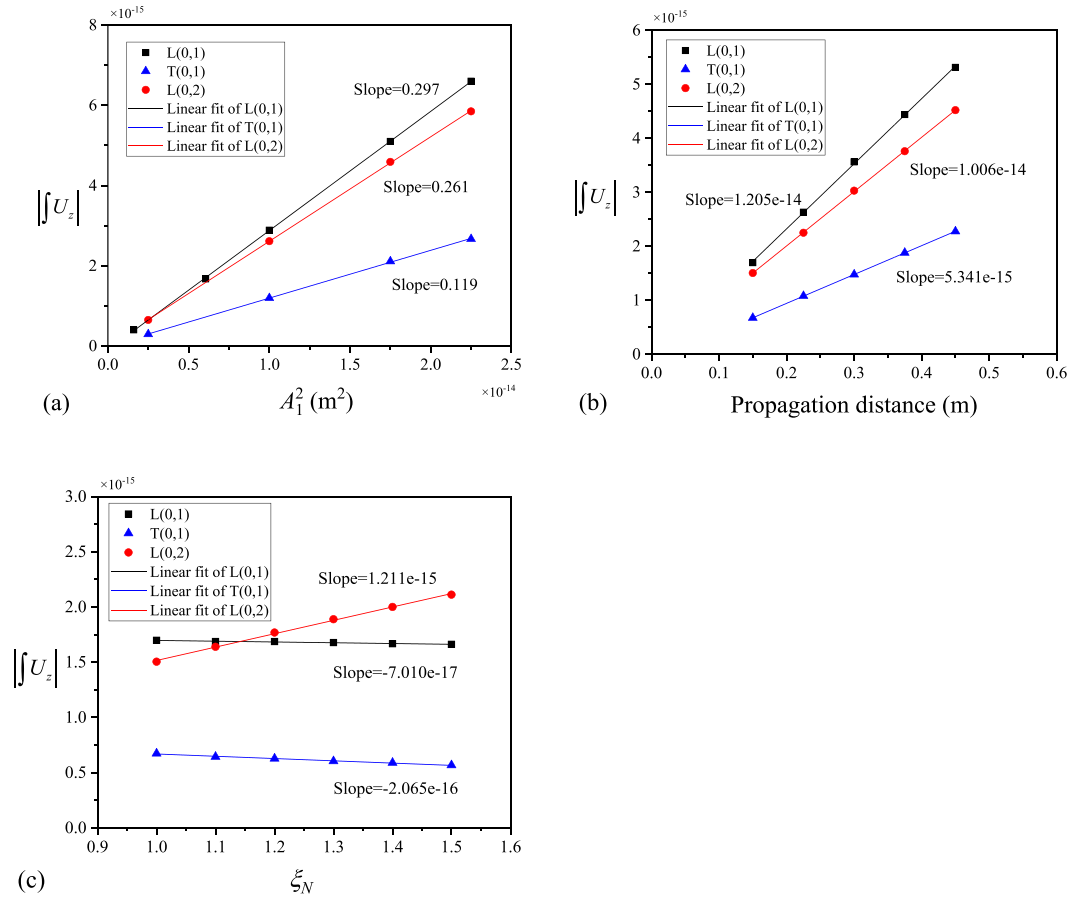
Fig. 7. Comparison of QSP generations in CFRP pipe: magnitude of QSP with respect to (a) amplitude of primary GW, (b) propagation distance, (c) magnification factor of nonlinear elastic constants.

thermal stresses. These recurring thermal stresses can lead to damage akin to what is seen under mechanical cyclic loading, including micro-scale damages in the forms of transverse matrix cracks, debonding, and delamination within the layers [31,32]. Consequently, the heating process degraded the fiber reinforced composites. From the nonlinear ultrasonic point of view, these micro-scale changes inside the materials are intrinsically related to the variations of elasticity properties of the materials, which can be characterized by the measurement of higher order elastic constants [33]. Thus, the QSP generation of guided waves, as one of the nonlinear ultrasonic responses, can also be potentially used for the evaluation of micro-damages in composite materials.

5.2. Experimental setup

The ultrasonic excitation and measurements were conducted using the NI signal generator, high-power amplifier, piezoceramic transducer, and 3D laser Doppler scanning vibrometer system (LDV, Polytech PSV-400). Fig. 10 shows the schematic diagram and pictures of the experiment setup. The Hann windowed tone-burst sinusoidal signal was customized and generated by the NI signal generator (PXIe-5122). After being amplified by the high-power amplifier (CIPRIAN HVA-800A), the high-voltage signal was transmitted to the shear piezoceramic transducers (Dimensions: 10.0mm×5.0mm×2.0 mm). The transducers were evenly glued upon the outer surface of the CFRP pipe at one end using conductive epoxy (Chemtronics CW2400). The vibration mode of the piezoceramic actuators is mainly in shear direction (i.e., parallel to the axial direction of the pipes). As a result, the longitudinal L(0,2) mode can be introduced into the pipe at the largest efficiency. Ultrasonic GWs were excited into the pipe and propagated towards the other end of the pipe. The GWs were eventually picked up by the 3D laser Doppler vibrometer. To enhance the reflectivity of the laser beams, the measurement area of the CFRP pipe was painted with a reflective coating (CRC 18015). The recorded signals were averaged 1500 times to improve the signal-to-noise ratio. Digital low-pass filters were applied to the received signals by the data acquisition system. The same process at each testing location was repeated three times to minimize the measurement errors.
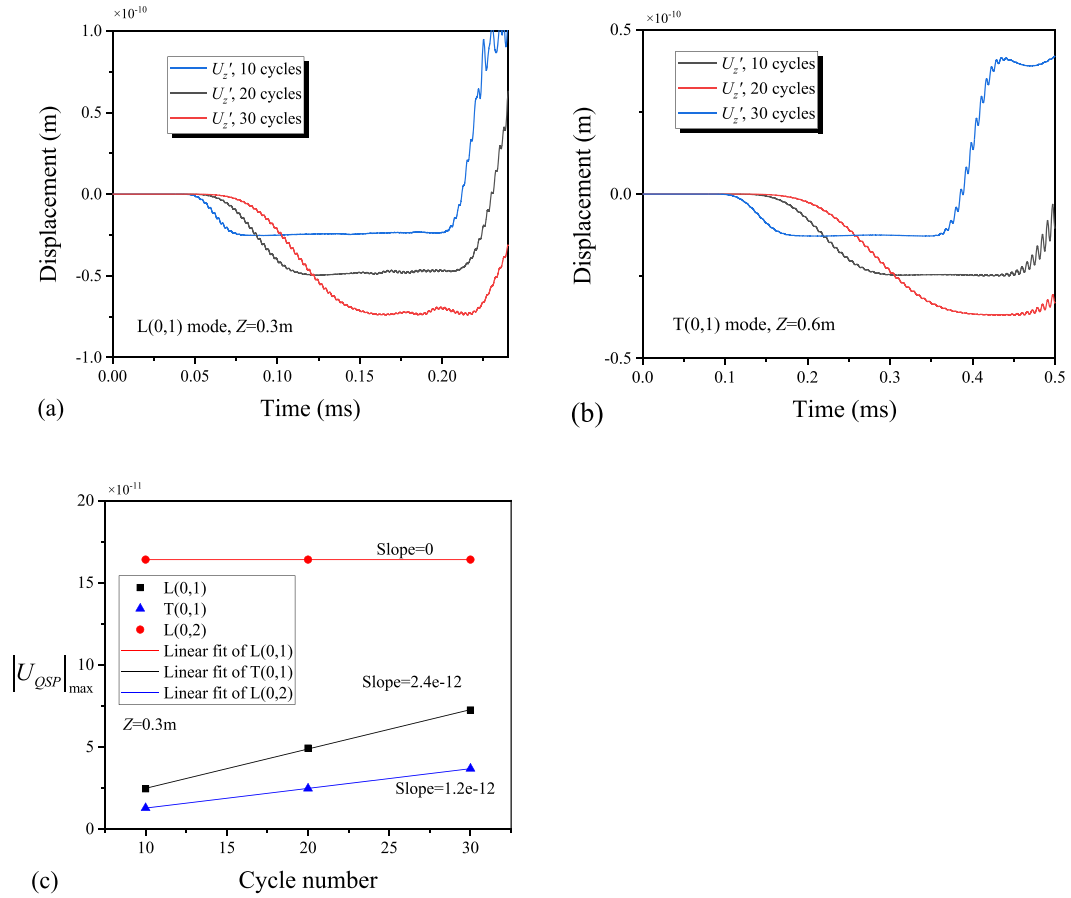
Fig. 8. Duration effect of primary wave on the amplitude of QSP: time-domain signals of QSPs generated by (a) L(0,1) mode and (b) T(0,1) mode of different tone-burst length, (c) comparison of different primary modes.

Table 4
Properties of carbon fiber.

Tensile modulus	Tensile strength	Elongation	Density
242 GPa	4550 MPa	1.8 %	1790 kg/m^3

Table 5
Properties of epoxy resin.

Vitrification transition temperature	Tensile modulus	Tensile strength	Bending modulus	Bending strength
125℃~135℃	3.82GPa	80MPa	4.28GPa	115MPa

5.3. Results & discussions

5.3.1. Analysis of primary waves

As discussed in Section 4.1 and shown in Fig. 6(c), the QSP generation exhibits cumulation in amplitude with propagation distance when the primary GW has the same group velocity as the induced QSP wave. Therefore, we expect that the L(0,2) mode is excited into the pipe by the eight shear piezoceramic transducers. Due to the similarity between the mode shape of L(0,2) mode and the setup of actuators, the excitability of L(0,2) mode is optimized. However, the transducer array can still result in the occurrence of multiple GW modes. While the primary GWs propagate along the axis of the pipe (Z direction), they also scatter away towards the circumferential direction of the pipe. Therefore, the multimodal feature and the interference of GWs from different wave sources lead to the oscillation of wave amplitude measured at different locations.

We first measured the primary waves in intact pipe specimen. As shown in Fig. 11(a), the out-of-plane displacements U_r of the 200
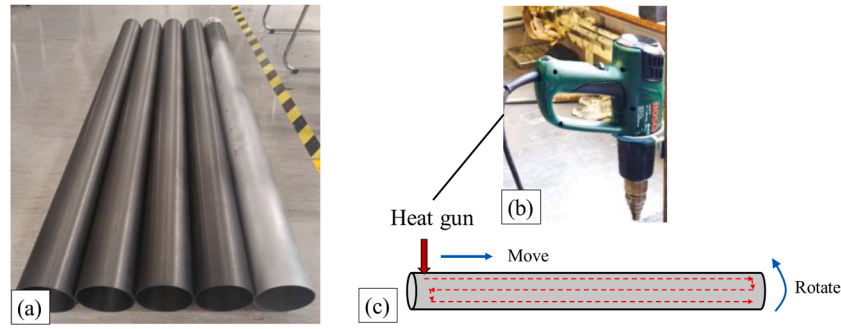
Fig. 9. (a) CFRP specimens, (b) Thermal gun used for heating CFRP specimens, (c) Illustration of heating process.
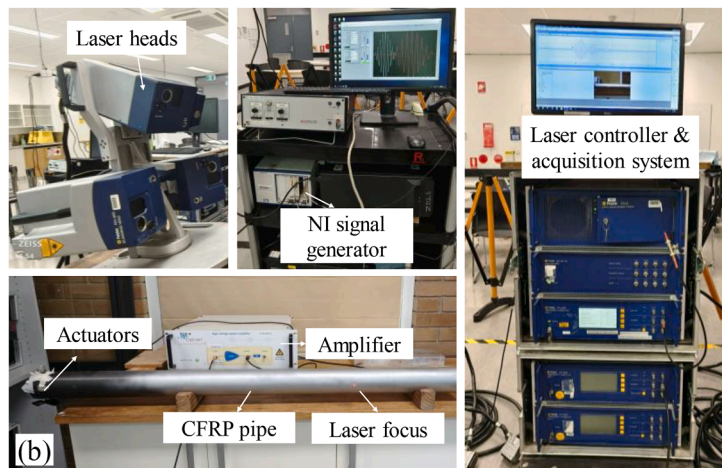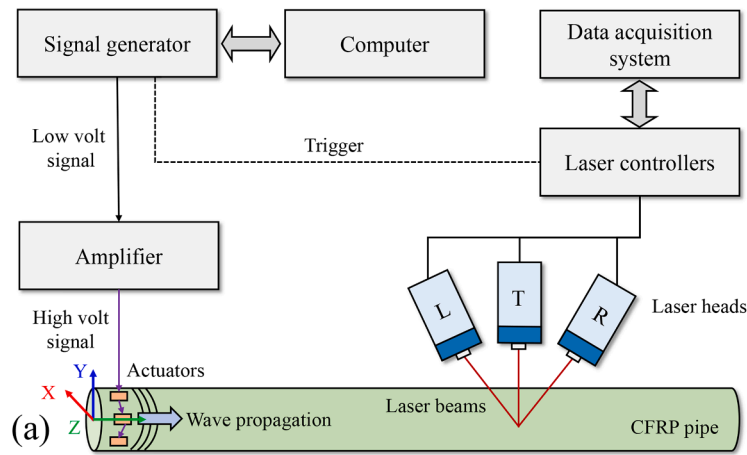

Fig. 10. Experimental setup: (a) schematic diagram, (b) physical pictures.

kHz primary waves at different axial locations are extracted. The group velocity of the fundamental wave packet is calculated as about 1610 m/s. Referring to the dispersion curves shown in Fig. 2, it is indicated that the L(0,1) mode is generated into the pipe. Besides, it should be noted that the out-of-plane amplitudes of L(0,1) mode measured at different locations do not decrease with the propagation distance. This oscillation of amplitude is due to the interference of waves from the transducer array. On the other hand, the axial displacements of the primary waves are extracted and shown in Fig. 11(b). The first wave packet has a group velocity of around 8026 m/s, which is in line with the L(0,2) mode at 200 kHz. There are many other primary wave packets polarized in the axial direction. In comparison to Fig. 6(c), which is obtained by exciting pure L(0,2) mode into the pipe, this is the experimental phenomenon that multiple GW modes are introduced into the pipe.
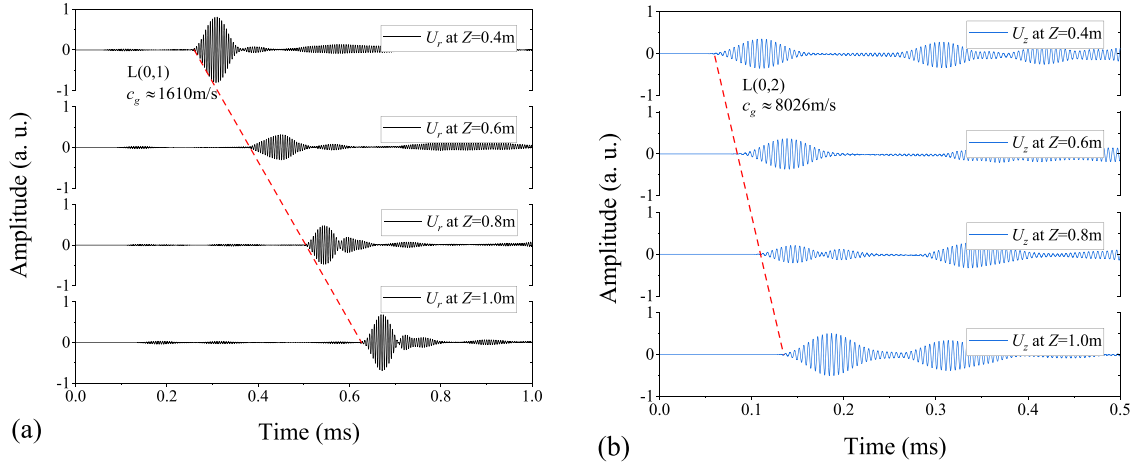
Fig. 11. Fundamental waves received in the (a) *r* direction and in the (b) *z* direction at different propagation distances.

5.3.2. Identification of QSP generation

To extract the QSP signals, the phase reversal method [34] was used. As the QSP is one of the even nonlinear responses of GW propagation, it can be amplified by two times when superposing the two received wave fields of opposite excitation phases [17]. In the meantime, the offset of two fundamental waves will occur. This method can significantly enhance the signal-to-noise ratio for the QSP measurement. Besides, the measured signals were averaged 1500 times and digital filtered. The axial displacements, which are generated by primary waves of the opposite phase, are measured at the different locations along the Z direction of the pipe. For a specific measurement location, the two axial signals are superposed and low pass filtered. The cut-off frequency of the digital filter is set as the main frequency of primary waves.

Fig. 12 shows the QSP signals measured at different Z locations at $\theta = 0°$. Based on the analysis of QSP by FE simulation results in Section 4, we infer that the QSP signal is formed by the superposition of many QSP components of different primary GW modes. The QSPs generated by all primary waves possess the same largest possible group velocity of GWs in the pipe. Since there exists a series of primary wave packets in the axial direction, it can be compared with the circumstance that a primary wave with a long duration is excited. As shown in Fig. 8, the duration effect can lead to the amplitude increase of QSP for group velocity-mismatched mode pairs. Thus, in the experiment, the constructive interference of QSP components eventually leads to the increase of its amplitude to a certain degree. This increase is not only due to the cumulative effect of QSP that is generated under the group velocity matching condition with the primary L(0,2) mode, but also due to the duration effect provided by the other multiple relatively slower primary GW modes. The group velocity of the resultant QSP signal is calculated as about 8071 m/s, which is consistent with the dispersion curves of L(0,2) mode at zero frequency. This verifies the theoretical and FE simulation analyses. It is noted that the QSP signal does not increase with the propagation distance in the experiment. This is because the primary wave packets are subject to dispersion, attenuation, and interference with each other. Unlike a pure fundamental GW mode that can be simulated in FE modeling, the primary GW signals measured at different axial and circumferential locations have different magnitudes in practice.

To further validate the QSP generation and propose a feasible nonlinear parameter for microdamage detection in composite pipes, different excitation levels and frequencies of primary GWs are induced into the pipe. As the out-of-plane displacement signal U_r has obviously fewer wave packets than that extracted in the axial in-plane direction, the relation of the absolute magnitude of QSP signals $|U_{QSP}|_{\max}$ against the square of the out-of-plane displacement U_r^2 is presented in Fig. 13. It is found that there is a linear relationship between the magnitude of QSP signal and the square of primary GW magnitude. Moreover, when increasing the frequency of primary waves, the slope of its linear fit increases significantly as well. These results are consistent with the theoretical and numerical studies. For a single primary wave mode, the squares of magnitude and frequency of the primary wave are theoretically linear and proportional to the generation efficiency of the corresponding nonlinear QSP signal. In the experiment, although the generated primary wave is multimodal, the relationship between the extracted QSP amplitude and the primary out-of-plane displacement shows similar effects of the excitation magnitude and frequency of the primary wave on the QSP generation.

5.3.3. Microdamage assessment using QSP

Based on the analysis in the above section, the relative nonlinear acoustic parameter employing the QSP generation is constructed as

$$\widetilde{\beta}_{QSP} = \frac{|U_{QSP}|_{\max}}{U_r^2}. \tag{12}$$

The ultrasonic signals are in turn measured in three CFRP pipes (#1, #2, #3) using the same process. By repeating the heating cycle of the pipe for different times, the early-stage thermal fatigue microdamage is generated in the pipes. The measurement point is set as $Z = 1.0$ m and $\alpha = 0°$. After acquiring the GW signals, the wave velocities of primary modes are calculated to be nearly the same, which

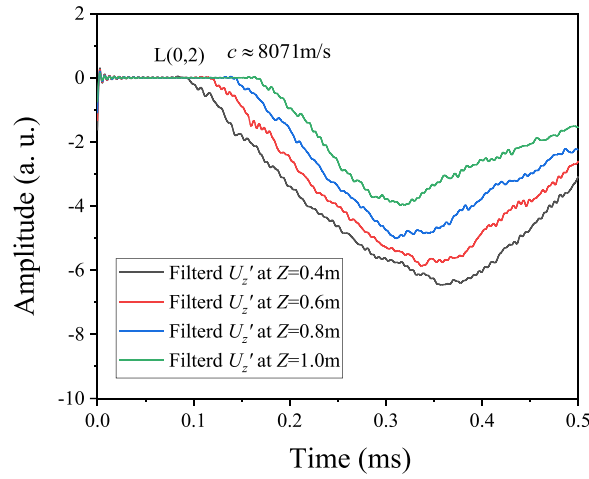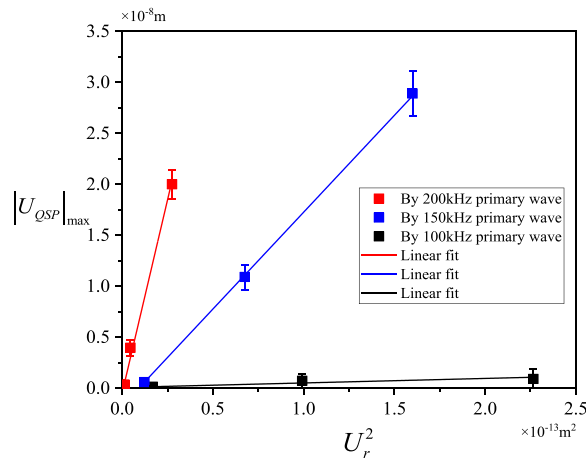**Fig. 12.** Low pass filtered QSP signals received at different axial *Z* locations.

Fig. 13. Relationship of absolute magnitude of QSP signals against that of primary waves.
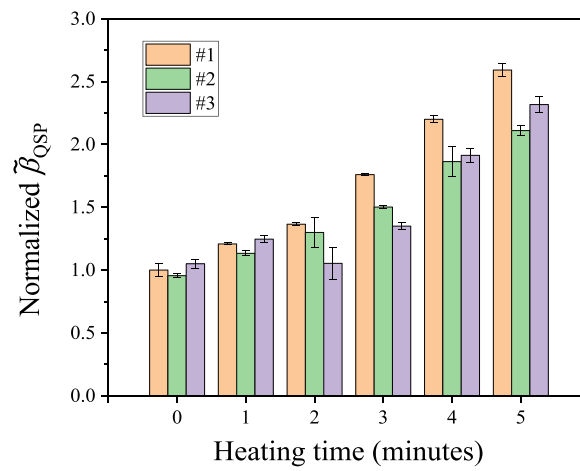

Fig. 14. Measured relative nonlinear acoustic parameter $\tilde{\beta}_{QSP}$ with respect to the total heating time of CFRP pipes.

suggests the ineffectiveness of linear ultrasound techniques using wave velocity. On the other hand, the comparison of the proposed parameter $\widetilde{\beta}_{QSP}$ of the three CFRP pipes is shown in Fig. 14. The calculated $\widetilde{\beta}_{QSP}$ is found to increase with the total heating time for pipes #1 and #2, while a slight decrease occurs for pipe #3 when the heating time is 2 min. This may be due to the inconsistency of the microdamage in the specimens. However, the overall trend of the variation of $\widetilde{\beta}_{QSP}$ indicates that this proposed nonlinear ultrasonic index is sensitive to thermal fatigue damage in CFRP composite pipes.

It should be noted that, under the current experimental conditions, we cannot yet achieve the perfect excitation of a pure L(0,2) mode inside the pipe specimens. For practical microdamage evaluation, the measurement of QSP signals using the identical experimental setups for different specimens is required for effectively comparing the variations of material properties. However, the generated QSP waves by different primary GW modes propagation in pipe have the same pulse velocity and are always the fastest longitudinal mode. Although both the primary wave and the generated QSP wave are influenced by the excitation condition, this unique feature of QSP generated by GWs in pipe makes the mode recognition of QSP wave less troublesome. Besides, the energy of generated QSP is less dissipated in cylindrical shell than in plate structures, and QSP suffers little the acoustic attenuation in composites as well. Thus, this generated QSP signal can be more readily predicted and analyzed than higher harmonic waves in a certain degree.

6. Conclusions

This study presents the numerical and experimental investigations on the quasistatic pulse generation in CFRP composite pipes. The theoretical background of QSP generation in anisotropic materials has been demonstrated and summarized. Features including the temporal waveform, cumulative effect, generation efficiency, and duration effect of the QSP generated by different primary guided wave modes have been studied by FE modeling and simulation. Experimental observations of the nonlinear QSP signals measured in CFRP pipes have been conducted using piezoceramic transducer array and the 3D laser vibrometer scanning system. The absolute amplitude of the QSP signal has been found to be proportional to the excitation magnitude and frequency of the primary wave. The relative nonlinear acoustic parameter of the amplitude ratio $\widetilde{\beta}_{QSP}$ has been proposed. The results of $\widetilde{\beta}_{QSP}$ measured in CFRP pipes have shown high sensitivity to early-stage thermal fatigue damage in composite pipes compared to linear ultrasonic characteristics.

CRediT authorship contribution statement

Chang Jiang: Conceptualization, Methodology, Writing – original draft. **Weibin Li:** Supervision, Writing – review & editing. **Ching-Tai Ng:** Supervision, Writing – review & editing. **Mingxi Deng:** Supervision, Writing – review & editing.

Declaration of competing interest

The authors declare that they have no known competing financial interests or personal relationships that could have appeared to influence the work reported in this paper.

Data availability

Data will be made available on request.

Acknowledgments

References

[1] F.G. Alabtah, E. Mahdi, F.F. Eliyan, The use of fiber reinforced polymeric composites in pipelines: a review, Compos. Struct. 276 (2021) 114595, https://doi.org/10.1016/j.compstruct.2021.114595.

[2] O. Ahmed, X. Wang, M.-V. Tran, M.-Z. Ismadi, Advancements in fiber-reinforced polymer composite materials damage detection methods: towards achieving energy-efficient SHM systems, Composit. Part B 223 (2021) 109136, https://doi.org/10.1016/j.compositesb.2021.109136.

[3] J.L. Rose, Y. Cho, M.J. Aviolis, Next generation guided wave health monitoring for long rangeinspection of pipes, J. Loss Prev. Process Ind. 22 (2009) 1010–1015, https://doi.org/10.1016/j.jlp.2009.08.011.

[4] R. Guan, Y. Lu, W. Duan, X. Wang, Guided waves for damage identification in pipeline structures, Areview. Struct Control Health Monit 24 (2017) e2007, https://doi.org/10.1002/stc.2007.

[5] Z. Su, L. Ye, Y. Lu, Guided Lamb waves for identification ofdamage in composite structures: a review, J. Sound Vib. 295 (2006) 753–780, https://doi.org/10.1016/j.jsv.2006.01.020.

[6] M.F. Hamilton, D.T. Blackstock, Nonlinear Acoustics, Academic Press Inc, San Diego, CA, 1998.

[7] K-Y Jhang, CJ Lissenden, I Solodov, Y Ohara, V Gusev (Eds.), Measurement of Nonlinear Ultrasonic Characteristics, Springer, Singapore, 2020.

[8] V.K. Chillara, C.J. Lissenden, Review of nonlinear ultrasonic guided wave nondestructive evaluation: theory, numerics, andexperiments, Opt. Eng. 55 (2016) 011002, https://doi.org/10.1117/1.OE.55.1.011002.

[9] M. Mitra, S. Gopalakrishnan, Guided wave based structural health monitoring: a review, Smart Mater. Struct. 25 (2016) 053001, https://doi.org/10.1088/0964-1726/25/5/053001.

[10] M. Hasanian, C. Lissenden, Second order harmonic GW mutual interactions in plate: vector analysis, numerical simulation, and experimental results, J. Appl. Phys. 122 (2017) 084901, https://doi.org/10.1063/1.4993924.

[11] W. Li, M. Deng, N. Hu, Y. Xiang, Theoretical analysis and experimental observation of freguency mixingresponse of ultrasonic Lamb waves, J. Appl. Phys. 124 (2018) 044901, https://doi.org/10.1063/1.5028536.

[12] W. Li, Y. Cho, Thermal fatigue damage assessment in an isotropic pipe using nonlinear ultrasonic guided waves, Exp. Mech. 54 (2014) 1309–1318, https://doi.org/10.1007/s11340-014-9882-2.

[13] M. Li, L. Liu, G. Gao, M. Deng, N. Hu, Y. Xiang, W. Zhu, Response features of nonlinear circumferential guided wave on earlydamage in inner layer of a composite circular tube, Chin. PhyS. B 28 (2019) 044301, https://doi.org/10.1088/1674-1056/28/4/044301.

[14] W. Li, Z. Lan, N. Hu, M. Deng, Modeling and simulation of backward combined harmonic generation induced by one-way mixing of longitudinal ultrasonic guided waves in a circular pipe, Ultrasonics 113 (2021) 106356, https://doi.org/10.1016/j.ultras.2021.106356.

[15] C. Yeung, C.-T. Ng, Nonlinear guided wave mixing in pipes for detection of material nonlinearity, J. Sound Vib. 485 (2020) 115541, https://doi.org/10.1016/i.jsv.2020.115541.

[16] J. Cantrell, Acoustic-radiation stress in solids. I. Theory, Phys. Rev. B 30 (1984) 3214, https://doi.org/10.1103/PhysRevB.30.3214.

[17] P. Nagy, J. Qu, L. Jacobs, Finite-size effects on the quasistatic displacement pulse in a solid specimen with quadratic nonlinearity, J. Acoust. Soc. Am. 134 (2013) 1760–1774, https://doi.org/10.1121/1.4817840.

[18] X. Jacob, R. Takatsu, C. Barrière, D. Royer, Experimental study of the acoustic radiation strain in solids, Appl. Phys. Lett. 88 (2006) 134111, https://doi.org/10.1063/1.2191428.

[19] K. Narasimha, E. Kannan, K. Balasubramaniam, Simplified experimental technique to extract the acoustic radiation induced static strain in solids, Appl. Phys. Lett. 91 (2007) 134103, https://doi.org/10.1063/1.2793181.

[20] X. Wan, P. Tse, X. Zhang, G. Xu, Q. Zhang, H. Fan, Q. Mao, M. Dong, C. Wang, H. Ma, Numerical study on static component generation from the primary Lamb waves propagating in a plate with nonlinearity, Smart Mater. Struct. 27 (2018) 045006, https://doi.org/10.1088/1361-665X/aaafeb.

[21] C. Jiang, W. Li, M. Deng, C.-T. Ng, Quasistatic pulse generation of ultrasonic guided waves propagation in composites, J. Sound Vib. 524 (2022) 116764, https://doi.org/10.1016/j.jsv.2022.116764.

[22] C. Jiang, C. Zhang, W. Li, M. Deng, C.-T. Ng, Assessment of damage in composites using static component generation of ultrasonic guided waves, Smart Mater. Struct. 31 (2022) 045025, https://doi.org/10.1088/1361-665X/ac5a77.

[23] W. Li, C. Jiang, J. Xiao, C. Xu, M. Deng, Assessment of thermal damage in polymethyrylate using quasi-static components of ultrasonic waves, J. Nondestr. Eval. 42 (2023) 13, https://doi.org/10.1007/s10921-023-00923-3.

[24] X. Yu, M. Ratassepp, Z. Fan, Damage detection in quasi-isotropic composite bends using ultrasonic feature guided waves, Compos. Sci. Technol. 141 (2017) 120–129, https://doi.org/10.1016/j.compscitech.2017.01.011.

[25] P. Zuo, Z. Fan, SAFE-PML approach for modal study of waveguideswith arbitrary cross sections immersed in inviscid fluid, J. Sound Vib. 406 (2017) 181–196, https://doi.org/10.1016/j.jsv.2017.06.001.

[26] J. Zhao, V. Chillara, B. Ren\, H. CHo, J. Qiu, al e, Second harmonic generation in composites: theoretical and numerical analyses, J. Appl. Phys 119 (2016) 064902, https://doi.org/10.1063/1.4941390.

[27] C. Jiang, W. Li, C.-T. Ng, M. Deng, Quasistatic Component Generation of Group Velocity Mismatched Guided Waves in Tubular Structures for Microdamage Localization, SSRN Electron. J. (2023), https://doi.org/10.2139/ssrn.4398162.

[28] X. Wan, G. Xu, Q. Zhang, P. Tse, H. Tan, A quantitative method for evaluating numerical simulation accuracy of time-transient Lamb wave propagation with its applications to selecting appropriate element size and time step, Ultrasonics 64 (2016) 25–42, https://doi.org/10.1016/j.ultras.2015.07.007.

[29] J.-Y. Kim, L.J. Jacobs, J. Qu, J.W. Littles, Experimental characterization of fatigue damage in a nickel-base superalloy using nonlinear ultrasonic waves, J. Acoust. Soc. Am. 120 (2006) 1266–1273, https://doi.org/10.1121/1.2221557.

[30] J.Y. Kim, J. Qu, L.J. Jacobs, J.W. Littles, M.F. Savage, Acoustic Nonlinearity Parameter Due to Microplasticity, J. Nondestr. Eval. 25 (2006) 28–36, https://doi.org/10.1007/s10921-006-0004-7.

[31] D.S. Forsyth, S.O. Kasap, I. Wacker, S. Yannacopoulos, Thermal fatigue of composites: ultrasonic and SEM evaluations, J. Eng. Mater. Technol. 116 (1) (1994) 113–120, https://doi.org/10.1115/1.2904246.

[32] M.D. Seale, B.T. Smith, W.H. Prosser, Lamb wave assessment of fatigue and thermal damage in composites, J. Acoust. Soc. Am. 103 (1998) 2416–2424, https://doi.org/10.1121/1.422761.

[33] W. Li, Y. Cho, J.D. Achenbach, Detection of thermal fatigue in composites by second harmonic Lamb waves, Smart Mater. Struct. 21 (2012) 085019, https://doi.org/10.1088/0964-1726/21/8/085019.

[34] W. Li, C. Jiang, X. Qing, L. Liu, M. Deng, Assessment of low-velocity impact damage in composites by the measure of secondharmonic guided waves with the phase-reversal approach, Sci. Prog. 103 (2020) 1–14, https://doi.org/10.1177/0036850419881079.

Chapter 8: Conclusions & Prospect

8.1. Conclusions

This thesis has presented the systematic study of QSC generation in solids with material nonlinearity. Through theoretical analysis, numerical simulation, and experimental investigations, the QSC generation of guided waves in plates and pipe-like isotropic and anisotropic materials has been explored and discussed. Important findings are summarized below:

1. The QSC pulse wave as one of the nonlinear ultrasonic responses always possesses the fastest velocity among all the possible guided wave modes in structures.

2. The QSC pulse wave generated by different primary waves always exhibits in-plane displacement in solid waveguides, either as pure in-plane mode in isotropic materials or partly in-plane coupled mode in anisotropic composite materials.

3. The displacement direction (positivity or negativity) of QSC pulse is dependent on the wave propagation direction and the material properties.

4. The QSC generation has intrinsic cumulative effect in magnitude during the primary guided wave propagation, however, suffers relatively larger divergence loss than higher harmonics due to poor directivity.

5. The cumulative generation of QSC by guided waves displays in the increase of amplitude while the pulse velocity matches the group velocity of primary waves. When the pulse velocity of QSC is different from that of primary wave, the cumulative effect is mainly shown by the increase of pulse width soon after the amplitude grows a few.

6. The QSC pulse in time domain has either the envelop shape of its corresponding primary wave when there is a group velocity matching, or a flat-top shape when there is a group velocity mismatch between the QSC and the fundamental wave.

7. The proposed microdamage evaluation approach in highly acoustic attenuation materials using the QSC generation is cost-effective and is sensitive to early-stage damages.

8. The QSC pulse generation by guided waves can be utilized for microdamage localization

when satisfying the velocity mismatch condition and can be utilized for regional microdamage evaluation when satisfying the velocity matching condition.

9. Experimental studies have shown good agreement with the theoretical predictions and results of finite element simulations. Potential NDT applications for advanced industrial materials can be promisingly developed based on the QSC phenomenon of ultrasonic guided waves.

8.2. Prospect

While the present thesis makes contributions to the field of nonlinear ultrasound, it is essential to acknowledge certain limitations: 1) The theoretical framework for directly deriving the conclusions is currently incomplete, 2) The numerical simulations adopted the displacement boundary conditions for guided wave excitations, while using traction boundary conditions may lead to new minor findings, and 3) The experiments validated most of the results of the finite element analyses, while full verification requires more advanced ultrasonic sensors and measurement equipment. To address the aforementioned limitations and contribute to the ongoing discourse in QSC generation by guided waves, future research endeavors could explore the following avenues:

1. Development of a general theoretical framework that can directly indicate all the features of QSC generation by guided waves.

2. Investigation on the QSC generation of ultrasonic waves in materials with specific stress-loaded status.

3. Investigation on the QSC generation of feature guided waves in geometries of specific shapes.

4. Investigation on the modeling of QSC generation by interactions between practical micro-damages with ultrasound.

5. Development of theoretical framework for mechanism interpretations of QSC generations in materials with different types of micro-damages.

6. Experimental study on the NDT applications regarding QSC generation based on novel

signal processing techniques and damage imaging algorithms.